VERTICAL LINE ARRAY PERFORMANCE IN GAS HYDRATE BEARING SEDIMENT IN THE NORTHERN GULF OF MEXICO

by

Erika Géresi
M.Sc. University of Eötvös Loránd 2002

A Thesis Submitted in Partial Fullfillment of the
Requirements for the Degree of
DOCTOR OF PHILOSOPHY
in the School of Earth and Ocean Sciences

Supervisory Committee:

Supervisor: N.R. Chapman, PhD (School of Earth and Ocean Sciences, University of Victoria,
Co-Supervisor: S.E. Dosso, PhD (School of Earth and Ocean Sciences, University of Victoria),
Departmental Member: G.D. Spence, PhD (School of Earth and Ocean Sciences, University of Victoria),
Outside Member: Adam Zielinski, PhD (Department of Mechanical Engineering, University of Victoria),
Additional Member: T.M. Mcgee, PhD (University of Mississippi),
External Examiner: Camelia D. Knapp, PhD (University of South Carolina).

Supervisory Committee:

Supervisor: N.R. Chapman, PhD (School of Earth and Ocean Sciences, University of Victoria,
Co-Supervisor: S.E. Dosso, PhD (School of Earth and Ocean Sciences, University of Victoria),
Departmental Member: G.D. Spence, PhD (School of Earth and Ocean Sciences, University of Victoria),
Outside Member: Adam Zielinski, PhD (Department of Mechanical Engineering, University of Victoria),
Additional Member: T.M. Mcgee, PhD (University of Mississippi),
External Examiner: Camelia D. Knapp, PhD (University of South Carolina).

Abstract

This thesis is aimed at investigating the possibilities of using vertical line array (VLA) data to image the gas hydrate stability zone (GHSZ) in the northern Gulf of Mexico. The presence of gas hydrate can be inferred from seismic evidence such as bottom simulating reflectors (BSRs) or changes in seismic velocity. The petroliferous northern Gulf of Mexico is noted for its obvious absence of BSRs, a characteristic it shares with other active passive margins with mobile salt and/or shale, which have high propagation velocities for seismic waves. This makes the imaging and the identification of the gas hydrates a challenging process with conventional seismic techniques. Therefore, new techniques in data acquisition, processing and analysis are sought to improve the imaging of complex areas. The new, unconventional seismic data acquisition technique used here is the VLA. This work defines a seismic processing flow

that has been developed to extract velocity, travel-time and amplitude information from VLA data to predict the hydrate distribution over the surveyed area. Specialized amplitude versus offset analysis and inversion is applied to the VLA data using a Bayesian inversion approach to provide estimates and uncertainties of the viscoelastic physical parameters at an interface. This thesis will compare the inversion of the 2-D seismic reflection data collected in 1998 by the USGS and in 2002 by the Center for Marine Resources and Environmental Technology (CMRET) to the VLA data collected in 2002 and 2003 by the CMRET to assess the value of a VLA in monitoring changes in the near-surface sediments that can be associated with the presence of gas hydrate.

Table of Contents

List of Tables

List of Figures

Dedication

Szüleimnek Diószegi Éva és Tamásnak akik szeretete és pártolása nélkül idáig sosem juthattam volna el.

Chapter 1

Introduction

1.1 General Overview

This dissertation presents results of the performance assessment of a vertical line array (VLA) to image structure in hydrate bearing sediment. The study is located in Mississippi Canyon Block 798 (MC798) in the northern Gulf of Mexico. At the survey area gas hydrates were widely reported [53] near the sea floor, but are described at only one deep drill site. Features observed in and around MC798 imply a complex geology and stress regime. In previous studies, conventional seismic techniques often failed to image complex geological features, especially in the presence of gas hydrates that have high propagation velocities for seismic waves. Therefore, new techniques in data acquisition and processing are sought to improve the imaging of complex areas.

The technique used in this study is the VLA. The site was the target of numerous multi- and single-channel seismic surveys and various other experiments including piston coring.

The main objectives of this work include:

- development of methodology for processing the VLA data for better imaging,
- creation of an integrated velocity structure model from the VLA data,
- performing amplitude studies using VLA data to create a sea floor reflection coefficient model of the area and conduct an inversion of amplitude variation with angle,
- assessment of the VLA performance in comparison with single- and multi-channel seismic data from previous experiments at the survey area, and
- integration of new results with previous information to develop possible scenarios of the hydrate distribution in MC798.

This dissertation describes the progress related to these objectives.

The main dataset was collected in 2003 using an 80 in^3 watergun source recorded on a single 16-channel VLA in MC798. During previous cruises in 2002 and 1998, conventional single- and multi-channel seismic data were recorded in the same area. Several lines from these experiments were placed close to the VLA site and therefore

a direct comparison with these data is made in order to assess the VLA performance and the gas hydrate distribution of the survey area.

The first chapter of this work provides a general overview and the motivation behind this study. Chapter 2 presents an overview on gas hydrates with special emphasis on the gas hydrates in the northern Gulf of Mexico. Chapter 3 gives a description of all the seismic experiments previously done in MC798 used in this research. An introduction is given in this section about the VLA technique and the main VLA experiment with the technical details as well. The processing sequence for the conventional (horizontal receiver style) 2-D seismic data is given in Chapter 4. The development of a comprehensive methodology is described in Chapter 5 for processing the VLA data. This chapter is also dedicated to show the development of the integrated velocity structure model coming from different inversion techniques. The next chapter presents the results of the amplitude studies using the Bayesian inversion approach. Chapter 7 is dedicated to integrate the results of the different travel time inversions with the amplitude inversion and to compare this integrated model with previous velocity studies from the study area. This chapter also shows an assessment of the performance of the VLA in comparison with the previous, conventional seismic data for imaging structure in the gas hydrate stability zone. Two possible scenarios of the hydrate formation around the VLA in MC798 are presented, based on the new results and the information learnt from previous experiments. Finally, a short

summary, conclusions, and recommendations for future studies provided in Chapter 8 completes the dissertation.

Chapter 2

Natural Gas Hydrates

Natural gas hydrate occurs worldwide in oceanic sediment of continental and insular slopes and rises of active and passive margins, in deep-water sediment of inland lakes and seas, and in polar sediment on continents and continental shelves. In aquatic sediment in general, where water depths exceed about 300 m and bottom water temperatures approach 0°C, gas hydrate is found at the sea floor to sediment depths of about 1000 m. In polar continental regions, gas hydrate can be present in sediment depths between about 150 and 2000 m. Natural gas hydrate is restricted to the shallow geosphere where its presence affects the physical and chemical properties of near-surface sediments. The global inventory reports on natural gas hydrate recovered from several places worldwide and includes 77 places where the presence of gas hydrate has been inferred from geophysical, geochemical, and geological evidence.

The potential amount of methane in natural gas hydrate is enormous, with current estimates converging around about teratonnes (10^{19} g) of methane carbon [45].

2.1 Definition

Natural gas hydrate is a solid substance composed of water and natural gas (mainly methane). The water molecules are arranged in a rigid framework of cages (called clathrates, Fig. 2.1), many of which are occupied and stabilized by a molecule of methane.

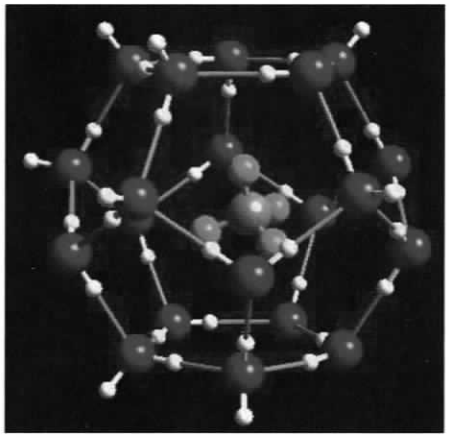

Figure 2.1: *Gas hydrate clathrate. Clathrate hydrates constitute a class of solids in which the guest molecules occupy, fully or partially, cages in host structures made up of H-bonded water molecules. The usually unstable empty clathrate is stabilized by inclusion of the guest species. In the case of guest molecules which are gaseous at ambient conditions the resulting clathrate hydrate is often called a gas hydrate, after Kvenvolden [45].*

The physical chemistry of methane is well known [70], and the occurrence of gas hydrate is controlled by interrelations among factors of temperature (T), pressure

(p), and composition of gas and water [43]. The upper depth limit for methane hydrate is about 150 m below the surface in continental polar regions, where surface temperatures are well below 0°C (273 K). Generally in oceanic sediment, gas hydrate occurs where bottom-water temperatures approach 0°C, and the water depths exceed about 300 m. The maximum lower limit of methane hydrate occurrence is determined by the geothermal gradient; this lower limit is about 2000 m beneath the continental surface and the ocean floor, although the depths of occurrence are typically less than 1000 m, depending on local conditions [62]. However, the P-T conditions (Figure 2.2) in which these gas hydrate exist are strongly dependent on the gas composition.

The occurrence of natural gas hydrate is restricted to the shallow geosphere where the amount of methane exceeds its solubility in water and thus is present in large enough quantities to form methane hydrate. Methane comprises more than 95% of the hydrocarbon gases in most natural gas hydrate. Worldwide, the most common crystal structure is known as Structure I [70]. In the Gulf of Mexico [5], Caspian Sea [75], [30], and Mackenzie Delta [10], gas hydrate has been recovered in which methane is accompanied by significant amounts of ethane and propane; this gas hydrate has Structure II crystallography [70]. Structure II gas hydrate with even higher molecular weight hydrocarbon gases has also been suggested in the Gulf of Mexico [62]. Minor quantities of CO_2 and H_2S are often present. A Structure I methane hydrate containing 10% H_2S has been recovered from the Cascadia Margin offshore Oregon

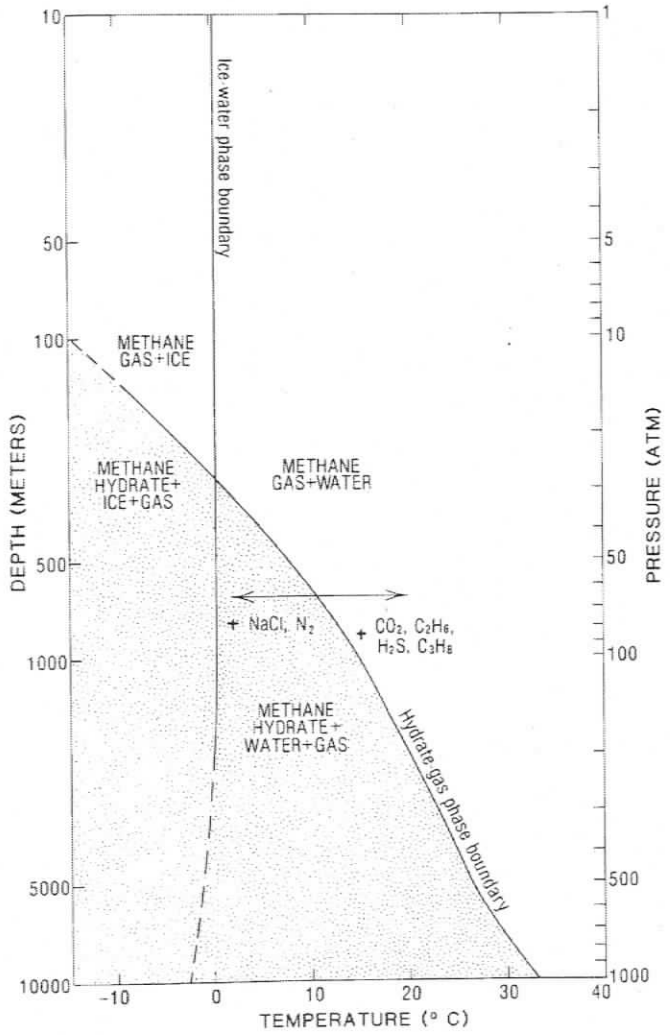

Figure 2.2: *Gas Hydrate phase diagram, showing the stability fields of the water-ice-methane-hydrate system. The presence of CO_2, H_2S, ethane and propane with methane in the hydrate has the effect of shifting the hydrate phase boundary to the right, thus increasing the P-T field within which methane hydrate is stable. Thermal stimulation has the effect of moving any point on the diagram to the right, while depressurization moves any point upwards. Inhibitor stimulation, for instance by NaCl solution, shifts the hydrate phase-boundary curve towards the left. Gas will be produced as a result of any movement of a P-T point, if its new position is to the right of, or above, the gas-hydrate phase boundary, after Kvenvolden [45].*

[39].

In many parts of the world, natural gas hydrate is formed from biogenic methane, excreted by bacteria that eat organic matter that has been washed into the ocean. This type of hydrate is concentrated where there is a rapid accumulation of sediments (which protect detritus from oxidation). Scientists believe that this non-concentrated bacterial action results in formations in which hydrates are relatively evenly distributed throughout other rocks or sediments. If detritus is concentrated, however, hydrates of biogenic origin can form layers that may be mixed in with or separated by sediments.

Hydrates can also form when faults permit natural gases (or other gases) to migrate from deeper inside the Earth's crust to the surface of the seabed at places with appropriate temperature and pressure levels. They may form sea floor mounds near the fault, or they may spread out from the fault and effectively seal it, preventing more methane from rising to the surface.

2.2 Oceanic Gas Hydrates and the Hydrate Stability Zone (HSZ)

Where conditions are suitable, oceanic gas hydrates occur in a surface-parallel zone of thermodynamic equilibrium (the hydrate stability zone: HSZ), which extends

downwards from the sea floor to a depth defined by the geothermal gradient.

Within this zone, the conductive transfer of heat between the warmer rocks below and the cold oceanic waters above is in equilibrium within the pressure-temperature field at any particular depth; thus, heat entering the base of the HSZ is conducted upwards and is dissipated into the sea, thereby maintaining conditions of hydrate stability throughout the HSZ.

Hydrates are known to occur in a wide variety of sediments, whose precise lithology (i.e. whether calcareous, siliceous, or clay-mineral rich) seems to be relatively unimportant. Optimum conditions for the formation of hydrates are found in thickly-sedimented areas on continental slopes and rises, where large volumes of gas can be generated or accumulated. Whether produced biogenically or thermally at greater depths, this gas may migrate upwards into the HSZ. Hydrates in the HSZ may fill the available porosity, and render an otherwise uncompacted and unconsolidated sediment solid.

Where present as a cementing blanket within sediment, hydrates may provide an impermeable seal, and therefore trap large volumes of gas. Hydrates can be reworked through a gasification and rehydration process, here termed the gas-hydrate conservation cycle, which provides a long-term, nearly steady-state mechanism for concentrating gas in an area of sediment deposition.

Sedimentation on the sea floor would tend to bury the hydrate were it not for

the influence of the heat flow from below. As sedimentation proceeds, the surface of the sediment moves upwards and the base of the HSZ follows, so that the thickness of the HSZ tends to remain constant. The key to this conservation cycle is that the base of the HSZ represents a metastable phase boundary between the gas-hydrate and gas-and-water fields, which is controlled by pressure and temperature (possibly locally modified by geochemical conditions). Thus, when hydrates at the base of the HSZ become unstable, owing to the upward migration of this zone of stability, they dissociate and invert to gas, which rises buoyantly upwards. Apparent fault offset of the hydrate-gas contact suggests that the zone of equilibration may be broad. In a thick sedimentary pile, gas may be reworked in this cycle many times. This reworking of hydrate at the base of the HSZ, combined with the influx of gas migrating from below, explains why the base of the HSZ has been observed to be the most heavily hydrated section. The HSZ is therefore stable in the upper portions of the sediment near the sea floor, even in areas where substantial sedimentation rates occur and where there is only little or moderate generation of gas. Once formed, gas hydrates will not become buried within the sedimentary pile.

2.3 Gulf of Mexico Sea-Floor Stability and gas hydrate presence

In the Gulf of Mexico, which is an area with extreme shallow salt movements and free gas presence, the depth and temperature values can be quite different from the average values observed at other deep sea locations. Gas hydrates in the Gulf of Mexico occur at or just beneath the seafloor, in water depths exceeding about 400 m and at 4°C water temperature [51].

In the Gulf of Mexico, gas hydrate mounds form along the intersections of faults with the sea floor. These hydrate containing mounds include of water from the sea and thermogenic hydrocarbon gases that have migrated up the faults from buried reservoirs. In addition to gas hydrates, they also contain various minerals deposited by bacteria feeding on the hydrocarbons. The mounds are ephemeral, capable of changing greatly within a matter of days. Many geoscientists familiar with recent geologic processes in the Gulf of Mexico think that events which produce changes to the hydrate mounds also trigger episodes of sea-floor instability [51].

Variations in the pressure, the water column temperature distribution, the chemical composition of the gas and the rate of gas flow combine to determine whether hydrates within the mounds accumulate or dissociate. Major influences are the warm eddies of water that separate from the Loop Current (Figure 2.3), a major current

that runs northward near the Yucatan Peninsula and eastward through the Straits of Florida, and raise bottom temperatures in the northern Gulf of Mexico by as much as 2-5 °C. The result is a quasi-cyclicity of sea floor hydrate formation that is driven largely

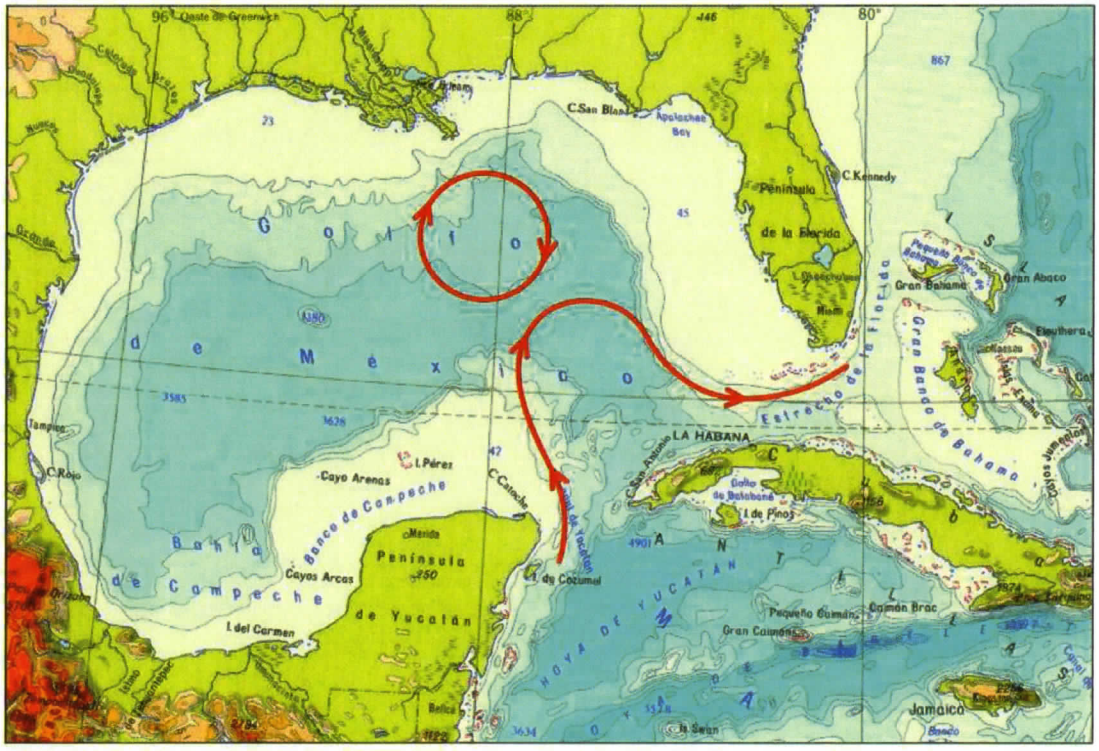

Figure 2.3: *Gulf of Mexico Loop current after Paul Mitchel.*

by these current-induced temperature variations of bottom waters. Changes in pressure, salinity, gas composition and flow rate that can also contribute are not well understood, but many changes are due partially to tectonic activity associated with

salt movement.

Hydrates contained in sediments are stable as long as the sediments are within the hydrate stability zone (HSZ) as defined by pressure, temperature and chemical composition. If hydrocarbon gases migrating up faults encounter sediments of sufficient permeability that lie within the HSZ, hydrates can form within the pore spaces and support the sediment frame. This increases the sediment's shear modulus and thereby its bearing capacity. As continuing sedimentation increases their depth of burial, hydrate-bearing sediments within the HSZ are subjected to successively higher temperatures and pressures until they eventually are more across the base of the HSZ. When this occurs, the hydrates in the pore space cementing the sediments dissociate, their bearing capacity decreases and a potential for sea floor instability is created. The same result can be produced by distortion of the geothermal gradient such as those caused by proximity to salt bodies or drilling activities [73]. Temporal factors also come into play because, over time, bacteria consume the methane released by hydrate dissociation, resulting in diagenesis and an increase in bearing capacity due to the cementation of sedimentary particles. Common indicators of bearing capacity are the speeds at which compressional (P) and shear (S) waves propagate below the sea floor and the efficiency of P-to-S conversion (PS) at reflecting horizons.

2.4 Evidence for Gas Hydrate:

Three kinds of evidence can be used to identify the presence of natural gas hydrate: geological, geochemical, and geophysical. Geological evidence includes sediment properties, stratigraphic relationships, gas-migration pathways, and, most importantly, the actual recovery and description of gas-hydrate samples. Pore fluid chemistry and gas composition (molecular and isotopic) are important aspects of gas-hydrate geochemistry. Finally, geophysical evidence includes data from seismic reflection profiling, vertical seismic profiling, and various kinds of well-logging. In this study, different types of geophysical data are used to investigate the possible gas hydrate distribution at the survey area.

2.4.1 Geophysical Evidence

Most oceanic occurrences of gas hydrate are inferred, based mainly on marine seismic reflection profiles showing an anomalous bottom-simulating-reflector (BSR). This reflection coincides with the depth predicted from the phase diagram (Figure 2.2.) as the base of the gas hydrate stability zone. BSRs mark the interface between higher velocity, hydrate bearing sediment above and lower velocity sediment containing free gas below. The seismic reflection from the base of the gas hydrate is generally characterized by a reflection polarity reversal resulting in a negative reflection coefficient. The reflection usually mimics seafloor topography, often increasing in sediment depth

with increasing water depth [69]. Other indications of hydrate are sea-floor reflectivity changes, velocity changes, attenuation and sea-floor mounds. In addition to seismic data, combining geophysical information from various wire-line well logs can aid in the detection and evaluation of gas hydrate intervals [44]. Well logs for gas hydrate studies include caliper, gamma ray, spontaneous potential, resistivity, sonic velocity, and neutron porosity. The resistivity and sonic velocity logs have proved most useful in the study of gas hydrate. Well logs provide a basis for estimating gas quantity, and in conjunction with seismic data, they play a very important role of the future global gas hydrate assessments. In the petroliferous Gulf of Mexico, the lack of BSRs causes problems in the geophysical identification of gas hydrates. Laterally continuous BSRs only exist if the geothermal gradient does not vary horizontally. In the Gulf of Mexico, where the geothermal gradient is often influenced by near surface salt domes, diapirs and complicated geology, continuous BSRs are rarely reported.

2.5 Gas Hydrate Distribution at the Survey Area

The Gulf of Mexico presents a unique setting for gas hydrates when compared to most other continental margins of the world. Both oil and gas are actively produced in the Gulf, and abundant leakage (i.e. venting) provides a thermogenic source of gas to the shallow section for forming hydrates [61], especially much rarer forms of Structure II hydrate [63]. Hydrates in the northern Gulf of Mexico have also been characterized

primarily from studies of hydrate mounds on the sea floor [61] rather than the more commonly known seismic indicator of hydrates, the BSR. The absence of widespread BSRs is puzzling, given the abundant gas in the Gulf, although observations of BSRs in Walker Ridge [49] and elsewhere in the Gulf are now beginning to be reported. The few BSRs that have been observed in the northern Gulf are weaker and less recognizable when compared with the BSRs that characterize well-known gas hydrate regions such as Blake Ridge [14], Hydrate Ridge [72], northern Cascadia Margin [59] and Nankai trough [2].

The Gulf of Mexico is also unique because of the salt tectonics that occur. This widespread salt may be related to the paucity of BSRs in two fundamental ways. First, salt is an inhibitor to hydrate formation, so that the presence of abundant shallow salt on the continental slope may act to limit hydrate formation [57]. Second, the salt tectonics and related faulting and fluid/gas venting may also distort the base of the gas hydrate stability zone, limiting the subjacent accumulation of laterally continuous zones of free gas necessary for a recognizable BSR [9]. The complexity of the geologic setting together with the abundant hydrocarbon development are factors which set the Gulf apart from other hydrate settings.

Chapter 3

Geophysical data in Mississippi Canyon Block 798

Mississippi Canyon Block 798 (MC798) and Atwater Valley Block 14 (AT14) are situated along the upper continental slope in the northern Gulf of Mexico which is an area of diverse geologic processes and stress regimes. Many data-acquisition programs have included collection of information over MC798 and AT14. Both lease blocks are located on the continental slope of the northern Gulf of Mexico (Figures 3.1 and 3.2). The average water depth at the site in MC798 is 821 m and at AT14 is 1309 m.

In MC798 Neurauter and Bryant (1989) [53] recovered hydrate from a mud diapir in the block. MC798 has, in recent years, become of great interest to CMRET of the University of Mississippi. This interest is driven by the documented recovery of gas

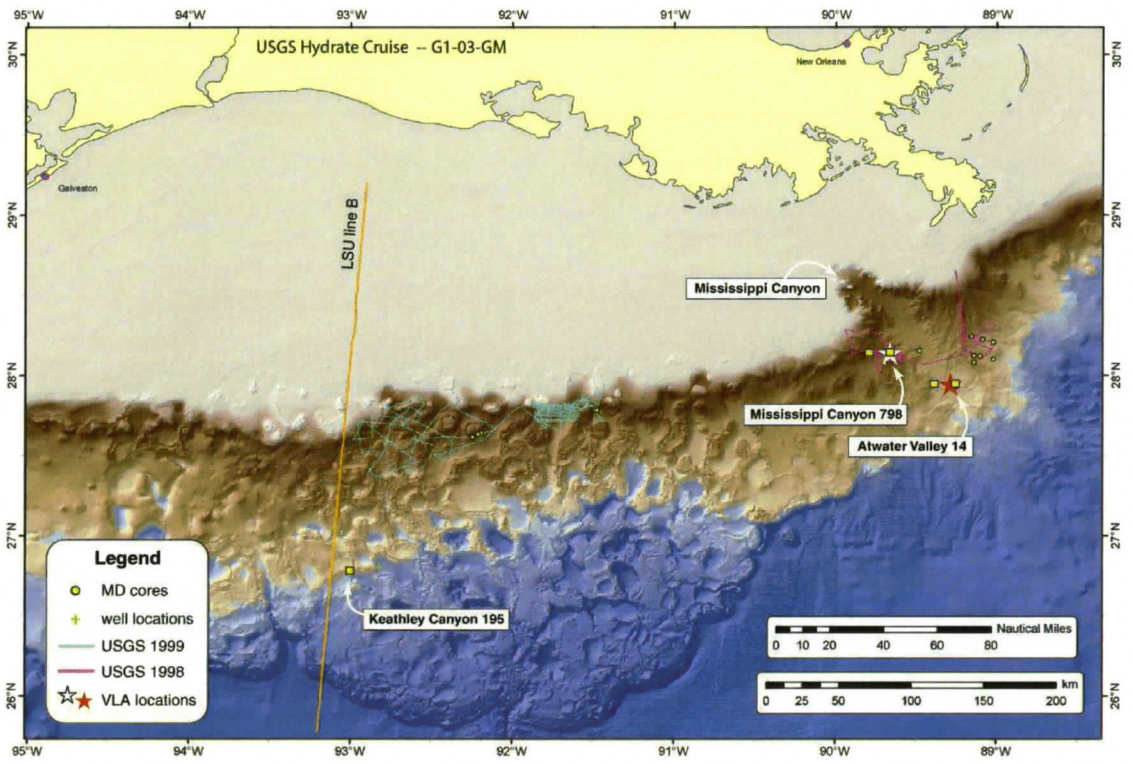

Figure 3.1: *Location of the experimental sites in the northern Gulf of Mexico (adapted from USGS Hydrate Cruise Report G1-03-GM, 2003).*

hydrate in the area. This chapter describes the geophysical data from experiments and surveys carried out at MC798. Figure 3.3 displays the line alignment at the survey area in 2002 and 2003 in relation to each other.

3.1 Heat Flow Data

Heat flow measurements at sites selected from seismic profiles over MC798 reveal substantial variation in heat flux. In one locality, heat flow at the base of a mud

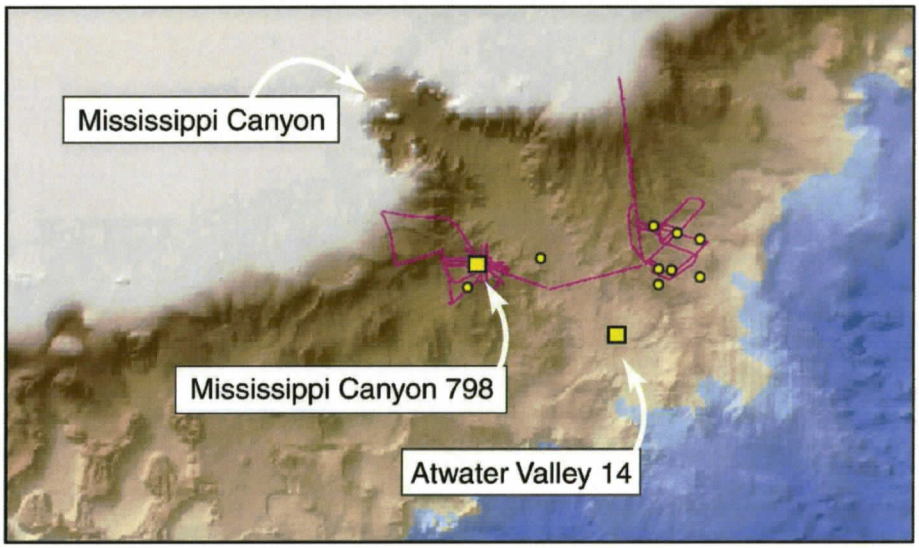

Figure 3.2: *Detail of Fig.3.1 showing locations of lease blocks Mississippi Canyon 798 and Atwater Valley 14 (adapted from USGS Hydrate Cruise Report G1-03-GM, 2003). The yellow circles indicate sites of 30 m sediment cores drilled by the Marion Dufresne experiments, and the purple tracks are the USGS (multi-channel) survey lines from 1998.*

diapir documented to contain hydrates [53] measured 10 times greater than that at its summit. A possible explanation for the extremes encountered is that faults near some measurement sites act as conduits for hot fluid rising from depths of thousands of meters [48]. However, it is not known if the hydrate reported in 1989 was still present during 2000 when the heat flow measurements were made. Episodic fluid-flow could well be a factor governing episodic hydrate formation/dissociation. There is evidence that a stream of dense brine about 1 m thick is flowing across the sea floor at or near this location (Trevor Lewis, consultant, reporting on heat-flow analysis, January 2001).

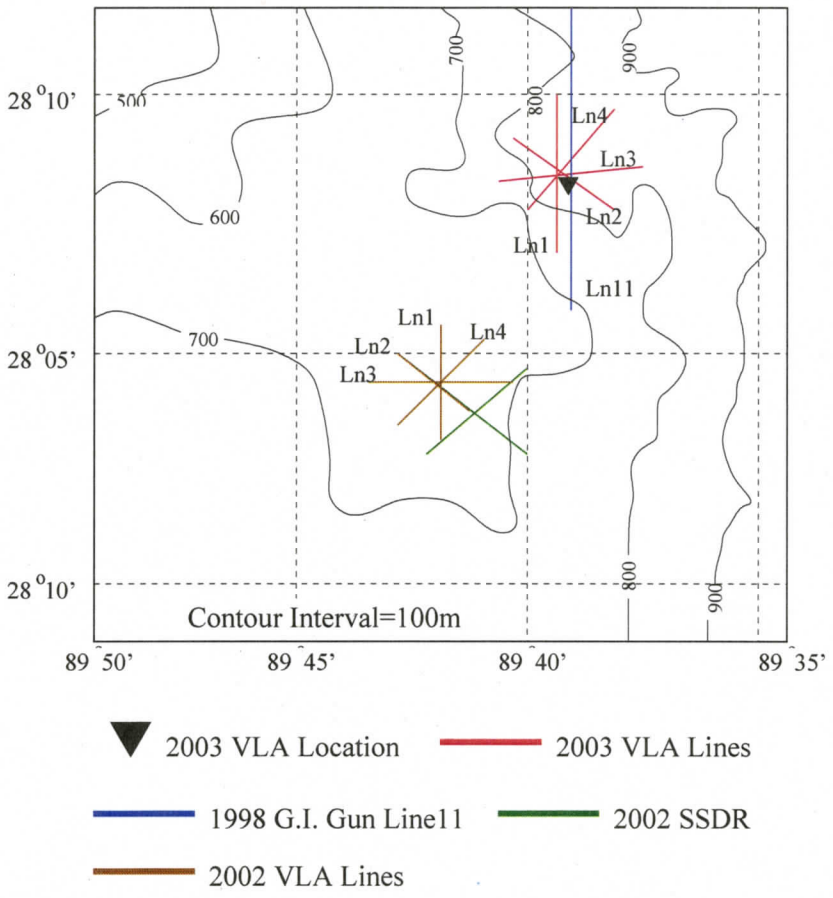

Figure 3.3: *Tracks of runs on the VLA site in Mississippi Canyon 798 in relation to the other surveys at the site.*

3.2 High-resolution Marine Seismic Data

For many years, the CMRET has been working on developing a new method of high-resolution seismic profiling. This method was based on very rapid sampling, also called oversampling, and the recording of source signatures for use during processing.

Both were crucial to achieving the required resolution for imaging the gas hydrate stability zone.

3.2.1 Recording the data

The amplitude and phase of seismic signals represent significant information. Subsequent processing can access this information only if the data are recorded digitally, and then only if the digitization has been done properly. There are two principal parameters to consider when digitizing a seismic signal: the digital resolution, i.e. the number of bits used to represent the analogue amplitude, and the sampling rate, i.e. the number of digital samples per unit time. Both affect the fidelity to which the analogue signal is represented. Increasing either or both serves to improve fidelity, but also increases the digital volume to be stored. The size of the data volume was a major concern when digital storage was expensive, but storage media are now so inexpensive that large volumes are no longer a problem. When digitizing a signal, the analogue gain is chosen such that the analogue signal voltages occupy most of the operational range without exceeding that range. Because the reflectivity of the sea floor can change significantly, unexpectedly increasing the analogue signal strength, it is conventional practice to choose the gain level so that the upper one or two bits of resolution are normally unused. This acts as a safety factor to allow reasonable increases in analogue signal strength without clipping the digital signal. A-D converters

using less than 16-bits are not really useful for practical seismic applications. Since reflection seismograms typically have higher amplitudes at shorter record times and significantly lower amplitudes at longer record times, it is often advisable to apply a TVG (time-varying gain) before digitization in order to avoid clipping the early arrivals but still record the later arrivals with reasonable digital resolution. Since it is necessary to account for the gain during processing, the TVG must be well calibrated or recorded as a separate channel. The use of TVG becomes unnecessary as the digital resolution increases. The current tendency in high-resolution work is toward 24-bit systems (which are, effectively, 21-bit systems allowing for sign and safety factor). Some digital streamers used for oil exploration have 32-bit resolution and 64-bit streamers are being discussed. If infinite digital resolution were possible, analogue gain would be entirely unnecessary. The second principal digitization parameter, sampling rate, is traditionally chosen according to a few conventional rules-of-thumb, discussed in the following section.

3.2.2 Bandwidth, digitizing rate and seismic resolution

It is a tenet of conventional seismic wisdom that seismic signals have limited band widths, i.e. that there is no power above some finite cut-off frequency. The consequences of this assumption dominate the practice of digital seismology because the minimum rate at which an analogue signal should be sampled is twice the cutoff fre-

quency. After digitization, one-half the sampling rate is the highest frequency (the Nyquist frequency) that the digital data can represent uniquely. Theory states that only signals of limited bandwidth may be digitized without loss of resolution. A generalized uncertainly principle requires that signals of limited bandwidth (such as a sinusoid) have infinite duration and that signals of limited duration (such as pulses) have infinite bandwidth [50]. The duration of seismic wavelets is limited because they are causal, i.e. they do not exist prior to their onset times. Thus their bandwidth is infinite. This presents a conundrum in practice because information theory requires an infinite sampling rate if resolution is not to be lost [68]. The implication is that at least some resolution is always lost when seismic signals are digitized, but the loss may be minimized by sampling as rapidly as possible. When a lower rate is desired, perhaps to limit data volume, the rate must be chosen that is adequate to provide the geologic information required.

When there are no good reasons to restrict sampling to a minimally adequate rate, the concept of oversampling offers good reasons for sampling much faster. Oversampling exploits the speed of modern A-D converters and the vastness of modern storage to define Nyquist frequencies so high that significant signal power at higher frequencies would be very improbable. Oversampling is well suited to seismic signals because the power of seismic wavelets decays naturally as frequency increases. Therefore it is not difficult to select a Nyquist frequency that is several octaves above the highest

frequency of interest, i.e. above the upper limit of the effective bandwidth. This promotes increased resolution both by avoiding losses associated with severe high-cut filtering prior to digitization and by improving signal coherency during digital processing.

3.3 Two-dimensional Conventional Seismic Data

In June 1998, the Marine Minerals Technology Center (MMTC, University of Mississippi) and the U.S. Geological Survey (USGS, Menlo Park) conducted an eleven-day cruise in the Mississippi Canyon region of the Gulf of Mexico where gas hydrates are known to occur in the shallow subsurface and, in some places, outcrop at the sea floor. The purpose of the cruise was to collect seismic data using a variety of systems in an effort to ascertain the best collection method(s) with which to study such regions, the ultimate goals being to characterize shallow gas hydrate stability zones by seismic means, to identify related subsurface features which might affect the stability of the sea floor and to estimate hydrate quantity within the shallow subsurface. The cruise was conducted onboard the R/V Tommy Munro owned and operated by the Gulf Coast Research Laboratory of the Institute of Marine Sciences at the University of Southern Mississippi [8]. Seismic profiling equipment was provided by both the USGS and the MMTC. Seismic sources were fired at standard energy levels and rates. Only one system was used at a time to avoid acoustic cross talk. All data were recorded

digitally. A total of nearly 50 gigabytes of data were recorded. Ocean-bottom seismometer (OBS) three-component instruments, leased from Dalhousie University, were also deployed.

3.4 Single-Channel Surface Source Deep Receiver Seismic Data (SSDR)

In 1999, the CMRET took the lead role in establishing the Gulf of Mexico Hydrates Research Consortium, which has, as its primary objective, the emplacement of a permanent seafloor station designed to monitor the activities of gas hydrates on the sea floor on a more or less continuous basis. The heart of the monitoring station is a network of VLAs of hydrophones. The primary purpose of the 2002 cruise was to acquire seismic data using a single prototype VLA. A secondary goal was the simultaneous collection of seismic profiles with which the sub-bottom configuration imaged by the vertical array can be compared. (The cruise configuration is shown schematically in Figure 3.4).

3.4.1 Objectives

In June of 2002, scientists from Specialty Devices, Inc. (fabricators of the VLA) and CMRET scientists embarked on a 5-day cruise on board the RV Pelican. This trip

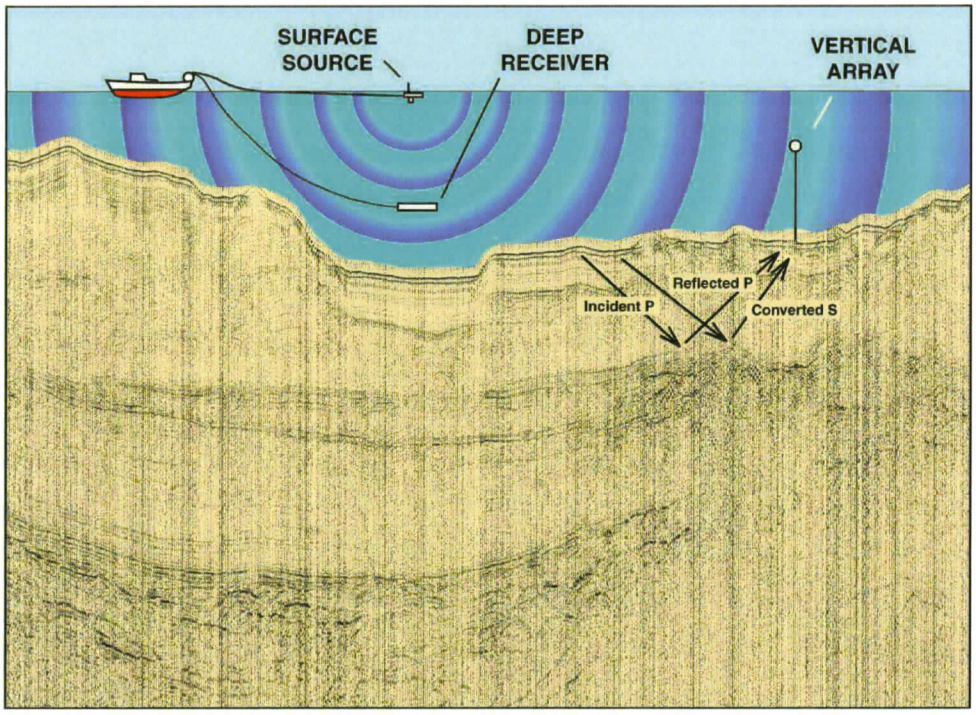

Figure 3.4: *Illustration of the vertical array testing with the surface-source deep-receiver (SSDR) horizontal profiling in 2002 by the CMRET.*

was designed to accomplish several tasks:

- to moor a 16-channel VLA prototye on the seafloor and to retrieve it,
- to run a pattern of ship tracks across the moored array, firing an 80 in^3 watergun at the sea surface,
- to collect seismic profiles, using the same source, and with a deep-towed receiver (the so-called shallow-source deep-towed receiver, or SSDR, technique), and

- to rerun two track lines across the VLA, using only the ship's noise as a sound source for the hydrophones.

The June 2002 cruise aboard the R/V Pelican resulted in two successful deployments and retrievals of the VLA, but due to electrical complications and failures, no data were retrieved.

Specialty Devices, Inc. completed the necessary repairs to the VLA by August. The MV Ocean Surveyor, was retained and a repeat cruise was completed during the final week of August, 2002.

The primary objectives of the research teams were achieved. Since time was available, two additional objectives were met:

- to run two orthogonal 6 km SSDR profiles over the site where the USGS had successfully retrieved a 28.35 m core in the southwestern flank of the block from the Mississippi Canyon 798, and

- to run two orthogonal 6 km SSDR profiles across a sand body thought to span the base of the hydrate stability zone.

The SSDR consisted of an 80 in^3 water gun source towed at the surface behind the support ship and a streamer, towed at depth (30m), as near to directly under the source as possible. The SSDR data were recorded every 9 s for a duration of 5 s while VLA data recording was done every 18 s for 9 s. The 80 in^3 watergun was

replaced with a reserve gun of the same volume when leakage caused the signal to deteriorate. The data obtained with the SSDR system were subjected to preliminary processing. The data from Atwater Valley Block 14 were not used in the comparison study with the VLA data. The 2-D conventional seismic AT14 dataset was processed and the results are shown in Appendix A. The reason for not using these data will be discussed in detail later in this chapter.

3.5 Vertical Line Array Data Acquisition

Conventional seismic techniques often fail to image the complex geological features, especially around and under salt domes and sills or in the presence of gas hydrates that have high propagation velocities. The conventional 2-D marine seismic survey generally acquires several lines over the target area. The source vessel pulls the streamer carrying receivers positioned on the same line where the source is activated. Thus, source-receiver azimuths follow the direction of those 2-D lines. This means that all the energy spread away from the 2-D profile is missed. Missing energy is responsible for the lack of illumination in most targets under complex geology. Therefore, new techniques in data acquisition and processing are sought to improve the image of complex areas.

One of the new seismic data acquisition techniques is the VLA. This new method deploys hydrophones attached to a vertical cable that is anchored to the sea floor (or

also can be suspended from the sea surface). Once the cable is deployed, a seismic source on a small survey boat is fired in a large surface grid over the cable. With the unconventional acquisition geometry, the VLA data can not be treated directly by the conventional procedures of seismic data processing. Therefore, new algorithms had to be created.

3.5.1 Vertical Line Array Overview and Advantages

The basic idea of the VLA technique is to use the receivers (piezoelectric hydrophones) in a vertical configuration, instead of horizontal, which is the usual case in marine seismic acquisition. Maintaining electrical and mechanical integrity of the cables and hydrophones under high hydrostatic pressure is a significant issue [41]. The cable is kept in the vertical position through the use of buoys at the top and a weight at the bottom. The array can be free floating or, as in the case of this study, moored to the sea floor anchor. The VLA techniques would be most similar to a marine walkway vertical seismic profiling (VSP), with the obvious difference - and advantage - of not requiring a drilled well. The walkaway VSP is a type of vertical seismic profile used on land in which the source is moved to progressively farther offset at the surface and receivers are held in a fixed location, effectively providing a mini 2D seismic line that can be of higher resolution than surface seismic data and provides more continuous coverage than an offset VSP. The VLA technique is also based on Navy antisubmarine

warfare technology from various countries.

In comparison to conventional acquisition such as streamer and ocean bottom cable techniques, the vertical cable advantages summarized and reported in abstracts by several authors are [40], [42], [1], [46], [65], [27]:

- lower background noise due to the deeper hydrophone depths and the elimination of flow noise from the towed streamer,
- the acquisition is less susceptible to weather conditions that affect survey operations, which is very important in places like North Sea, off West Africa and the storm zone of Southeast Asia,
- up- and down-going waves can be separated,
- a less rigid and easier to reconfigure geometry is possible, which is especially important when 3-D pre-stack migration is used,
- as several azimuths are sampled, true 3-D imaging is possible with several VLAs,
- no common mid-point assumption is used (this is a major concern in Gulf of Mexico sub-salt imaging), as the data are 3-D pre-stack migrated,
- on small scale 3-D surveys, costs are considerably reduced, as smaller boats can pull the source, eliminating the large distances required for turning a vessel pulling long streamers,

- the coverage is better as the boats can get closer to any obstruction,
- 3-D pre-stack depth migration is less expensive than on streamer data,
- It also provides an opportunity for direct separation of up-coming and down-going wave fields in comparison with vertical seismic profiling where the wave-field separation can be only done in the frequency domain,
- for complex geologic structures, a more uniform distribution of reflection points from an interface can be obtained. A higher resolution, when compared to streamer data, is claimed for this technique, but the reason presented for this (less noise at higher frequencies) may not occur on some environments.
- Another great advantage is the possibility of acquisition in areas where the sea bottom has an oil and/or gas production line on it, which may cause the use of ocean bottom cables to be difficult, if not impossible. Reefs on sea bottom, including cold water carbonates (generally present on deep to very deep water) may also prohibit the use of bottom cables.

3.5.2 Vertical Line Array Survey

During August 2002 and October 2003, the CMRET conducted research cruises on-board the R/V Ocean Surveyor and R/V Pelican operated by the Louisiana University Marine Consortium. The purpose of the cruises were to deploy the prototype VLA

and record seismic data in survey tracks centered on the VLA. The VLA is a prototype hydrophone array developed as a component of the proposed Gulf of Mexico sea-floor gas-hydrate monitoring station.

The intention of the cruises was to collect high-resolution seismic data for use during development of software for analyzing monitoring station data. Two seismic acquisition techniques were carried out. One was an 80 in^3 watergun towed behind the R/V Pelican at the sea surface and the other was the noise of the R/V Pelican itself running at full speed. On survey tracks with the watergun, it was intended to tow a single-channel hydrophone several hundred meters below the gun to collect zero-offset seismic reflection profiles simultaneously with the VLA data. Use of this recording geometry, dubbed the SSDR technique, allows the source signature to be recorded for each shot so that it can be used to improve resolution during post-cruise digital processing. Unfortunately, the deep-tow cable developed a major electrical fault and it was not possible to record SSDR profiles on the 2003 deployment.

3.5.3 The prototype Vertical Line Array

A schematic of the prototype VLA is shown in Figure 3.5. It has a total length of 187.5 m. It is supported in the water column by glass-sphere flotation and is fixed to the sea floor by an expendable concrete anchor connected by acoustic releases. The upper portion of the VLA consists of 16 channels evenly spaced at 12.5 m intervals.

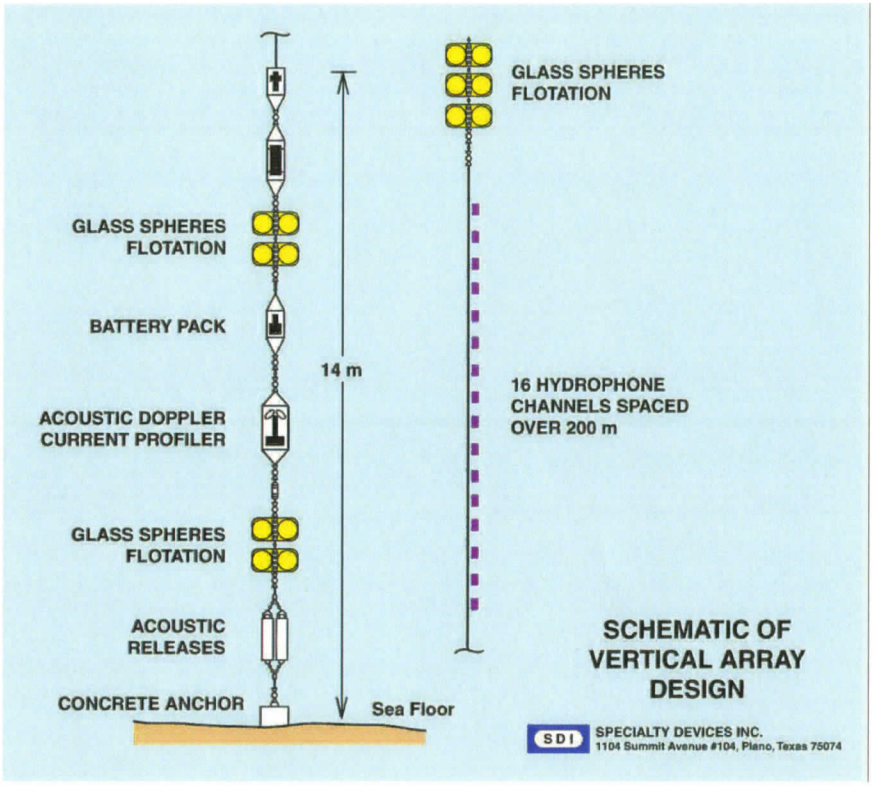

Figure 3.5: *Schematic diagram of the prototype VLA deployed in 2002 and 2003 by the CMRET.*

Each channel comprises a single hydrophone and preamplifier. One preamplifier was set to lower gain than the other 15 to insure a non-clipped recording of the direct arrivals even at short offsets. This was done because data collected on the initial VLA test cruise (August, 2002) exhibited some direct arrivals that had been clipped, making them unusable as source signatures. The lower portion of the VLA accommodates electronic devices in the pressure housings. These include a data logger, a battery pack, an acoustic-doppler current profiler (ADCP) and acoustic releases to disengage

the anchor. All 16 hydrophone channels are analog wired to the data logger which includes a data acquisition and telemetry system (DATS). The signals are further amplified by a programmable gain amplifier before each channel is digitized to 16 bits at 10,000 samples per second. A recording of 2-10s is stored in memory before being transferred to a hard drive following each shot. The DATS is connected to a two-way acoustic modem operating at about 38 kHz and capable of 1200-baud communications. This modem is used to receive a command to start recording data. The modem is also used to monitor the DATS house-keeping status, transmit compressed sample record information, provide surface control of acquisition parameters including gains of the programmable amplifiers and, if requested, transmit a recording for quality analysis in near-to-real time. A pressure-compensated battery pack mounted below the data logger provides all system power for up to a 10-day deployment. Energy conservation includes power control of the hydrophone array, signal conditioning circuitry and hard drives. An ADCP meter is located below the battery pack. The current profiler is directed upward to aid in determining the geometric configuration of the VLA in the water column. Recovery of the system is initiated by activating a pair of acoustic releases that connect the VLA to the expendable concrete anchor. Only one of two is required to release the anchor successfully. The glass spheres then provide sufficient buoyancy to bring the entire system to the sea surface.

3.5.4 Vertical Line Array survey design

During the VLA deployment, ship runs were made while firing a surface-towed 80 in^3 watergun. The idea of the general pattern of the runs for 2002 and 2003 is shown in Figure 3.6 displays the line alignment at the survey area in 2002 and 2003.

After the survey, several inaccuracies in the VLA positioning and data collection were discovered. The VLA position was calculated using a standard triangulation technique. This results from this process showed that there was 30 m difference between the triangulated position and the position where the VLA was dropped into the water. This change is expected between the deployment position and the actual sea-bottom location in any VLA survey (Paul Higley, personal communication, 2006). The array was deployed at 28° 08.1180'N, 89° 39.6696'W about 30 m (South-East) away from the crossing point of the lines.

The other issue was the timing errors on the data. Therefore, a time based error calculation was needed. The reason for these time inaccuracies was that the times were recorded at two places and the arrival times were different. The time base on the VLA and the boat was not properly calibrated to each other and differed. This timing error influenced the proper arival times of the data. After this was realized, it was decided that to be able to correct this error it was needed to calculate the theoretical travel times to take the data back to the correct time 0. Ray tracing was done using a conventional ray tracing method. Basically, the program used the

sound speed profile, the depth of each receiver, the VLA position and calculated the theoretical direct wave in the given range. The ray-tracing program determined the time t and ray parameter p to connect source at depth and receiver at depth separated by a given range, with sound speed points consisting of depths z, sound-speeds c, and gradients. The program is solving the travel-time equation and also takes into account the turning rays and direct path. The ray tracing had to be done separately to each receiver because the error was different for each receiver in the VLA [18].

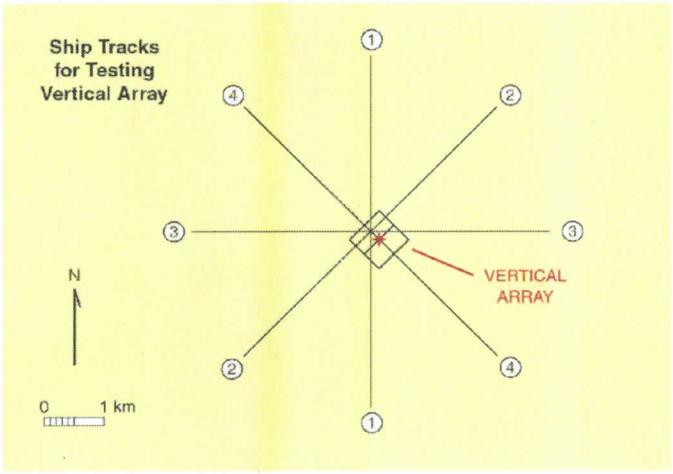

Figure 3.6: *Possible track line schematic of the 2002 and 2003 VLA cruise from Mississippi Canyon 798.)*

Waveforms recorded from one shot of the watergun are shown in Figure 3.7. Acoustic waves in Figure 3.8 are seen to sweep across the array, impinging on the sensors at slightly different times. Downward-traveling waves impinge first on the top of the array. Those that impinge first on the bottom are traveling upward.

The left-most wave in Figure 3.7 is propagating downward. It is the wave that has traveled directly from the source to the VLA. It can be seen that the direct wave is clipped, i.e. its amplitude exceeds the saturation level of the A/D converter. This could have been avoided by reducing the gain applied prior to digitization, but then the amplitudes of later arriving waves may have been unacceptably weak. Rather than take that chance, it was decided onboard ship to accept the direct wave being clipped.

The upward-propagating wave that follows the direct wave is the reflection from the sea floor. Other upward-propagating waves arriving later than the sea-floor reflection are subbottom reflections. The downward-propagating waves on the right-hand side of Figure 3.7 are first-order multiple reflections in the water layer, i.e. they are downward-traveling sea-surface reflections of waves that had been traveling upward from reflectors at and below the sea floor. Figure 3.8 shows detail of the upward traveling waves reflected from the sea floor and a sequence of sub-bottom layers.

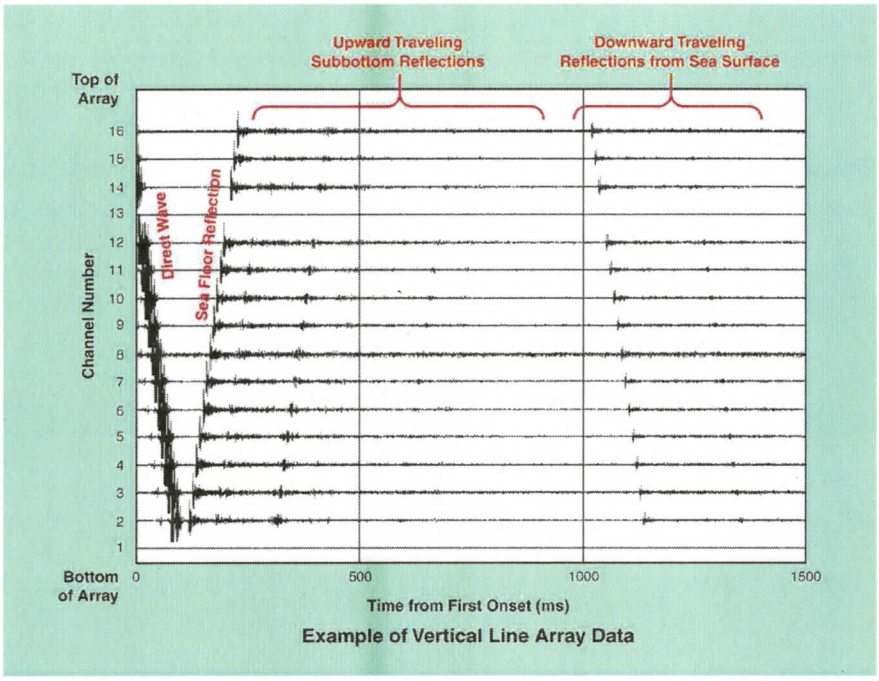

Figure 3.7: *VLA data example from the MC798 dataset.*

3.5.5 Vertical Line Array data coverage

In the vertical cable technique the receivers record two different wave-fields that can be migrated to form two images of the sub-surface: the up-coming and the down-going wave-fields. Figure 3.9 shows the differences between these fields. The down-going field is related to an intercepted water multiple. The VLA makes use of the water surface reflected signal, as seen in Figure 3.9, in the water reflected path near the receiver. The up-coming and down-going fields produce quite different sub-surface coverage, depending on the depth of the target and the position of the receiver in the

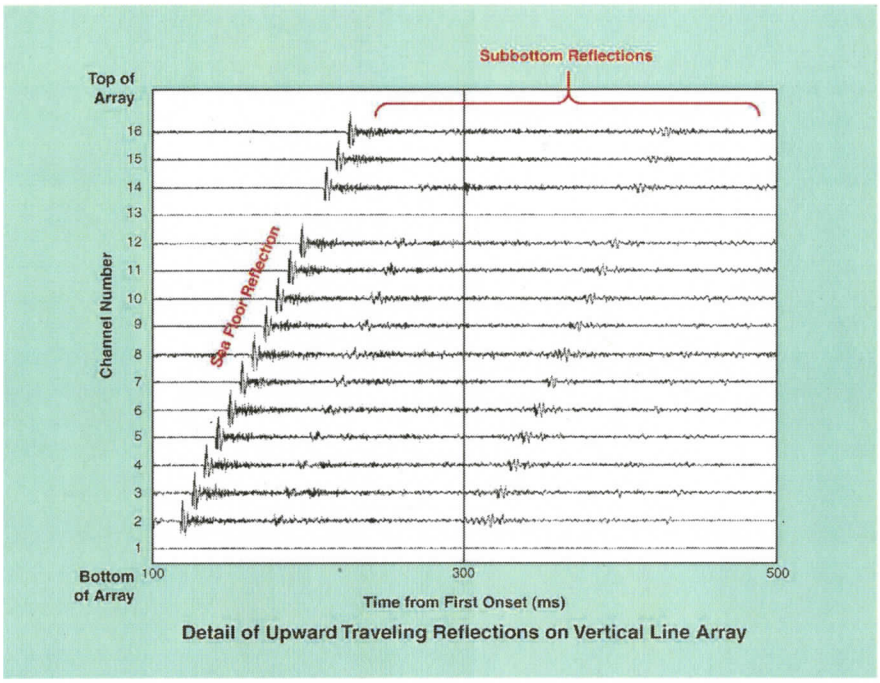

Figure 3.8: *Detail of upward traveling reflections on the VLA from the MC798 dataset.*

water layer.

The coverage, or the seismic illumination, generated by each receiver over the sub-surface will vary according to its depth in the water. Figure 3.10 shows three different receiver depths with up-coming field trajectories. The shallowest receiver in the water produces the largest lateral coverage. This is more noticeable on reflector one. Although the deepest receiver has the advantage of being in a quieter environment in the water, it has the drawback of possessing the least lateral coverage for the up-coming field, especially for the shallowest reflections.

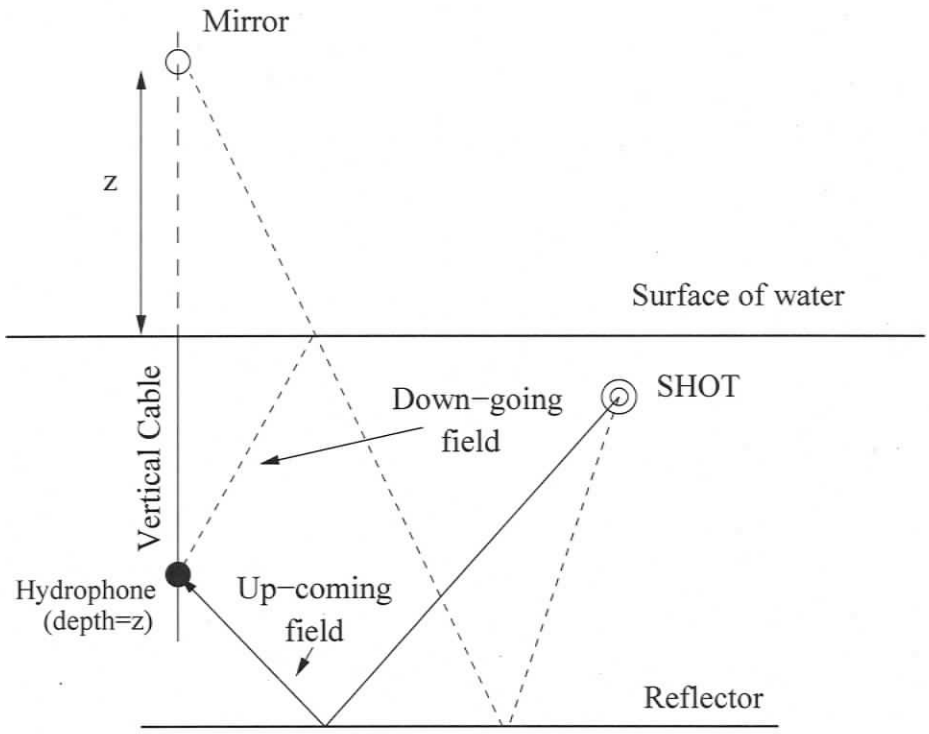

Figure 3.9: *Trajectory of up-coming (solid line) and down-going (dashed line) rays. Notice that for the same offset the down-going ray samples the sub-surface farther from vertical cable location than the up-coming ray. The projection of the receiver over the surface of the water shows why the down-going field is called mirror reflection.*

As the cable is anchored at the sea bottom, for a fixed cable length, the shallowest receiver controls the maximum lateral coverage for the up-coming wave-field.

The left panels in Figure 3.11 show the difference of up-coming and down-going rays in illuminating reflector one for receivers at two different levels. The right panel in Figure 3.11 shows the same effect but it is not so pronounced as for reflector two that is deeper than reflector one. The figures demonstrate that for deep water, the

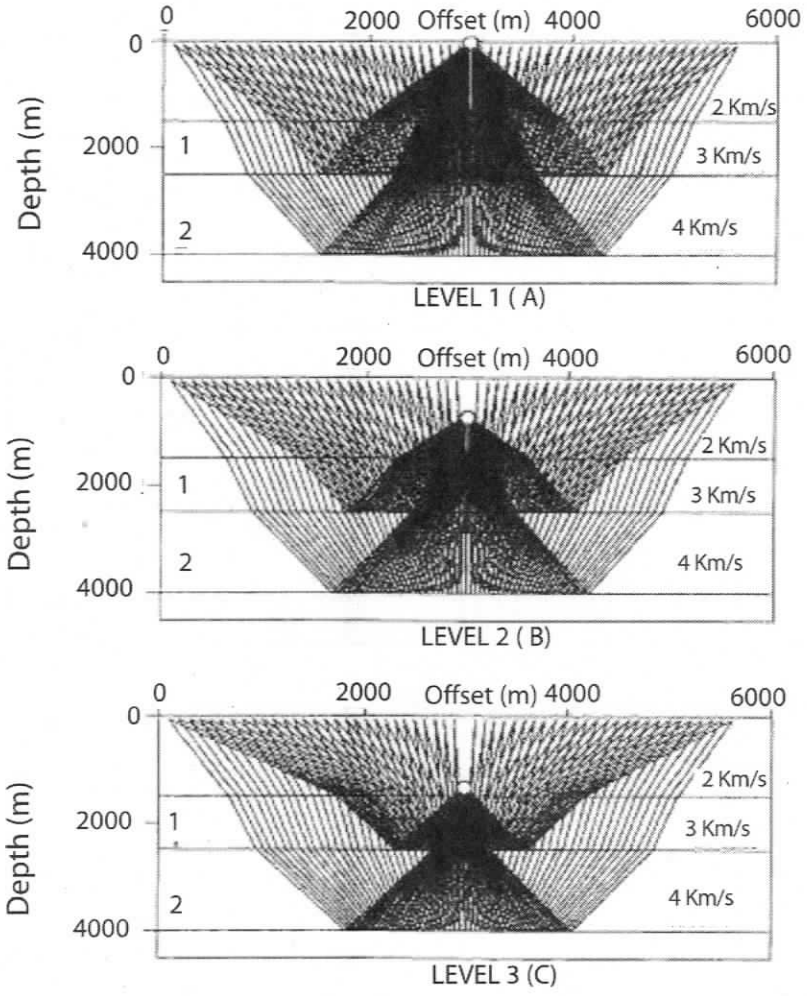

Figure 3.10: *Ray-tracing for three different receiver depths over a three-interface model. For the up-coming field the shallowest receiver in the water produces the largest lateral coverage, after Guimareas, 1998.*

coverage of the down-going field extends further laterally than that of the up-coming field, especially for the shallow horizons.

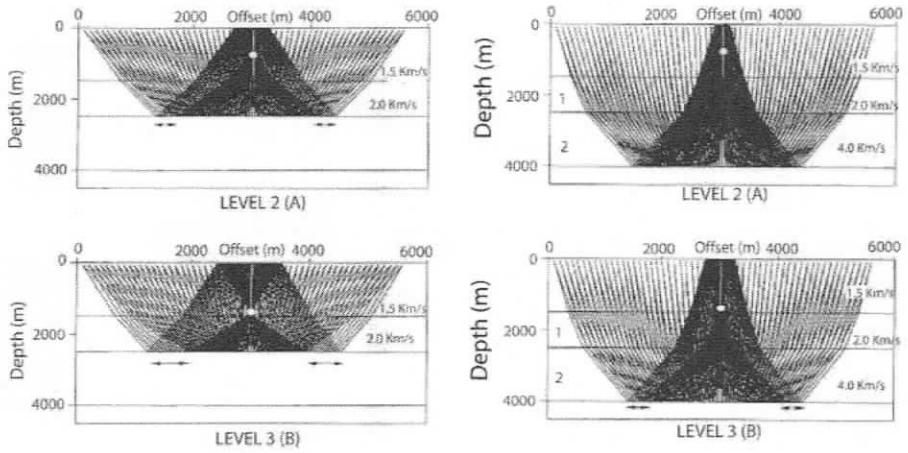

Figure 3.11: *Left image represents the down-going field extending the coverage laterally on reflector 1 compared to the up-coming field. Right figure represents the down-going field extending the coverage laterally on reflector two, after Guimareas, 1998.*

The up-coming field produces a denser sampling of the sub-surface. Dense sampling is required in areas of steep dip structures to avoid spatial aliasing. The acquisition planning of the vertical cable geometry has to account for the seismic coverage of the sub-surface [31].

3.5.6 Associated measurements

- **Sound Speed Profile**

  Since post-cruise processing would require knowledge of the speed of sound in

the water column, CTD (Conductivity-Temperature-Depth recorder) casts to measure conductivity, temperature and depth as a function of depth were made at each of the VLA deployment sites. Seabird software was used to calculate the speed of sound profile in the water column from the measurements. The results of the calculations are shown in Figure 3.12.

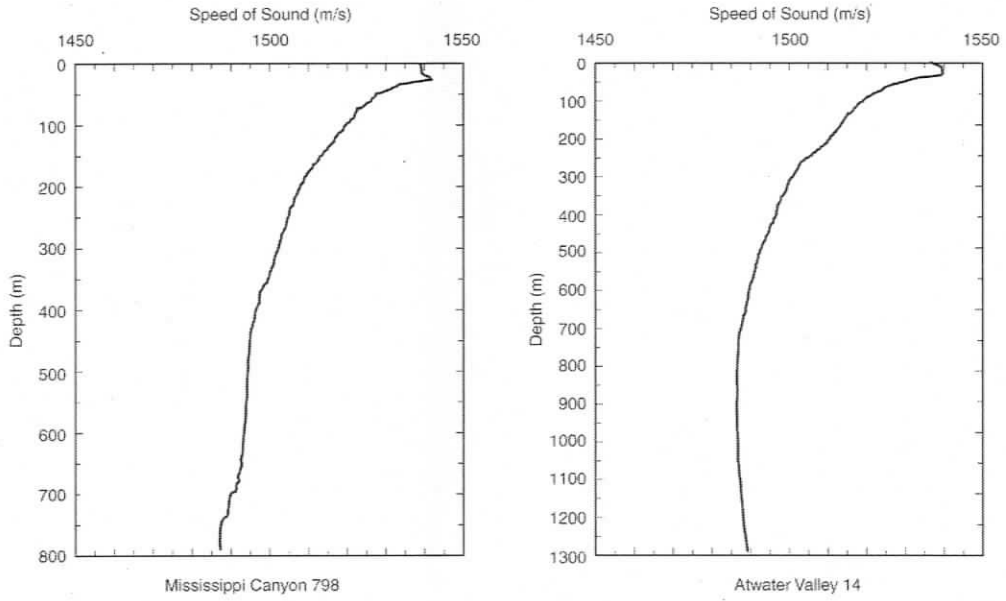

Figure 3.12: *Speed of sound profiles calculated from CTD casts for the 2003 deployment. These data were used in the ray tracing process.*

- **Acoustic Doppler Current Profile**

  An ADCP was deployed to measure the current along the VLA in the 2003 deployment (Figure 3.13). The ADCP was deployed at the base of the VLA

only in MC798, the water depth in AT14 being too great for its pressure housing. The ADCP was directed upward to determine any geometry/shape change of the vertical cable due to any water current. The current and the possible array shape change due to the current could drastically influence the depths and the positions of each individual receiver, and consequently impact each post-processing procedure. Therefore, this was a very important issue and needed to be investigated. In order to model the effect of current on the shape of the VLA, the current versus depth data was entered into a program by Speciality Devices Inc. along with the technical details about the VLA (weight, length, etc.). The program then calculated and displayed the expected deviation of the VLA from vertical. The effect of the current on the VLA in MC798 are shown in Figure 3.14. They indicate subsurface currents to be southerly at a maximum of about 90 mm/s (less than 0.2 knots).

The total displacement from bottom to the top of the VLA was 1.6 m. Therefore, the shape of the VLA at the MC798 site did not deviate very much from being vertical. There was no change in the expected depths of the individual receivers due to the current.

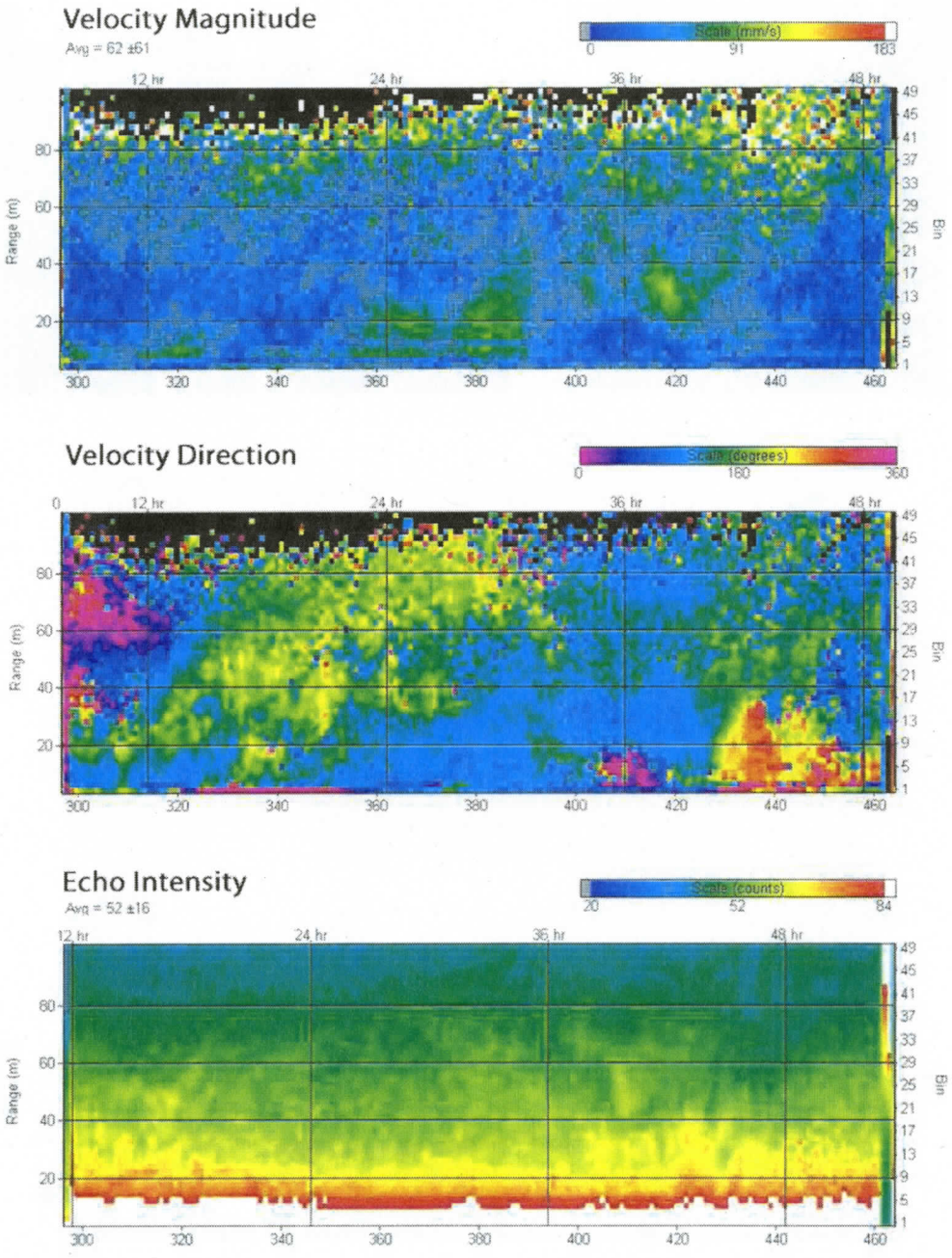

Figure 3.13: *Data from the upward looking ADCP at the base of the VLA (from Vernon Asper). This dataset was used to calculate the tilt on the vertical cable. A current velocity profile was created by integrating these data with the surface current data recorded by the ship itself (RDI Instruments). The current velocity was not strong enough to significantly change the shape of the vertical line array from vertical.*

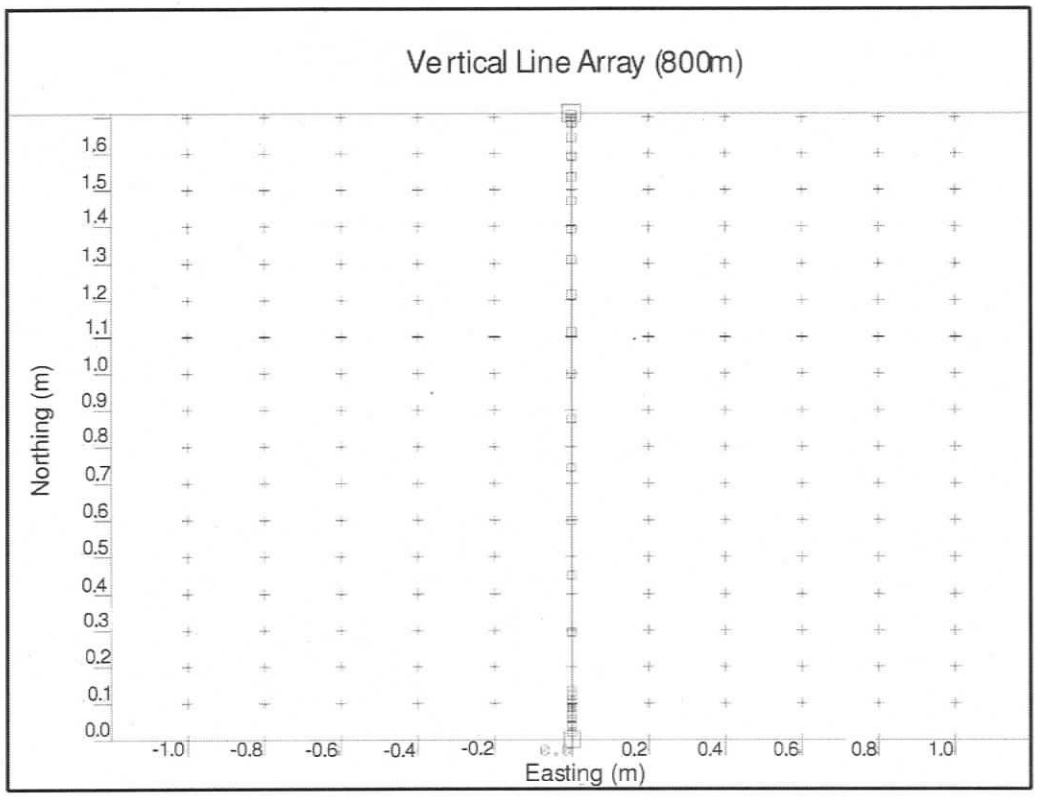

Figure 3.14: *Plan view of the displacement from the bottom to the top of the vertical cable in the direction of the current. The total displacement value was 1.6 m. This value is not significant enough over the entire cable length to cause shape change from the vertical, therefore the depths did not need to be recalculated.*

3.5.7 Acoustic Data Description and Problems

There were some major drawbacks in the data acquisition and quality that influenced the later post-processing procedures. In this section, these major limitations of the recorded data from both the 2002 and the 2003 VLA deployments will be highlighted.

- **2002 VLA Deployment**

  Channels 1 and 13 were very weak and channel 8 was noisy. These three channels were eliminated (replaced by zeros) to exclude them from further processing. Individual shot records were found to have severe timing errors due to erratic timing of the key pulse. This was corrected by static shifting each record to a calculated hyperbolic curve. First, the distance from the source to channel 2 was determined from the geometry of the measured distances from the source to the VLA site and from the sea surface to channel 2. Then the calculated distance was converted to time using the average speed of propagation in the water column, 1505 m/s, which had been determined from the CTD cast prior to the first deployment. The internal consistency of the time-corrected VLA data set was checked using a simple procedure to enhance upward-traveling energy (bottom and subbottom reflections) while reducing the amplitude of downward-traveling energy (direct waves and water surface reflections). The procedure consisted of applying negative static shifts so that the bottom reflection on each channel was aligned with the channel nearest the sea floor (channel 2).

The channels were then summed to produce one trace per shot record. This summed the upward-traveling wavelets in phase and the downward-traveling ones out of phase. Gathering together a number of summation traces along track 2 produced the image shown in Figure 3.16. The hyperbolic shape of seismic arrivals in Figure 3.16 is caused by the seismic source approaching the VLA from the left of the figure, passing over it and proceeding further away toward the right. Due to several timing errors, the navigation data for the majority of the data set were not synchronized with the shot file data and so it was not possible to recover the precise positions. Therefore, it was decided not to use these data in further processing investigations.

There was one profile, however, that was used from this dataset (since it was the first prototype VLA deployment) to calibrate the VLA data in general and to show its ability to create a profile-like image of the subbottom.

- **2003 VLA Deployment**

The VLA data collected in 2003 using both the watergun source and ship noise were quite good. The low-gain preamplifier was on channel 15 at the MC798 site and on channel 16 at the AT14 site.

There was/is a computational time problem with reformating the VLA data because these data were not recorded as profiles with the proper geometry

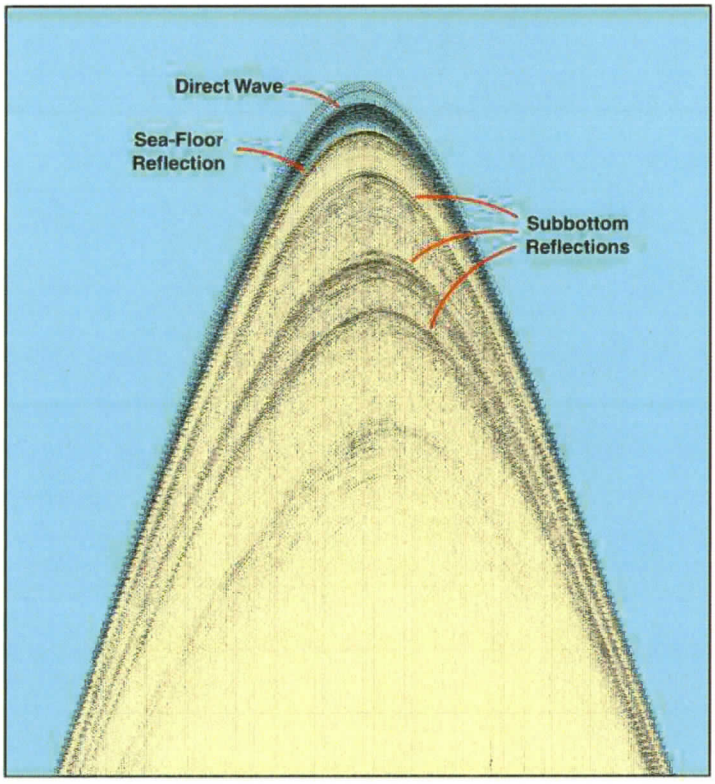

Figure 3.15: *Vertical line array single common receiver gather example (channel-2).*

written into their headers. Only individual shots with empty headers were recorded. The geometry files are separate and unorganized. Several programs had to be written to properly create the profiles with the precise geometry written into their headers. Despite all the efforts in this research to simplify this issue, it still remains a time consuming process. This problem is addressed in more details in the next chapter.

After more work on the 2003 dataset, it was realized that two channels

(channel-1 and channel-16) were dead (very weak) and channel 8 was too noisy to process. This problem instantly gave a limitation in the consideration of stacking these data properly.

Another problem surfaced when the recorded direct wave was clipped on almost every channel. Therefore, it was not possible to carry out the desired signature processing. However, on channel 15 where the gain was low, the direct wave was only partially clipped. It was used to show the performance of signature processing on the VLA data. The results of this process and the direct wave recovery procedure are discussed in greater detail in chapter 6.

Individual shot records were found to have severe timing errors due to erratic timing of the key pulse. This was corrected by static shifting each record to a calculated hyperbolic curve. Ray tracing was used to calculate this curve and a subroutine was written to automatically calculate and correct the time inaccuracies. This issue and the solution are addressed in the next chapter in more detail.

It was realized after the cruise that the array was affected by sea water leakage during the deployments. The individual hydrophones were affected differently by the cable leak, and so the system gain was different for each common receiver gather. The data in MC798 were not seriously influenced by this problem, but the AT14 dataset was badly corrupted. The results of the

corrections on this problem are shown in chapter 6.

Another issue that affected the deployment in Atwater Valley was that the ADCP data were not recorded. It was decided onboard that due to the deeper water of the site the housing of the ADCP would have been jeopardized. Therefore, there is no information about the shape of the VLA in this area. Several investigations were done in this research to model the currents using data from areas with similar setting from the northern Gulf of Mexico. It was concluded that there was a possibility that currents might have effected the data and therefore the shape of the VLA at this area. However, without knowing the current at AT14, the depths of the reflectors are uncertain. It was decided that due to the lack of knowledge of the current and the impact of the water leakage in the array that the AT14 data should not be used in the further amplitude investigation.

Chapter 4

Conventional Seismic Data Processing in MC798

This chapter describes the data processing of the two-dimensional and single-channel conventional, horizontal seismic reflection profiles described in the Chapter 3 from MC798.

4.1 Two-dimensional Seismic Data Processing

High-resolution two-dimensional and single channel data were recorded by the USGS and CMRET. Most 24-channel data were digitized at 16-bits at 4000 samples per second, the only exception being one profile of 105-105 in^3 GI Gun data recorded at 2000 samples per second. Single-channel data were digitized at faster rates (9,000-

80,000 samples per second) to improve resolution and coherence for subsequent data processing. The reflection data were affected by several noise generating effects such as continuous oscillation of the ship's heading produced by the autopilot, moderate self-generated ship noise (affected hydrophones deployed within a few tens of meters from the ship), noise due to nearby exploration seismic vessels and drilling platforms, and electrical noise on the multichannel streamer caused by corrosion in the deck connector. The quality of the reflection data was variable; it was generally considered to be sufficient for basic visual interpretation but not for processing to determine reflection coefficients.

4.1.1 Basic Data Processing

For the seismic data processing, the software of the Lookout Geophysical Company (LGC) was used. As the first step the data were reformatted from the original SEGY format to the format of LGC software.

- **Detrending**

  The next step was detrending. Often low-cut filtering can be avoided entirely using the process of detrending. The trend of a seismic trace is a slowly varying voltage produced by some non-seismic process in the environment such as wave action. The seismic energy produces a more rapidly varying voltage that oscillates about the trend. If a low-cut filter was used to attenuate the trend

it would distort the low-frequency portion of the seismic spectrum and thereby degrade the results of subsequent processing. Instead of filtering, detrending models the slowly varying trend and subtracts it from the trace, thereby leaving the low-frequency portion of the seismic spectrum relatively undisturbed. A general detrending procedure that works well is: 1) average the primitive trace by convolving it with a rectangular window, and 2) subtract the differential of the average primitive from the original data trace [50]. This way of detrending is convenient because it gives good results as well as being a very fast procedure for machine time. (An example of the results of detrending on the data is shown in Figure 4.1.)

- **Signature processing**

  After detrending, the source signature was used both to deconvolve and to phase conjugate the data before the correction for spherical divergence and hi-cut filtering were applied. If the source waveform is known (as in this case), then the solution to the deconvolution problem is deterministic. The process of deterministic deconvolution was used with zero and minimum phase filters. The better result was obtained with the minimum phase filter, and therefore, it was chosen for use in the deconvolution [24]. Deterministic deconvolution divides the amplitude spectrum of the seismogram by that of the source signature, thus producing an amplitude spectrum of bandwidth broader than that of the

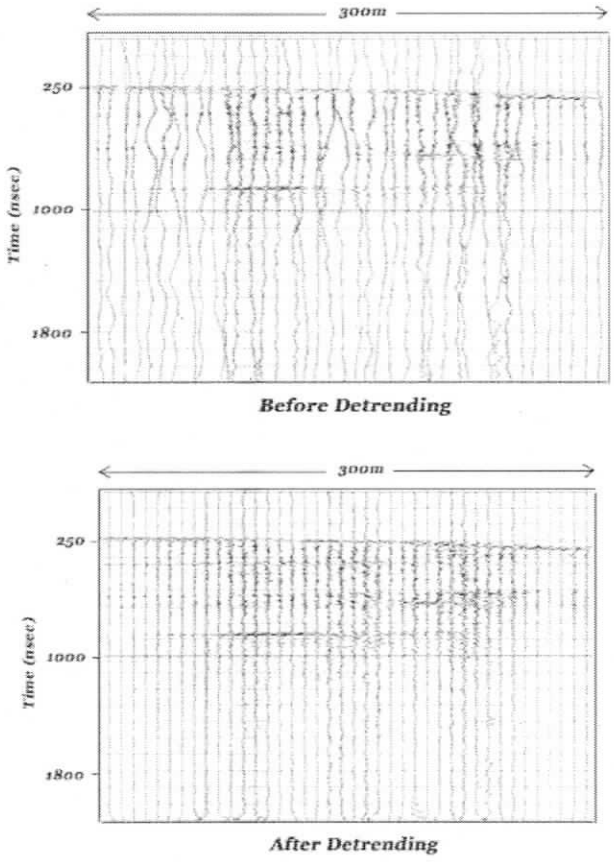

Figure 4.1: *Illustration the results of the detrending procedure on the high-resolution GI Gun data from the 1998 USGS/MMRI gas hydrate cruise in MC798. The upper panel shows the data before detrending and the lower panel represents the same profile after the detrending operation.*

seismogram. If the sampling rate is sufficiently high, resolution is proportional to bandwidth; thus, deterministic deconvolution should provide the greatest resolution compared to the phase conjugation or matched filtering. However, deconvolution is notoriously sensitive to noise, while phase conjugation is fairly

robust in the presence of noise [56].

- **Wavefront divergence correction**

  The next step was spherical divergence correction. Since seismic sources are of finite size, the wavefronts they generate expand as the energy propagates. This is called wavefront divergence and causes a reduction of the amount of energy per unit wavefront area. The reduction in signal strength must be accounted for if true reflection amplitudes are to be determined. If the signal wavelet is large compared to the size of the source and the speed of propagation is constant, the divergence is spherical and the decay is inversely proportional to the distance propagated. The correction is then a linearly increasing factor equal to reflection time multiplied by the propagation speed. It is usually assumed that the divergence is approximately spherical but it is possible to generate wavelengths smaller than the size of the source. In such a case, the radiation pattern of the source would not be spherical. Rather, its shape would be a function of frequency and the divergence correction would be vastly more complicated and it would have to be accomplished in the frequency domain. In this research, the radiation pattern of the source was assumed to be spherical and it was corrected accordingly.

- **Frequency filtering**

  The last step in the processing was frequency filtering. High-cut (low-pass) filtering was used to achieve a better interpretable image. Frequency filtering is perhaps the most common of all processes applied to seismic data and is often used with little consideration of its negative effect on resolution. The resolution, or information-carrying capacity, of a signal is measured by its entropy. Entropy is greater for signals that have smoother and more gently sloping power spectra. Filtering always reduces entropy to some extent. An example of the final processed image is given in Figure 4.2. [24].

4.2 Single-Channel SSDR Seismic Data Processing

The single-channel watergun profiles were digitized to 24 bits at 96,000 samples per second. Particular emphasis was placed on seismic imaging of the hydrate stability zone.

4.2.1 Basic Data Processing

The raw data were detrended to remove near-DC offsets. Application of source-signature-phase conjugation (a unitary operator) improved the resolution of shallow

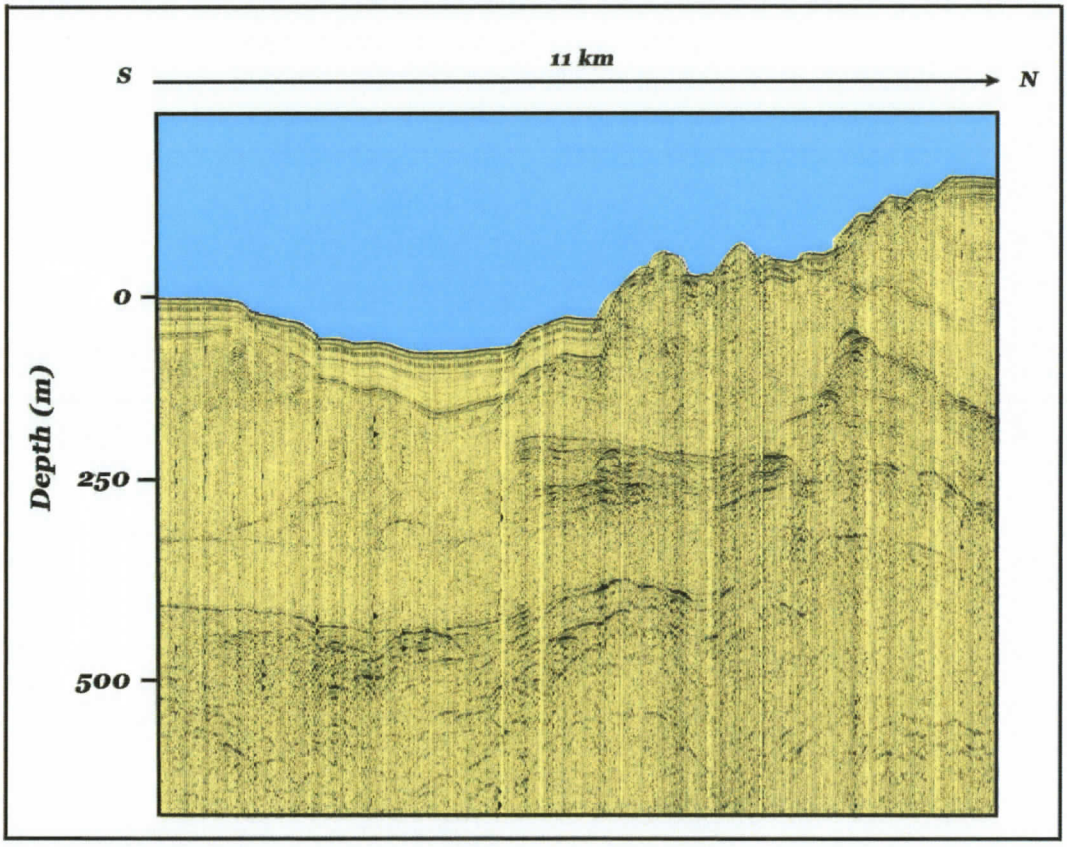

Figure 4.2: *Processed image for a single-channel 35-35 in^3 GI Gun survey line (Line 11) after all the described processing steps.*

reflections. The main processing steps for this dataset included: detrending, source-signature-phase conjugation, spherical divergence correction. The data were also migrated using the method of wave-equation migration velocity analysis. Biondi and Sava [4] introduce the method of migration velocity analysis using wave-equation techniques (WEMVA), which aims at improving the quality of migrated images. The slowness model is estimated by finding the slowness perturbation which explains the

difference between the migrated image using the reference model and an externally-defined target image [64]. Wave-equation migration velocity analysis operates in the image space, and estimates velocity by improving the quality of migrated images. This also dealt with velocity related changes observed over the entire images. Unfortunately, before the application of WEMVA technique the resolution had to be decreased (by downsampling from 96000 to 48000 samples per second) in order to carry out the migration procedure. Despite the decreased resolution, the focus of the reflectors in the migrated image was still improved. The result of the processing on the SSDR data is shown in Figure 4.3.

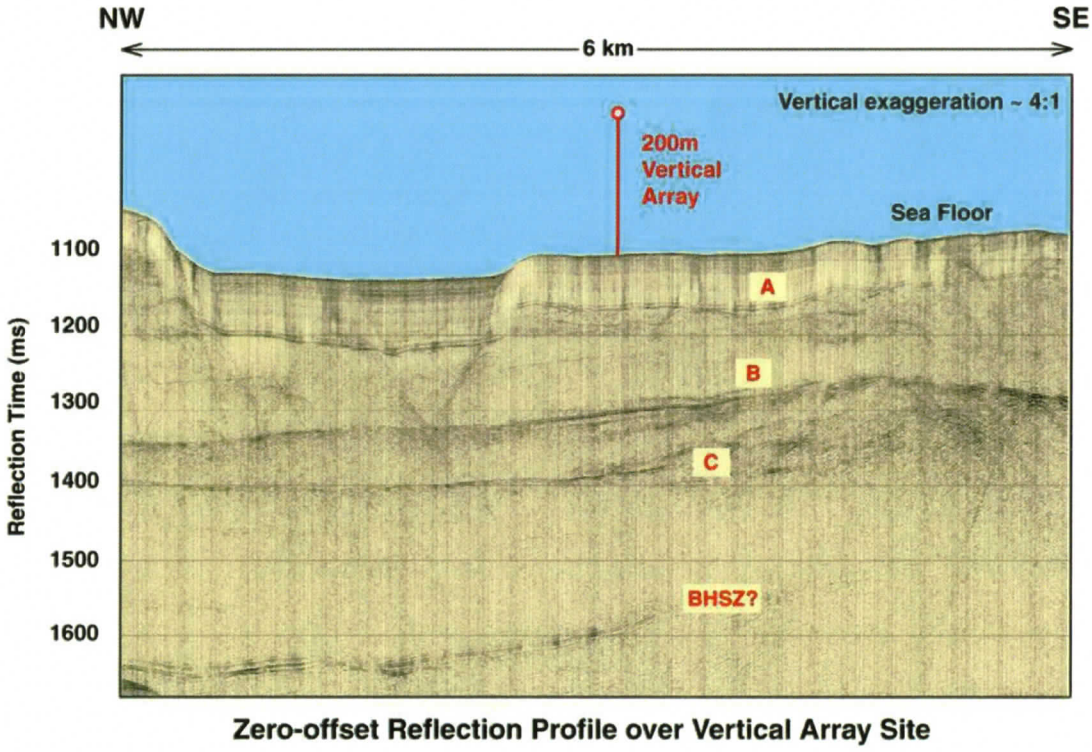

Figure 4.3: *Example from the processed SSDR dataset over the VLA site from the 2002 survey. A, B and C highlight the main reflectors.*

Chapter 5

Vertical Line Array data processing

The VLA represents a new seismic survey tool that provides advantages through its geometry in comparison to the conventional 2-D seismic technique. However, the conventional data processing procedures developed for horizontal seismic data must be modified for application to the VLA. The VLA data processing technique uses common receiver gathers (CRGs) as the basic unit of processing, and does not utilize common midpoints (CMPs) like conventional seismic processing. In fact, the CMP assumption, valid only for flat layers, is never made. For this reason and because of several other unique features related to the VLA geometry, new processing algorithms were developed and applied. This chapter describes the seismic data processing sequence that was developed specifically for the high-resolution VLA data from the 2003 deployment to improve the signal-to-noise ratio and the data quality.

5.1 Preprocessing: Reformating, Geometry Setup, Positioning, Ray Tracing, Static Correction

The data were recorded in SDI format (the special format of Speciality Devices Inc., the company that designed the VLA and recorded the data). Each shot was saved in separate files with empty headers. The geometry of each shot was recorded separately in different files. This issue represented a major computational time loss. Several computer programs had to be written to identify the particular geometry for each shot then the headers needed to be filled with the correct geometrical data of the individual shots.

A careful analysis of the acquisition geometry and the shot and receiver positions was also carried out before any further processing. Some position inaccuracies were noticed after the cruise and needed to be corrected. This step was crucial to the subsequent processing steps in order to carry out the proper migration procedure. The correct offsets were also calculated using a great circle calculation and added automatically into the headers.

The data also had some timing error during the acquisition and these errors required correction to establish the true time origin for all traces. Figure 5.1 shows the raw data with the time inaccuracies caused by the timing error.

To solve this problem, a computer program was written, using the method of ray

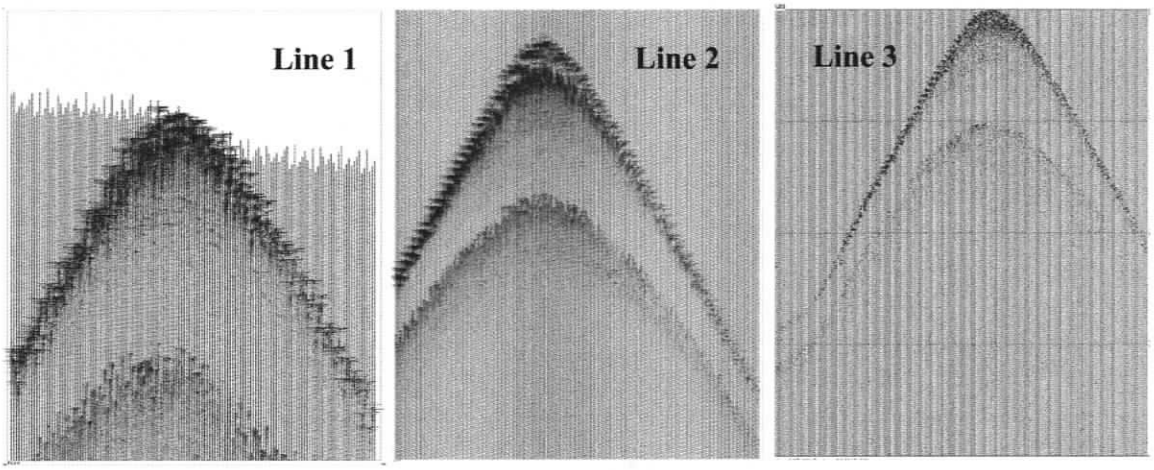

Figure 5.1: *Raw common receiver gather from Line 1, 2 and 3 from the MC798 dataset with the timing inaccuracies. At this stage, the data were only reformatted and geometrically corrected.*

tracing to calculate the static shifts for this correction. The program first calculated the travel time of the direct wave. Then the original travel time of the direct wave was picked and output into text files. Afterwards the difference was calculated between the calculated travel time and the shifted travel time (Figure 5.2).

These numbers represented the correct shift values for each shot and therefore brought the data back to time 0. Finally, these values were written into text files. These files were later taken into the final reformating algorithm and were corrected for the static shifts caused by the timing errors. The results of this process are shown in Figure 5.3 and 5.4.

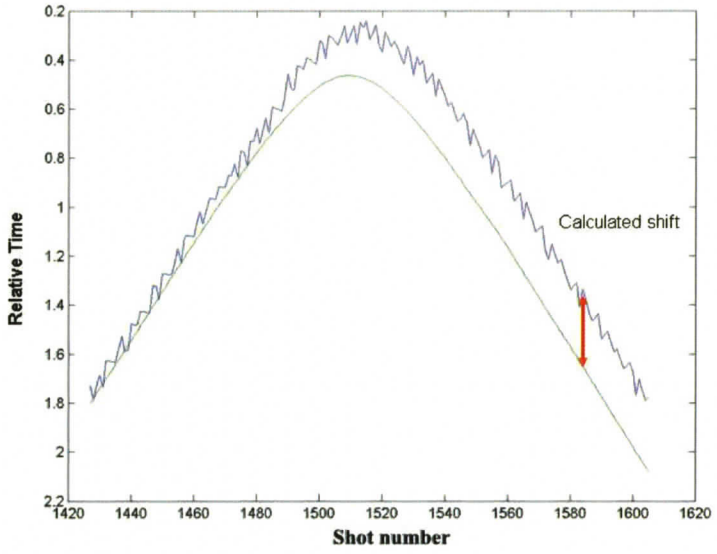

Figure 5.2: *Theoretically calculated travel times (black line) coming from ray tracing and the picked travel times from the real data (blue curve). The red arrow refers to the difference between them. These were the values that were output into the reformating program in order to correct for the timing errors.*

After the geometrical and statistical corrections, the data needed to be carefully reformatted for the processing software (Lookout Geophysical and DataTrend) first and then eventually to the industry standard SEG-Y format. The shots needed to be integrated into profiles. Shot gathers were made as the first step but they needed to be formed to common receiver gathers (CRG) to achieve the desired processing results in the later steps. In this process, programs were developed that made the reformatting an easier procedure. Several programs were written through the time of this research project to reformat the data and they were frequently revisited as an attempt to automate the process further.

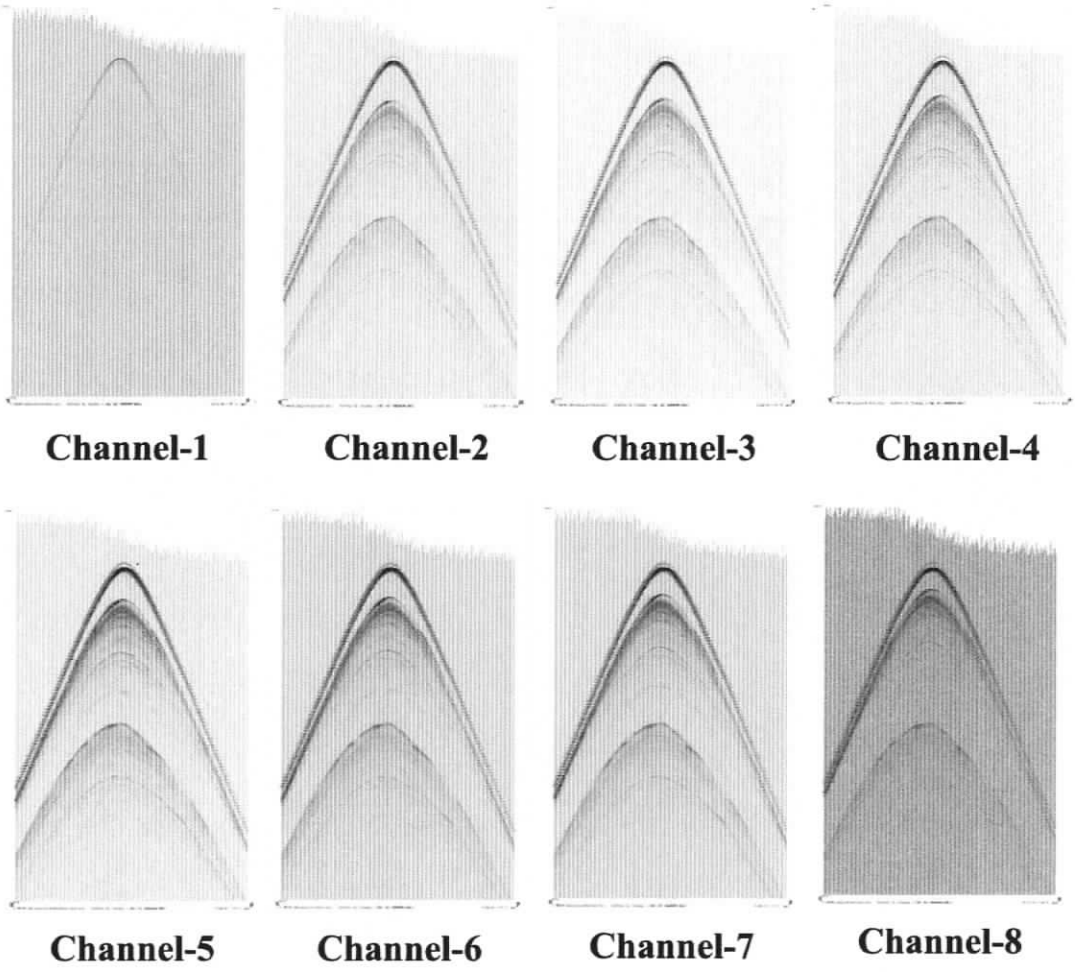

Figure 5.3: *Results of the static shift correction and a time corrected CRG from MC798 dataset. The individual common receiver gathers are shown from channel 1 to 8. Notice that channel 1 is weak and 8 is noisy.*

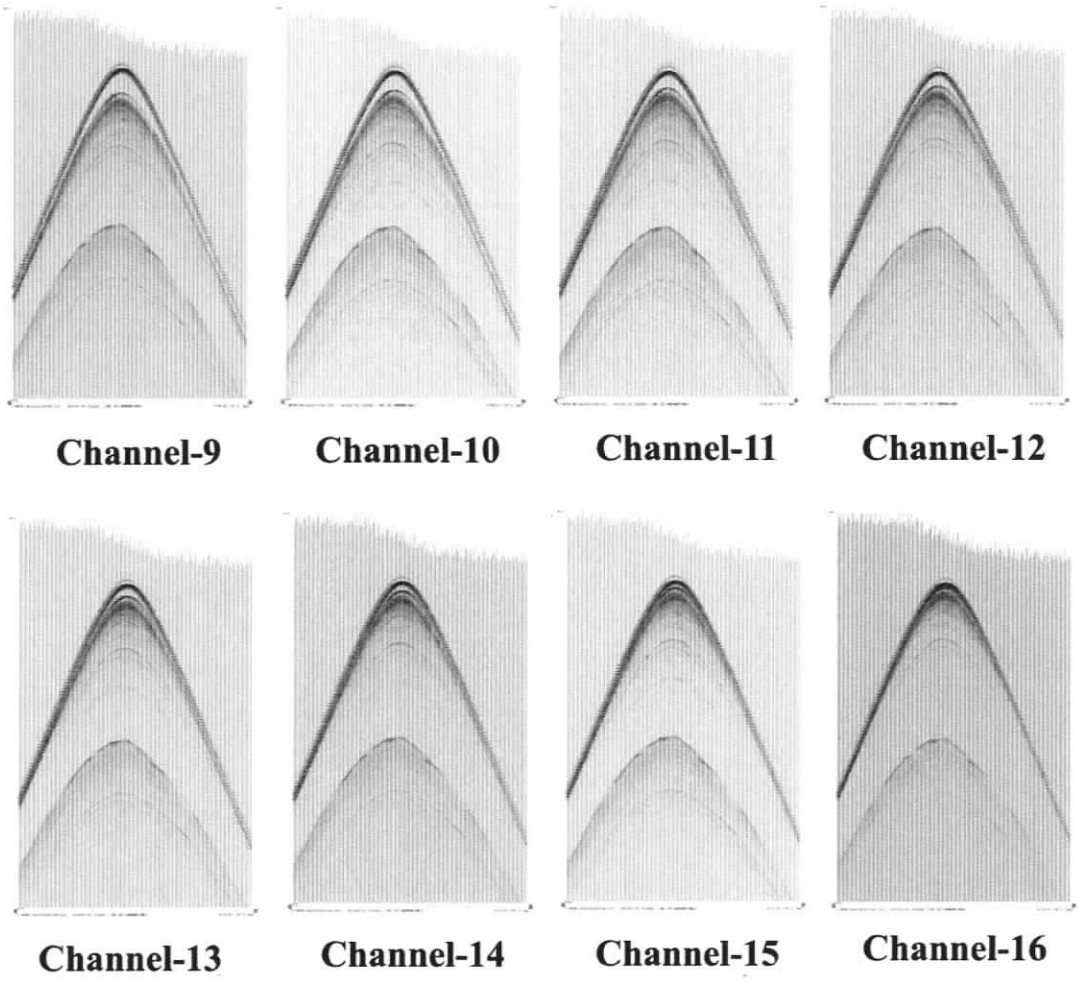

Figure 5.4: *Results of the static shift correction and a time corrected CRG from MC798 dataset. The individual common receiver gathers are shown from channel 9 to 16.*

5.2 Detrending, Wavelet Deconvolution and Spherical Divergence correction

The raw data contained a significant amount of low-frequency noise. The noise was modeled and subtracted from each trace by the method of detrending that leaves the low frequency portion of the seismic spectrum relatively undisturbed (see in details in Chapter 4).

The VLA technique uses information embedded in the direct wave that included: the true source signature, directivity, and instrument responses. This information can be used in a straightforward manner for the deterministic deconvolution. However, the direct wave in this experiment was clipped. Therefore, only the technique is presented here that was developed to the VLA data. Since this work represents the development of the technology of VLA data processing and interpretation, the deconvolution code has been written but it only could be applied at this point to the VLA profile with the clipped source signature (Figure 5.5) just to show the possibilities for the future, successful deterministic deconvolution application (Figure 5.5). The process of phase conjugation [56] was also experimented with the data and to improve the overall signal to noise ratio. The phase conjugation depends on the accurate phase in all components; therefore, the application is limited because of the direct wave clipping. The results of the trial phase conjugation process is shown in

Figure 5.6. Spherical divergence correction was also carried out on the data to correct for waveform divergence.

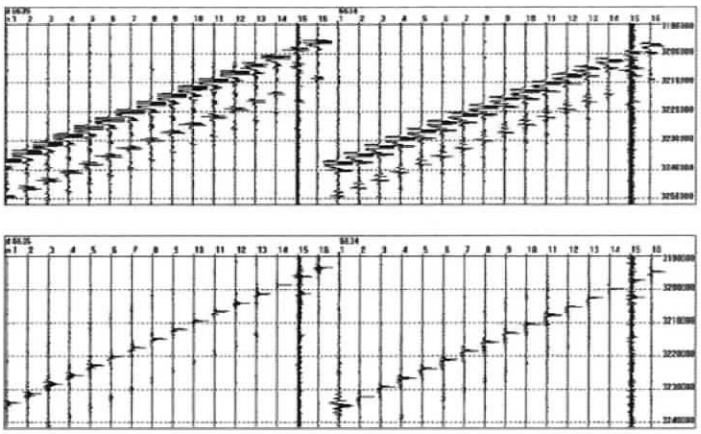

Figure 5.5: *Results of the deterministic deconvolution using the direct wave as the source signature for this processing. This image shows that even though the direct wave was partially clipped it still makes the overall image quality better. This illustration is only shown to demonstrate the performance of this process and that the algorithm is available for future VLA datasets. The top panel displays the raw signals and the bottom panel shows the deconvolved signal.*

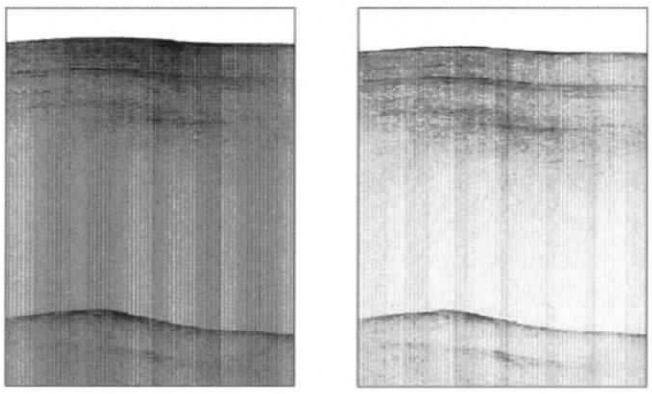

Figure 5.6: *The before (left) and after (right) images after phase conjugation of the VLA data, again for demonstrative purposes only.*

5.3 Velocity Analysis, Normal Moveout Correction and Stacking

The VLA data were required to be normal moveout (NMO) corrected. Since the common midpoint (CMP) assumption is not valid for the VLA geometry, the meaning of the stacking procedure needed to be revalidated as a part of this development study. In this section, the development of these processes will be described and the interval velocities will be presented that are achieved from this investigation. Normal moveout is the basis for determining velocities from seismic data. Computed velocities can in turn be used to correct for NMO so that reflections are aligned in the traces of a CRG before other processes. In the case of the VLA, the conventional travel time equation that is used to calculate the root-mean-square (RMS) velocities had to be revisited in order to make sure they could be applied to the VLA data. Figure 5.7 shows the source S and the receiver G at the cable O over a single interface. The reflection travel-time is expressed in terms of the offset x and velocity v as follows:

$$t = \frac{1}{v_{rms}}\sqrt{x^2 + (2h_s - h_r)^2} = \sqrt{t_0^2 - \frac{h_r t_0}{v_{rms}} + \frac{x^2 + h_r^2}{v_{rms}^2}}, \tag{5.1}$$

where $t_0 = \frac{2h_s}{v}$ is the two-way vertical travel time, h_s the depth of the reflector, and h_r is the depth of the receiver and v_{rms} is the rms velocity.

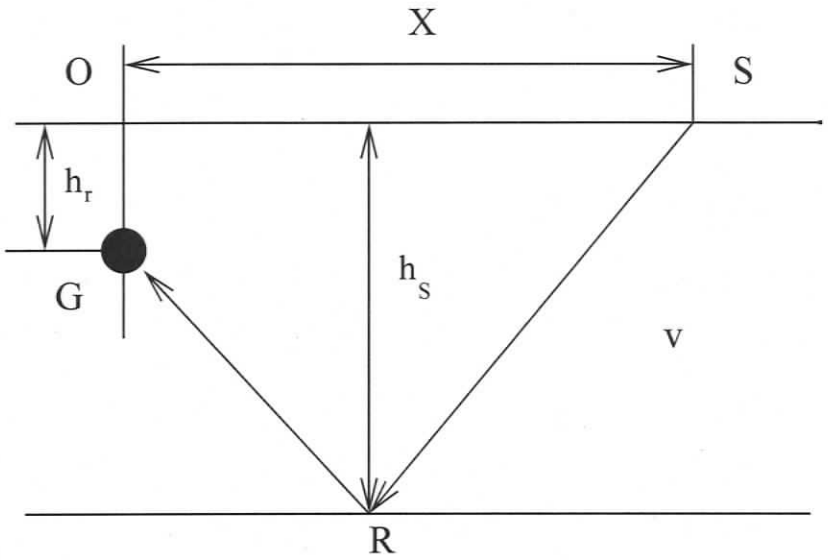

Figure 5.7: *VLA geometry. S indicates the source, R the reflection point on the sea bottom and G one of the VLA receivers, respectively. X denotes the distance between the source and the cable location, h_s is the water depth and v is the water sound speed.*

For the VLA geometry v_{rms} for the first layer can be defined as:

$$V_{1,rms} = \left(\frac{v_1^2 \frac{(\Delta t_s + \Delta t_r)}{cosi_{11}}}{\frac{(\Delta t_s + \Delta t_r)}{cosi_{11}}} \right)^{1/2} \tag{5.2}$$

where Δt_s is the vertical travel time from the source to the reflection point, Δt_r is the vertical travel time from the reflection point to the receiver and i_{11} is the reflection angle for the first interface. For the first layer v_{rms} equals v_1. A similar expression is obtained for the n-layer case. v_{rms} for the n^{th} layer can be expressed as:

$$V_{n,rms} = \left(\frac{\frac{v_1^2(\Delta t_s + \Delta t_r)}{cosi_{1n}} + \sum_{k=2}^{n} \frac{\Delta t_s v_k^2}{cosi_{kn}}}{\frac{(\Delta t_s + \Delta t_r)}{cosi_{1n}} + \sum_{k=2}^{n} \frac{\Delta t_s}{cosi_{kn}}} \right)^{1/2} \tag{5.3}$$

where $cosi_{1n}$ is the refraction angle to the first layer and $cosi_{kn}$ is the reflection able from the nth layer. These equations are used in the NMO correction for the VLA data. The NMO method applied to the VLA data provides one method to invert the velocity profile. The NMO correction was similar to the conventional method with the difference that an extra offset needed to be added to the equation because of the receiver depth. The main horizons layer 1 to layer 6 are presented in Table 5.1.

The accuracy of the velocity models on one CRG gather was evaluated. Figure 5.8 displays its velocity scans overlain by the obtained RMS velocity trend (left and middle panels) as well as the resulting NMO corrected gather (right panel). The main reflections appear to be moved out with an accurate velocity and the velocity scans display a good agreement between the RMS picks and the maximum semblance. The RMS velocities were calculated for each CRG separately. The interval velocity resulting from the displayed RMS velocity trend can be see in Figure 5.9. The accuracy of the interval velocity depends on the accuracy of the RMS velocity picks. RMS velocity picking errors mainly depend on the width of the maximum semblance at a reflector. Based on the width of the semblance a possible RMS velocity picking error of $\pm$ 15 % is introduced. The resulting RMS velocity trends are displayed in

the left panel of Figure 5.9. The solid line represents the original interval velocity trend corresponding to the picked RMS trend, while the two dashed lines represent the velocities resulting from ± 15 % picking errors. Using the Dix equation [15] these different RMS trends are converted into interval velocities which are shown in the right panel of Figure 5.9. The solid line represents the interval velocity obtained from the original RMS velocity. The relatively small errors in RMS velocity introduced by picking can therefore yield considerable uncertainties in the interval velocities.

The velocity analysis provided interval velocity profiles to achieve NMO correction separately for each line and for each receiver (Figure 5.10). The interval velocities for twelve CRGs in the array have been averaged to represent the overall interval velocity model for each line. The averaging was done with the twelve time corrected velocity profiles. After the averaging, the standard deviations were calculated for each layer and for the layer thicknesses. The calculations showed that the uncertainty in the interval velocities increased with depth. The uncertainties on the depth measurements also increased with distance. The results of the NMO correction for Line 1 are shown in Figure 5.11.

The stacking procedure needed to be evaluated in this study as well. A partial brute stack procedure was used on three receivers. Since there were several receivers that could not be used for different reasons (noisy, dead, etc.) the successful, full brute stack could not be done. The results of the partial, brute stack application can

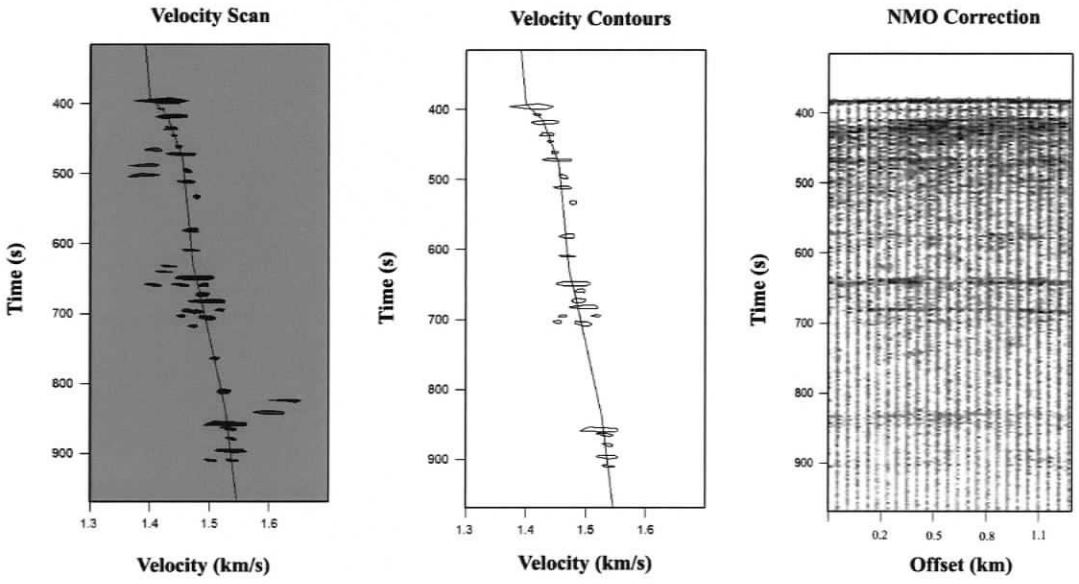

Figure 5.8: *The left panel shows the velocity scan overlain by the picked RMS velocity trend. The middle panel displays the velocity scan contours again overlain by the RMS velocity. The right panel shows the moveout corrected CRG using the displayed RMS velocities.*

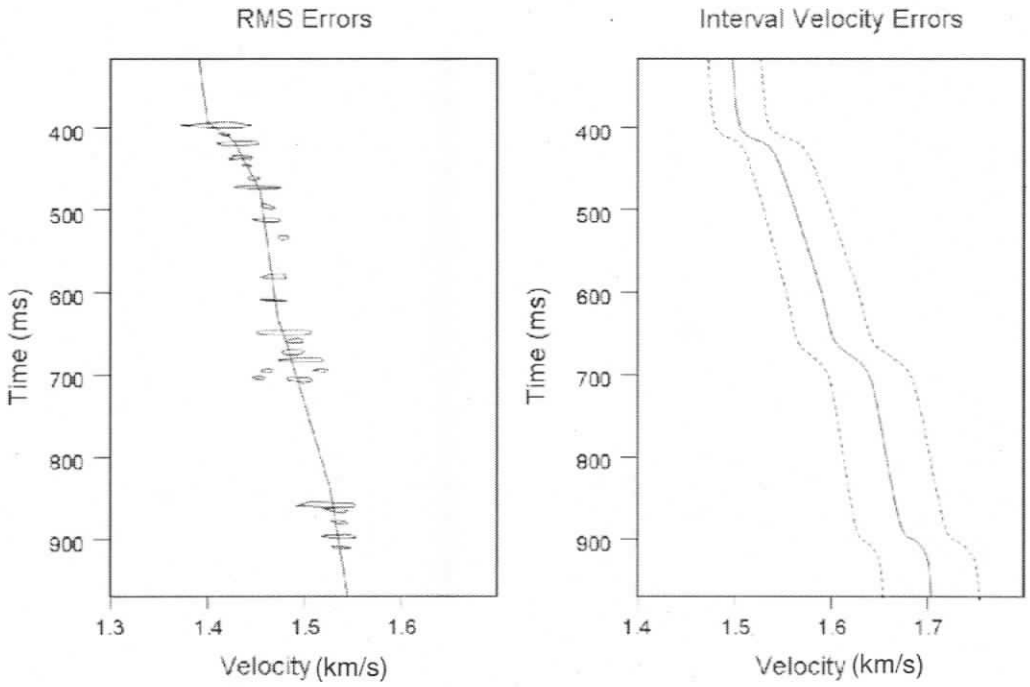

Figure 5.9: *The left panel shows the error in the RMS velocity trend. The right panel displays the interval velocities resulting from the different RMS velocity trends. The solid line represents the original velocity; the two dashed lines are the velocities with picking errors of* $\pm$ *15 % and indicates the expected error in interval velocities.*

Line 1	**Depth**	**Interval Velocity**
Layers	(m)	$v_p(m/s)$
Layer 1	$0 - 40 \pm 4$	1483 ± 10
Layer 2	$40 - 80 \pm 7$	1519 ± 20
Layer 3	$80 - 200 \pm 12$	1587 ± 35
Layer 4	$200 - 240 \pm 19$	1645 ± 40
Layer 5	$240 - 350 \pm 23$	1670 ± 50
Layer 6	$350 - \pm 35$	1700 ± 60
Line 2	**Depth**	**Interval Velocity**
Layers	(m)	$v_p(m/s)$
Layer 1	$0 - 40 \pm 5$	1510 ± 10
Layer 2	$40 - 90 \pm 8$	1535 ± 20
Layer 3	$90 - 200 \pm 14$	1580 ± 32
Layer 4	$200 - 240 \pm 20$	1645 ± 39
Layer 5	$240 - 343 \pm 25$	1660 ± 50
Layer 6	$343 - \pm 37$	1710 ± 58
Line 3	**Depth**	**Interval Velocity**
Layers	(m)	$v_p(m/s)$
Layer 1	$0 - 40 \pm 4$	1508 ± 10
Layer 2	$40 - 85 \pm 7$	1532 ± 20
Layer 3	$85 - 200 \pm 13$	1615 ± 32
Layer 4	$200 - 240 \pm 18$	1655 ± 37
Layer 5	$240 - 342 \pm 25$	1700 ± 50
Layer 6	$342 - \pm 35$	1725 ± 60

Table 5.1: Depths below the sea-floor and velocities from the NMO correction with the errors for VLA Line 1, Line 2 and Line 3.

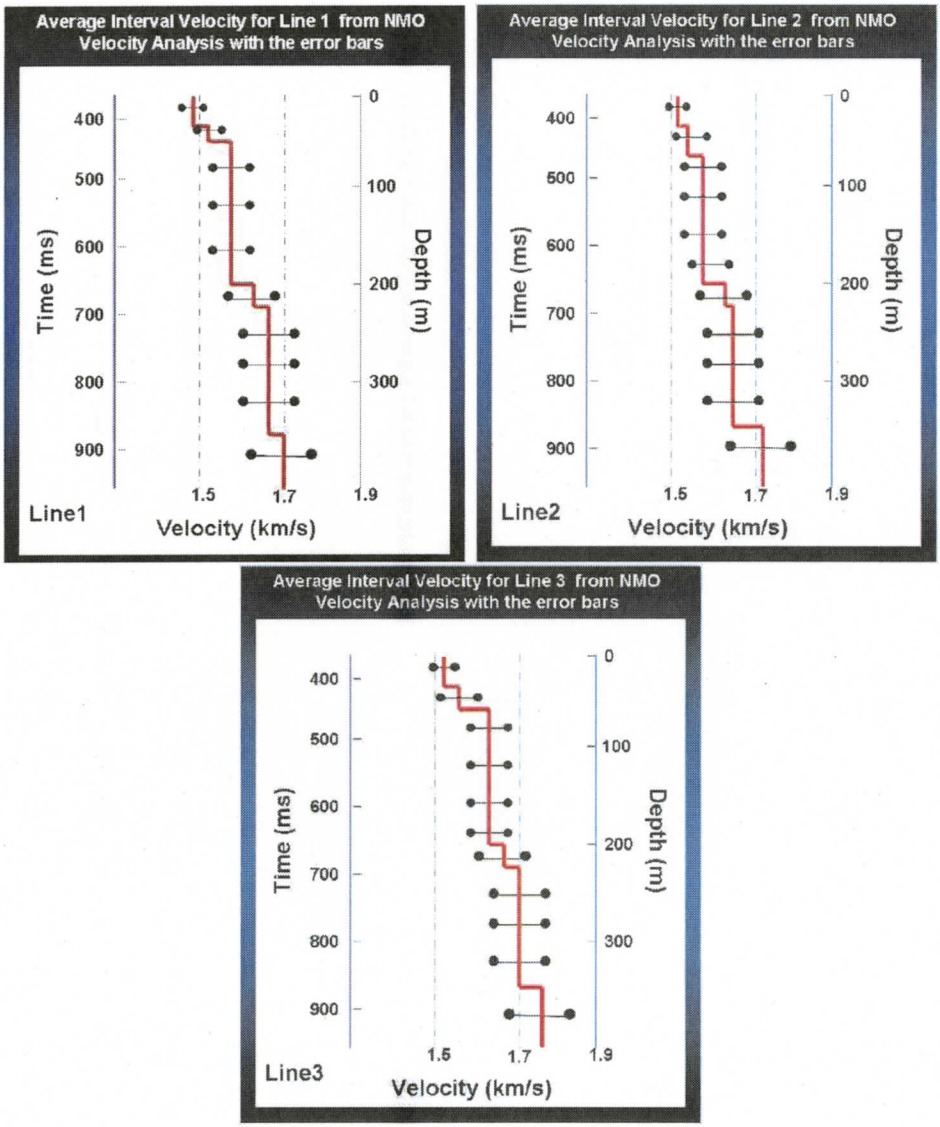

Figure 5.10: *Average NMO velocities with the standard deviations for Line 1, Line 2 and Line 3.*

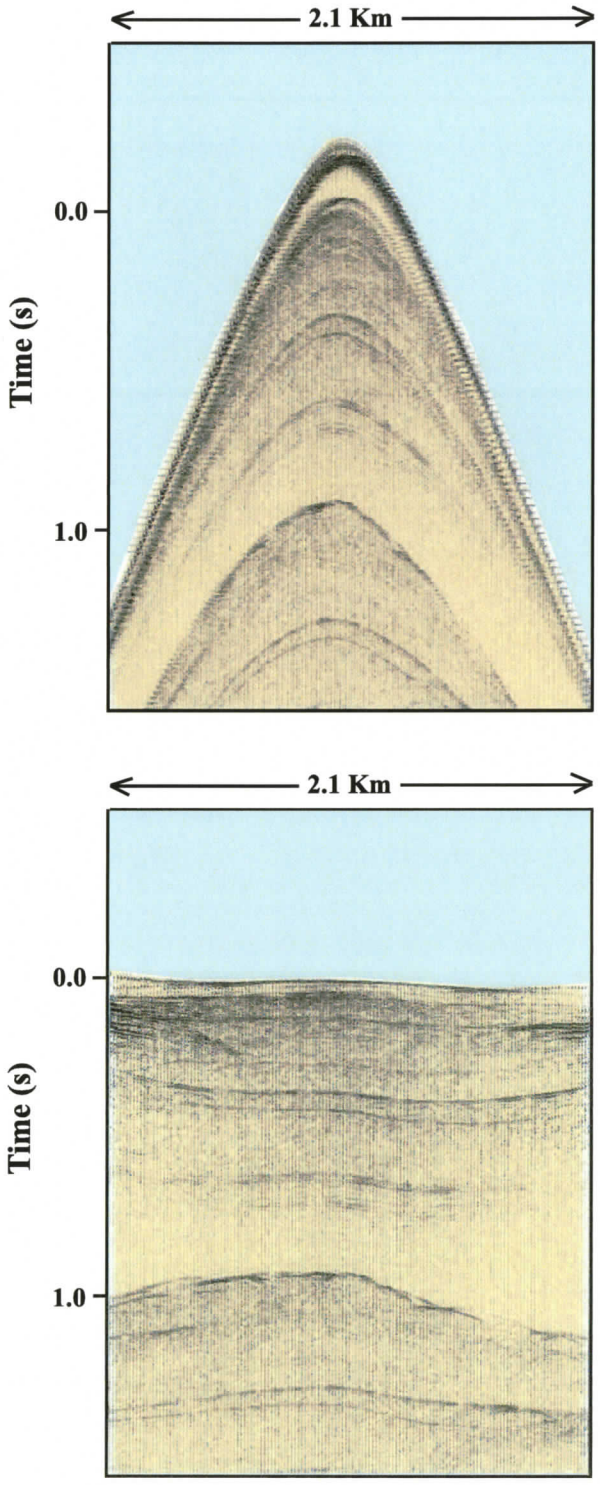

Figure 5.11: *NMO correction on VLA data. The upper image shows one CRG (channel-6 on Line 1) before normal moveout (NMO) correction, the lower image represents the normal moveout corrected profile.*

be seen in Figure 5.12. Notice that the profile looks blurry. The explanation for this can be that the different common receiver gathers were representing slightly different parts of the sea-bottom. Therefore, not one sea-floor image was stacked together but three. Even though this process did not help the quality of the overall image, it preserved the main features and it was also a quality control tool on the NMO process.

Normally stacking would be useful for improving the signal-to-noise ratio in the image. However, the VLA stacking is fundamentally limited by the array geometry since the the traces can not be arranged in CMP groups.

5.4 2-D Travel-time Calculations

Pre-stack depth migration is a processing technique used to image models with complex geologic structures that cause rapid lateral variation of the seismic velocity. The vertical cable method collects common receiver gathers (CRG) that should be pre-stack depth migrated to increase the signal-to-noise ratio and the overall image quality. Since the stacking procedure was fundamentally limited by the single VLA geometry, the process of post-stack migration could not be carried out meaningfully.

Assuming models with sedimentary cover with lateral inhomogeneities caused only by dipping plane interfaces between homogeneous layers, the rays are straight segments, but the reflections do not follow hyperbolic trajectories. The travel-time

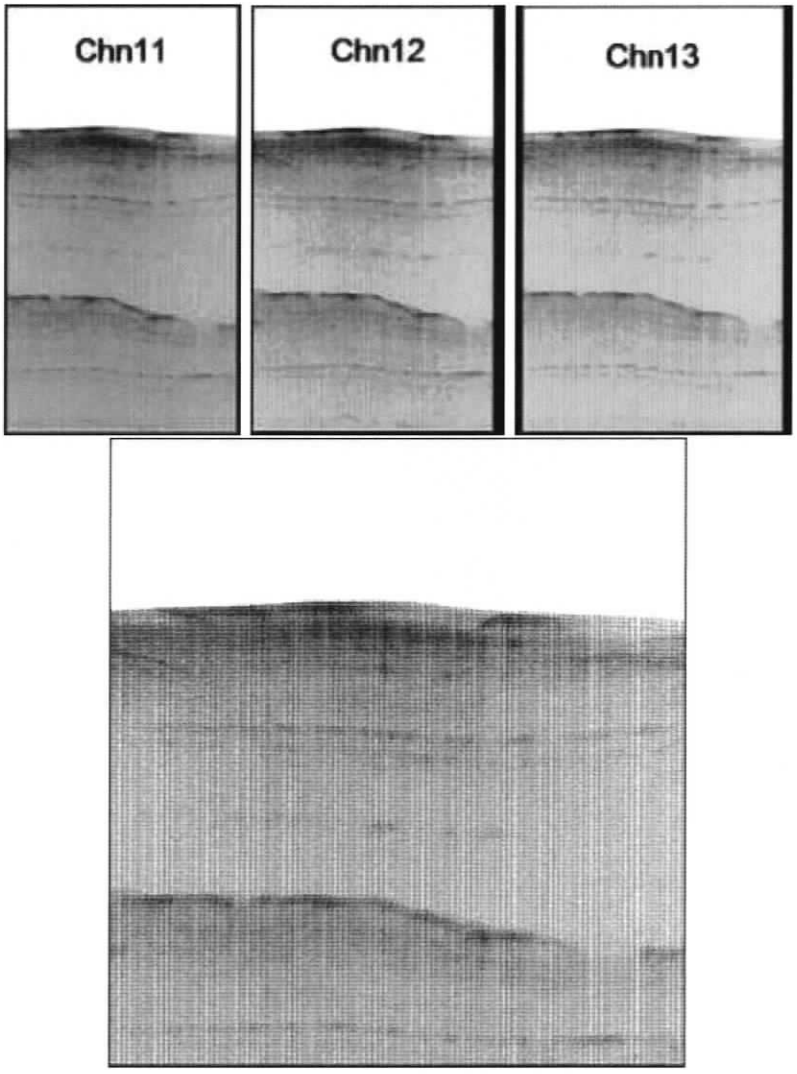

Figure 5.12: *The lower panel represents the brute stacked image from MC798 using three common receiver gathers (above) on Line 1. Notice the diffraction on the left side of the image and the role of stacking in preserving the main features.*

equation was examined in this study for CRG to obtain reliable velocities and depths for the sedimentary part of these types of models. Travel-time equations have been studied extensively in the last decades. Many authors ([20], [52], [54], [21], [13], etc.)

have published different travel-time equations and their proofs. However, most of the equation were developed for refractions and for conventional geometries. Johnson [38] presented a generic equation for travel-time with thickness and ray angles with reference to the vertical.

This study will focus on 2-D common receiver gather geometry to calculate the 2-D travel-time equation for dipping interfaces.

An analytic proof for the 2-D travel-time equation is presented that is generic for n layers. The offset is handled as a function of slowness [31]. The travel-time equation also describes trajectories in the $\tau - p$ domain. In this domain it is possible to estimate the slowness at the source and at the receiver location using 2-D or 3-D trajectories. The model for n dipping layers is shown in Figure 5.13.

For the models with n dipping layers a ray that leaves A, reflects at n^{th} interface and is observed at B, has the total travel time expressed:

$$T = \sum_{j=1}^{n} Pa_j(Xa_{j-1} - Xa_j) + \sum_{j=1}^{n} qa_j(Z_j + Xa_{j-1}\tan\omega_{j-1} - Xa_j\tan\omega_j) + \qquad (5.4)$$

$$+ \sum_{j=1}^{n} Pb_j(Xb_{j-1} - Xb_j) + \sum_{j=1}^{n} qb_j(Z_j - Xb_{j-1}\tan\omega_{j-1} + Xb_j\tan\omega_j)$$

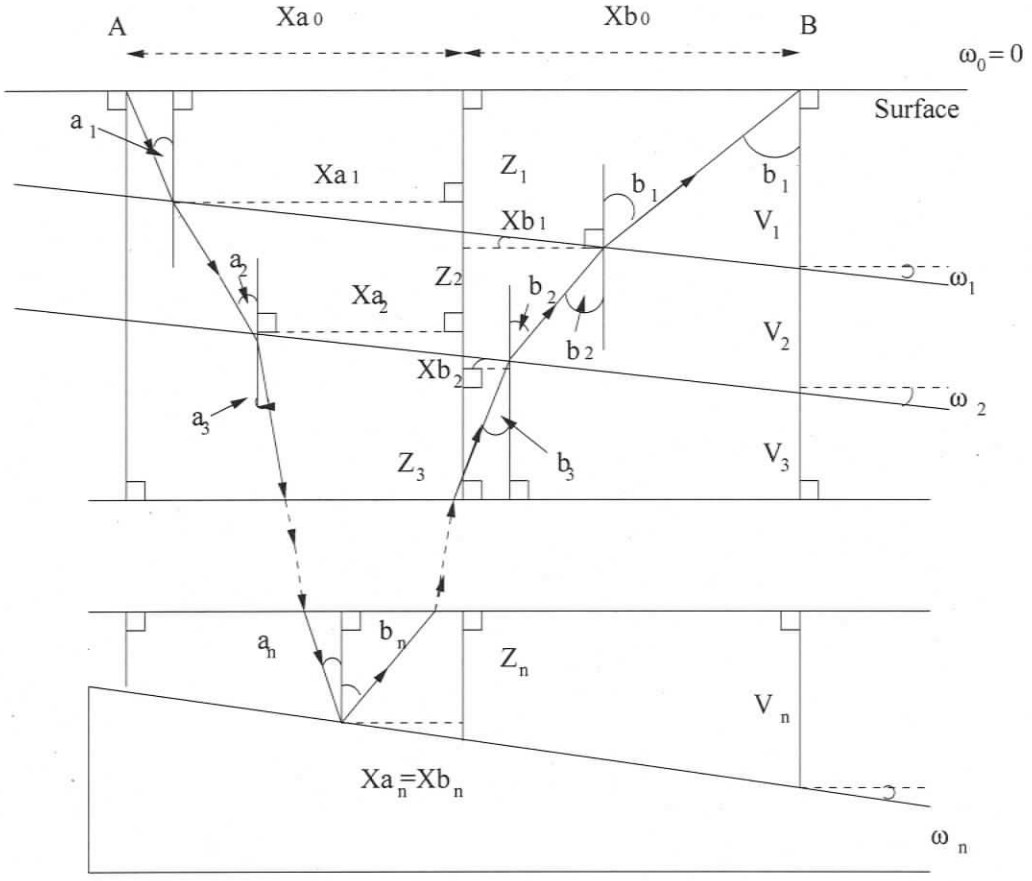

Figure 5.13: *Model with n dipping interfaces specified by Z_j, V_j and ω_j. Z_j are the depths of interfaces measured at an arbitrary position between A and B. Xa_j and Xb_j are the distances from the point where the j^{th} down-going and up-coming rays, respectively, intercept the j^{th} interface to the arbitrary position. Then, each ray segment can be decomposed into its horizontal and vertical contributions in time. The total travel-time is the sum of travel-times of each ray segment.*

Solving these equations analytically for the interval velocity of the current layers, the interval velocity of the nth layer satisfied the recursive relation.

$$V^2{}_n = \frac{\sin^2(2\theta_n)}{\{\frac{\sin(a_{n-1}+\omega_{n-1})}{V_{n-1}} + \frac{(\sin(b_{n-1}-\omega_{n-1})\cos 2\theta)}{V_{n-1}}\}^2 + \frac{\sin^2(2\theta_n)}{V^2{}_{n-1}}\sin^2(b_{n-1}+\omega_{n-1})}. \quad (5.5)$$

The dip can be computed by:

$$\omega_n = \sin^{-1}(V_n P b_n) - \theta_n. \quad (5.6)$$

The details of this calculation can be found in Appendix B.

5.5 Gazdag Pre-stack phase-shift migration and migration velocity analysis

5.5.1 Theory of shot-record migration

The principle of reciprocity says that seismic data with vertical geometry are equivalent to a single source (in place of one receiver in the cable) with receivers at the surface. Therefore, a shot-record migration scheme could be applied to these data. Shot-record migration requires back propagation of the receiver field and forward propagation of the source wave field [3]. Thus, assuming reciprocity, common-receiver gather migration shots are back propagated and receivers are forward propagated.

Claerbout [7] suggests that reflectors exist in the earth where the onset of the back propagated wave-field is time coincident with the forward propagated wave-field. Figure 5.14. illustrates this concept.

Both wave fields must be extrapolated. Downward continuation of the source field can be handled by any wave equation method ([3], [7], [23]). The receiver field is handled theoretically. Typically the travel-time is known analytically by solving the eikonal equation directly or by ray-tracing, or alternatively, by downward continuing a Dirac function with the same wave equation method which extrapolates the source field.

Ray-tracing generates multi-paths in complex areas connecting two points of in-

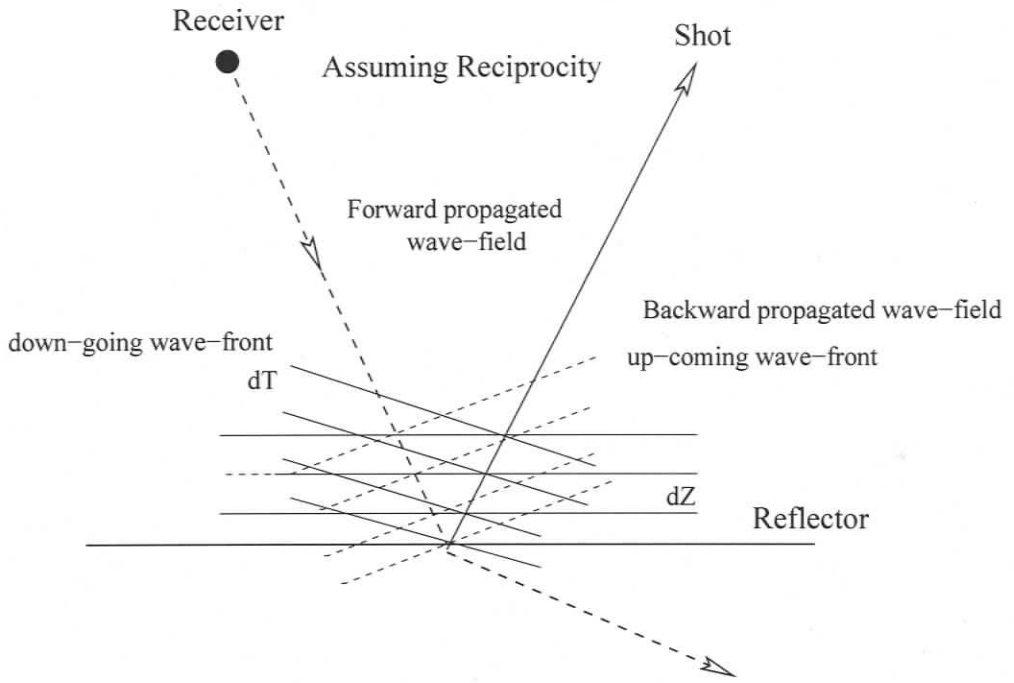

Figure 5.14: *Forward- and backward propagation wave-fields at different depths. At the depth of the reflector the fields have the same time. The fundamental principle of the reflector mapping states reflector exist where fields are time coincident.*

terest. Additionally, this method would be slow for 3-D models and does not handle shadow zones. The numerical solution of the eikonal equation is faster than ray tracing, and it is well suited for rapid computations of travel-time throughout a 3-D velocity model. However, the travel-time is obtained from the first arrival from one point to another, and does not necessarily correspond to the shortest path. The extrapolation of a Dirac function from the receiver by one of those wave equation methods is more accurate and robust than those previous method since it is derived

from the full wave-equation and not from an asymptotic solution based on high frequency assumptions.

In this research, the downward continuation of the shots is always carried out by the phase shift plus interpolation (PSPI) method by Gazdag and Saguazzero [23]. For the continuation of the Dirac function of the receivers two option were used: numerical solution of the eikonal equation which provides travel-times everywhere in the velocity model, and PSPI forward propagation. These methods are more accurate over complex geologic models since the complete solution of the wave-equation is obtained. Therefore, this type of migration was used on the real data from the surveyed area. The description of downward continuation of sources and receivers can be found in Appendix C.

5.6 Migration in practice

For migrating individual common receiver gather records, the sources are downward continued using the PSPI routine in the Claritas program. The scattered field from any surface point (x, y, z) will image coherently at time t which equals the travel-time from the fixed receiver location that can be either the receiver itself or its mirror image over the free-surface. Computing travel-time over the physical model from the receiver position by numerical solution of the eikonal equation provides time to obtain the image. The process can be summarized:

-Calculate travel time t from receiver location to all points in the subsurface by eikonal equation,

-Downward continue the source $P(t, z = 0)$. This results in the scattering field at each point in the subsurface P(t,z),

-Apply the imaging condition by cross-correlating t and P.

The travel-time inversion provided the velocities to carry out the pre-stack depth migration on the VLA data. The calculated migration velocities from the travel-time inversion is shown in Table 5.2. This process constructed a velocity structure model for the sub-surface, and was applied to obtain a velocity model separately for twelve receivers and for each line (Figure 5.15). The models for all the receivers were averaged to create an average migration velocity model for each line. The standard deviations were calculated for the migration velocity profiles and indicated increasing errors with depth.

The migration process gave another estimate of the velocity profile. The migration was carried out for each CRG for each line. An example for Line 2 on Channel-6 is shown in Figure 5.16. The figure shows the profile before and after the migration. The migration worked well for the shallow layers which were better defined. It also eliminated the diffractions that are visible in the upper left portion of the unmigrated image [25]. The migration was an expensive computational time process. Migrating

Line 1	**Depth**	**Migration Velocity**
Layers	(m)	$v_p(m/s)$
Layer 1	$0 - 40 \pm 4$	1483 ± 10
Layer 2	$40 - 80 \pm 7$	1519 ± 20
Layer 3	$80 - 200 \pm 12$	1565 ± 35
Layer 4	$200 - 240 \pm 19$	1645 ± 40
Layer 5	$240 - 350 \pm 23$	1670 ± 50
Layer 6	$350 - \pm 35$	1700 ± 60
Line 2	**Depth**	**Migration Velocity**
Layers	(m)	$v_p(m/s)$
Layer 1	$0 - 40 \pm 5$	1505 ± 10
Layer 2	$40 - 90 \pm 8$	1538 ± 20
Layer 3	$90 - 200 \pm 14$	1615 ± 30
Layer 4	$200 - 240 \pm 20$	1655 ± 40
Layer 5	$240 - 343 \pm 25$	1702 ± 50
Layer 6	$343 - \pm 37$	1730 ± 60
Line 3	**Depth**	**Migration Velocity**
Layers	(m)	$v_p(m/s)$
Layer 1	$0 - 40 \pm 4$	1500 ± 10
Layer 2	$40 - 85 \pm 7$	1535 ± 20
Layer 3	$85 - 200 \pm 13$	1621 ± 30
Layer 4	$200 - 240 \pm 18$	1665 ± 40
Layer 5	$240 - 342 \pm 25$	1715 ± 50
Layer 6	$342 - \pm 35$	1723 ± 60

Table 5.2: Depths below the sea-floor and velocities from the migration velocity analysis with the errors for VLA Line 1, Line 2 and Line 3.

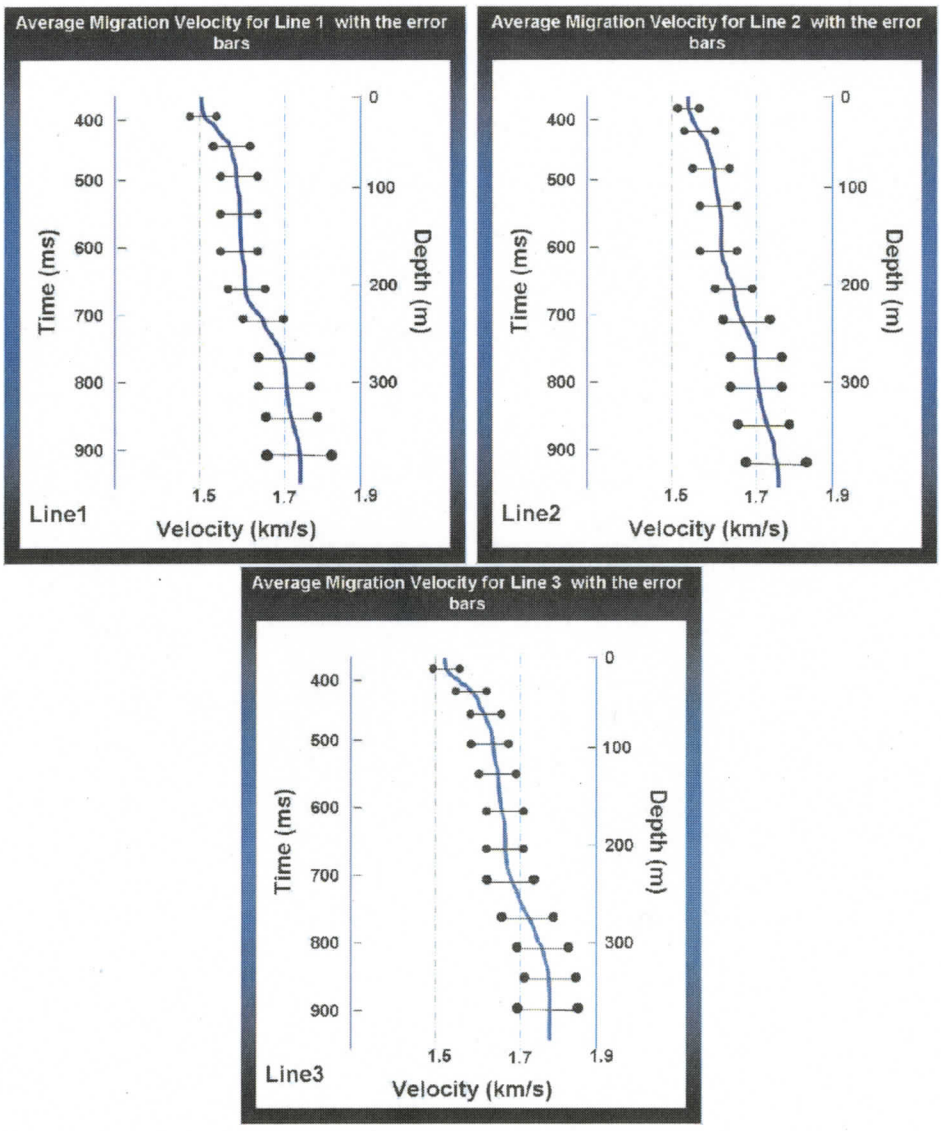

Figure 5.15: *Average migration velocities with the standard deviations for Line 1, Line 2 and Line 3.*

each individual CRG took about 8-10 hours with a standard computer.

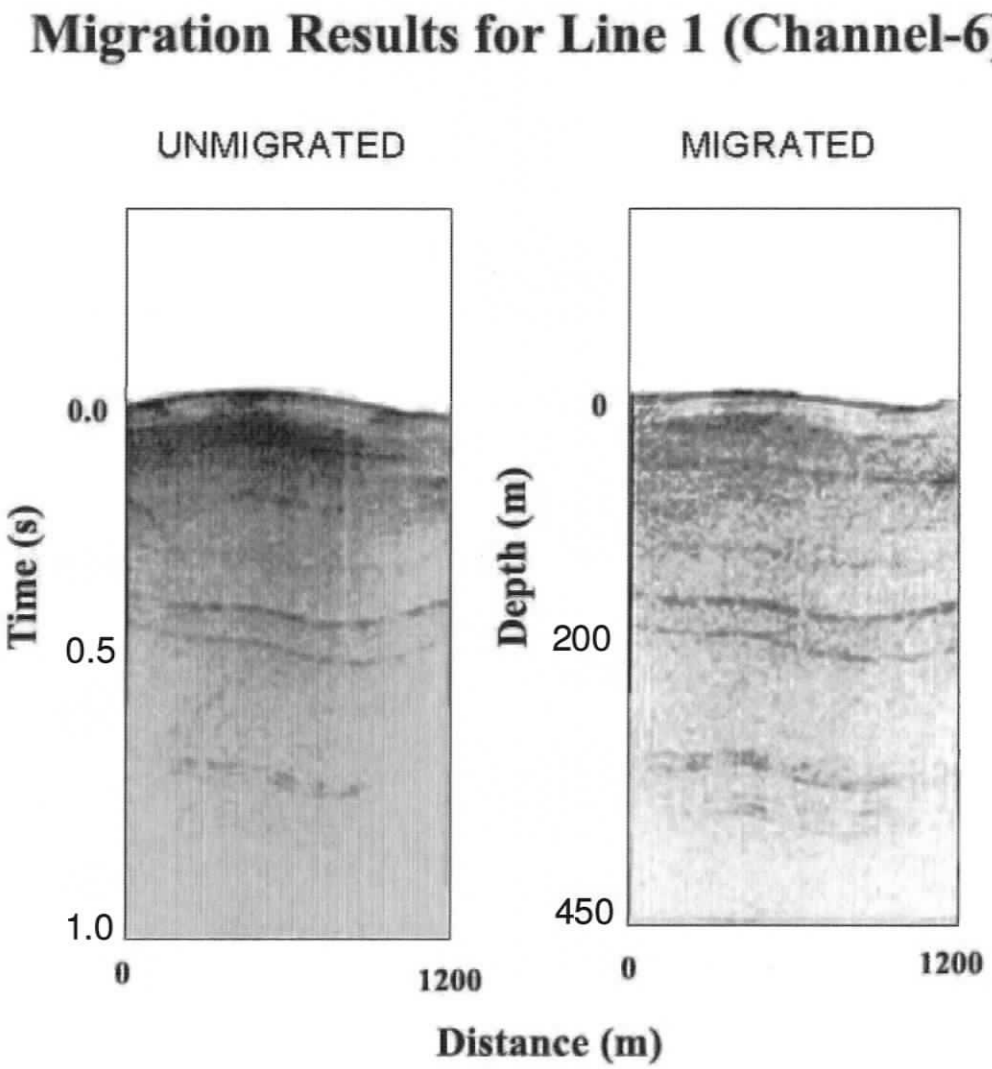

Figure 5.16: *Results of the Gazdag Phase shift migration procedure on channel-6 on Line 2 from MC798. The left panel displays the unmigrated image and the right panel shows the migrated image The migrated image has improved over the non-migrated one. The layer boundaries seems better qualified. It is also important to mention that the migration procedure only worked well for the upcoming field and it disregarded the down-going.*

5.7 Wave field separation

In the VLA technique, the up-coming and the down-going fields can be separated in the time domain if the water depth is sufficiently deep because there can be a significant time difference between the arrival times. In comparison to the VSP data processing, where the wave field separation is an important step in the processing flow since the up-coming and down-going fields interact and can only be separated in the frequency domain [33].

In the VLA data used in this work, the water depth was deep enough for the arrival time of the down-going field to be delayed. The up-coming and down-going wave field separation of the VLA data is shown in Fig. 5.17. The wave fields could carry different information about the sub-bottom because they span different angle ranges. This research worked with the up-coming field.

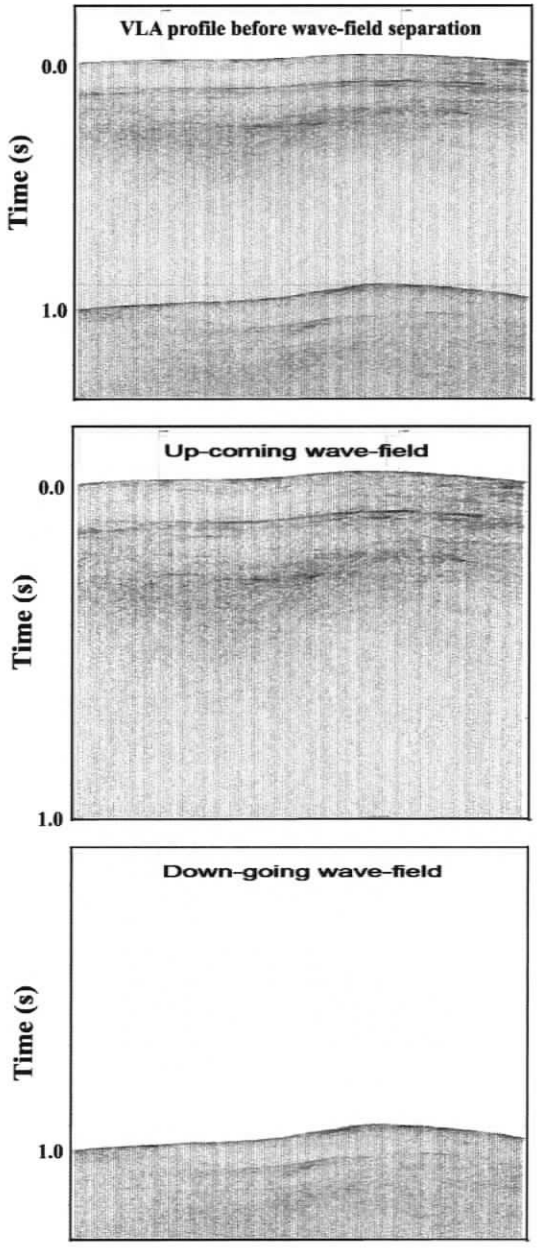

Figure 5.17: *Results of the wave field separation process on channel-7 from Line 3. The wave fields were separated in time since they did not interact with each other as they would be in VSP profiling.*

Chapter 6

Amplitude Analysis

6.1 Overview

In this chapter, the use of amplitude versus offset/angle (AVO/AVA) information extracted from the VLA data from Mississippi Canyon Block 798 is investigated for determining the characteristics of the sediment at the survey area. By observing the variation of the reflection amplitude with the incident angle it is possible to infer the acoustic properties of the media on the both sides of the interface. This method is called AVA, or, since the true angle of incidence is often known, or can be estimated using the offset between source and receiver, it is commonly referred to as AVO [6], [28]. This approach presented several challenges that were associated with the unconventional nature and the quality of the VLA data. First an examination was needed

to show that the high-resolution VLA data from MC798 have the proper range of angles to carry out the inversion. Second, the data quality presents specific difficulties. A careful analysis was done to show that if proper averaging over several hydrophones is taken into account, high-resolution VLA AVO data from MC798 provide useful information about sub-bottom sediment. The proper measure of the direct wave that is clipped on most of the channels needed to be recovered as a basic requirement for applying this type of investigation. Also, because the hydrophone sensitivities were affected by a slow water leak, the reflection amplitudes were corrupted differently on the individual receivers. Therefore, amplitude scaling was crucial, and the amplitude-preserving processing has a very important role in this research. After the proper processing, a Bayesian inversion approach is used for inverting seismic amplitude versus offset/angle (AVO/AVA) data to provide estimates and uncertainties of the viscoelastic physical parameters at an interface using the Zoeppritz equations as the forward model [67]. The Bayesian inversion is based on Gibbs' sampling to determine the properties of the posterior probability distribution (PPD), such as the posterior mean, maximum a posteriori (MAP) estimate and marginal probability distributions [19]. Finally, it is important to note that the array leakage problem limited the application of amplitude processing to data from only MC798.

6.2 General AVO theory

Reflection at an interface involves energy partition from an incident P-wave to (1) a reflected P-wave, (2) a transmitted P-wave, (3) a reflected S-wave, and (4) a transmitted S-wave as shown in Figure 6.1. The angles for incident, reflected, and transmitted rays at the boundary are related according to Snell's law,

$$p = \frac{\sin\Theta_1}{\alpha_1} = \frac{\sin\Theta_2}{\alpha_2} = \frac{\sin\Phi_1}{\beta_1} = \frac{\sin\Phi_2}{\beta_2} \tag{6.1}$$

where,

α_1 = P-wave velocity in medium 1, α_2 = P-wave velocity in medium 2,

β_1 = S-wave velocity in medium 1, β_2 = S-wave velocity in medium 2,

Θ_1 = incident P-wave angle, Θ_2 = transmitted P-wave angle,

Φ_1 = reflected S-wave angle, Φ_2 = transmitted S-wave angle,

and p is the ray parameter.

The P-wave reflection coefficient as a function of incident angle $R_{PP}(\Theta_1)$ is defined as the ratio of the amplitude of the reflected P-wave to that of the incident P-wave. Similarly, the P-wave transmission coefficient $T_{PP}(\Theta_1)$ is the ratio of the amplitude of the transmitted P-wave to that of the incident P-wave. Also, $R_{PS}(\Theta_1)$ is the ratio of the amplitudes of the reflected S-wave and incident P-waves, and $T_{PS}(\Theta_1)$ is the ratio of the transmitted S-wave and incident P-wave amplitudes.

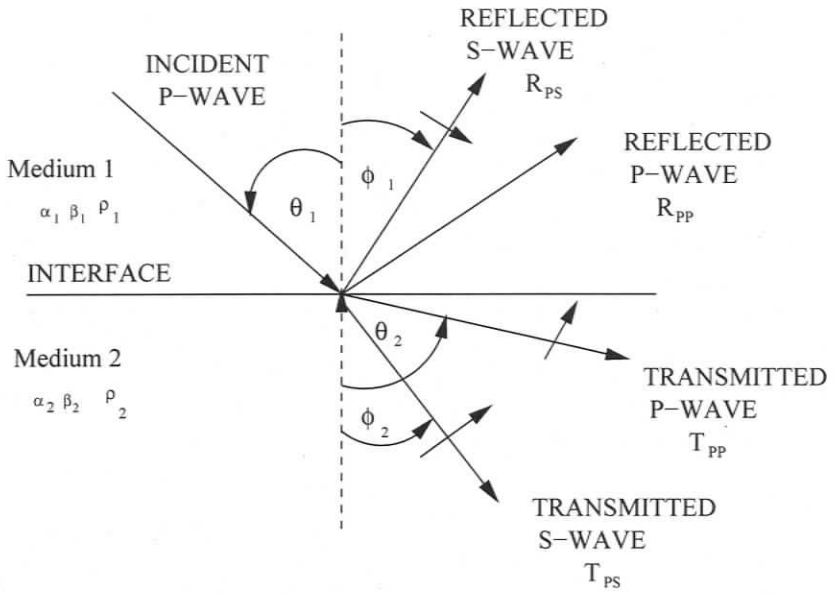

Figure 6.1: *Reflection and transmission at an interface between two infinite elastic half-spaces for an incident P-wave.*

At normal incidence, there are no converted S-waves and the P-wave reflection coefficient R_P is given by

$$R_P = \frac{I_{P2} - I_{P1}}{I_{P2} + I_{P1}} = \frac{1}{2}\frac{\Delta I_P}{I_{PA}} \approx \frac{1}{2}\ln\frac{I_{P2}}{I_{P1}} \tag{6.2}$$

where I_P is the continuous P-wave impedance profile,

I_{P2} = impedance of medium 2 = $\rho_2\alpha_2$,

ρ_2 = density of medium 2,

I_{P1} = impedance of medium 1 = $\rho_1\alpha_1$,

ρ_1 = density of medium 1,

I_{PA} = average impedance across the interface = $(I_{P2} + I_{P1})/2$, and

$\Delta I_P = I_{P2} - I_{P1}$.

The amount of energy that is reflected back from the interface is defined by

$$E_{reflected} = R \cdot E_0, \tag{6.3}$$

where E_0 is the incoming energy and R is the reflection coefficient for the specific wave component. The P-wave transmission coefficient at normal incidence T_P is given by

$$T_P = 1 + R_P \tag{6.4}$$

The variation of reflection and transmission coefficients with incident angle and thus offset is commonly known as offset-dependent reflectivity, which is the basis of AVO analysis. The Zoeppritz equations [77] describe the reflection and transmission coefficients as a function of incident angle and elastic properties of the materials in the upper and lower media (P-wave velocity, S-wave velocity and density).

The equations are expressed as four equations with four unknown reflection coefficients according to:

$$\begin{pmatrix} \cos(\Theta_{1p}) & -\sin(\Theta_{1s}) & \cos(\Theta_{2p}) & \sin(\Theta_{2s}) \\ \sin(\Theta_{1p}) & \cos(\Theta_{1s}) & -\sin(\Theta_{2p}) & \cos(\Theta_{2s}) \\ \cos(2\Theta_{1s}) & -\frac{\beta_1}{\alpha_1}\sin(1\Theta_{1s}) & -\frac{\rho_2\alpha_2}{\rho_1\alpha_1}\cos(2\Theta_{2s}) & -\frac{\rho_2\beta_2}{\rho_1\alpha_1}\sin(2\Theta_{2s}) \\ \sin(2\Theta_{1p}) & \frac{\alpha_1}{\beta_1}\cos(2\Theta_{1s}) & \frac{\rho_2\beta_2^2\alpha_1}{\rho_1\beta_1^2\alpha_2}\sin(2\Theta_{2p}) & -\frac{\rho_2\beta_2\alpha_1}{\rho_1\beta_1^2}\cos(2\Theta_{2p}) \end{pmatrix} \begin{pmatrix} A_1/A_0 \\ A_2/A_0 \\ A_3/A_0 \\ A_4/A_0 \end{pmatrix} = \begin{pmatrix} \cos(\Theta_{1p}) \\ -\sin(\Theta_{1p}) \\ -\cos(2\Theta_{1s}) \\ \sin(2\Theta_{1p}) \end{pmatrix}$$

where A_1/A_0 is the reflected P-wave amplitude normalized to the amplitude of the incoming wave A_0. Solving the full form of the Zoeppritz equations for the relevant reflection coefficients (A_1/A_0) provides the formalism for the AVO forward modeling used in this dissertation.

Since the Zoeppritz equations are highly nonlinear with respect to velocities and density, many approximations have been made in the past in order to linearize them to save computational time. However, nowadays the computer power allows researchers to solve for highly nonlinear problems without linearizing them. This study used the full form of the Zoeppritz equations in the following form:

$$R = \frac{A_1}{A_0} = \frac{\left[\left(b\frac{\cos\Theta_1}{\alpha_1} - c\frac{\cos\Theta_2}{\alpha_2}\right)F - \left(a + d\frac{\cos\Theta_1}{\alpha_1}\frac{\cos\psi_2}{\beta_2}\right)HP^2\right]}{D} \qquad (6.5)$$

where

$D = EF + GHp^2$,

$E = b\frac{\cos\Theta_1}{\alpha_1} + c\frac{\cos\Theta_2}{\alpha_2}$, $\qquad F = b\frac{\cos\psi_1}{\beta_1} + c\frac{\cos\psi_2}{\beta_2}$,

$G = a - d\frac{\cos\Theta_1}{\alpha_1}\frac{\cos\psi_2}{\beta_2}$, $\qquad H = a - d\frac{\cos\Theta_2}{\alpha_2}\frac{\cos\psi_1}{\beta_1}$,

$$a = \rho_2(1 - 2\beta_2^2 p^2) - \rho_1(1 - 2\beta_1^2 p^2), \qquad b = \rho_2(1 - 2\beta_2^2 p^2) + 2\rho_1\beta_1^2 p^2,$$

$$c = \rho_1(1 - 2\beta_1^2 p^2) + 2\rho_2\beta_2^2 p^2, \qquad d = 2(\rho_2\beta_2^2 - \rho_1\beta_1^2),$$

$$p = \frac{\alpha_1}{\sin\theta_0}.$$

The equations apply to reflection of plane-waves between two half-spaces, and do not include wavelet interferences due to layering. Furthermore, amplitudes are a measure of the reflection coefficient only when effects that cause amplitude distortions have been removed from the data. Thus, preprocessing to remove transmission loss, source and receiver directionality, spherical divergence, and so on, is essential to the successful recovery of the reflection coefficients.

6.3 True Amplitude Preserving Data Processing

The preprocessing of amplitudes is one of the most important aspects of AVO investigation. This technique can only work well if there is sufficient data quality, and the data processing is able to scale the signal amplitudes properly. The VLA dataset from MC798 presents several challenges that this study needs to address.

6.3.1 True Amplitude Recovery

Clues to the lithology and fluid content of an exploration target may be revealed by analyzing variations of seismic reflectivity with source-receiver offset or reflection

angle. Field recordings of seismic data, however, do not directly indicate target reflectivity because numerous other factors (for example, geometrical spreading, variation in shot strength or receiver coupling, directivity, transmission loss, dissipation and noise) affect seismic amplitude [55].

Data Preprocessing

The VLA data are first reformatted, shot and receiver locations and other information are placed in the trace headers, static corrections are applied using ray tracing calculations and then the data are sorted into common receiver gathers (CRGs) (see Chapter 5 for details). The number of processing steps is kept to a minimum because of impacts on amplitude distortion. Several attempts are made in this research to investigate the effects of different processing steps on the VLA data, such as filtering or normal moveout correction and it has been concluded that the raw amplitudes offer the best information content with the least distortion effects.

Direct Wave Recovery

The vertical cable technique provides information embedded in the direct wave that includes the true source signature, directivity and instrument responses. Also, the direct wave is the least influenced by the media. Unfortunately, as mentioned in detail in Chapter 4, the direct wave is clipped on almost all the hydrophones in this

experiment. The only channel for which the direct wave is unclipped is channel 16 (Figure 6.2), and so, this channel was used to estimate direct wave amplitude.

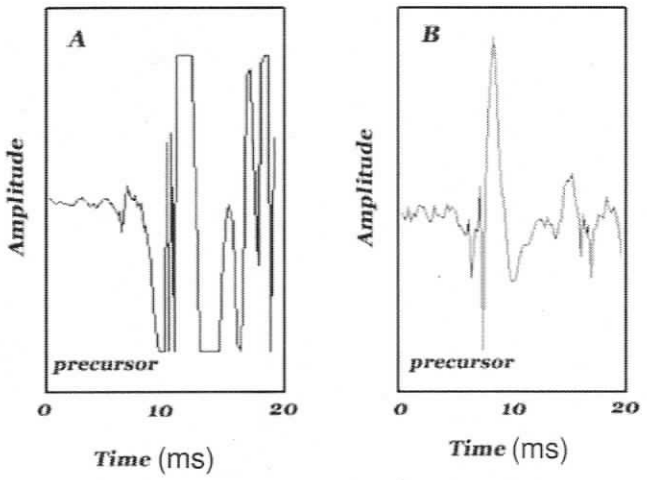

Figure 6.2: *Example of the short-range clipped direct wave (A) from channel-15 versus a long-range unclipped direct wave part (B) from channel-16 that is used in this investigation.*

This channel was purposely preset to low gain, and so did not contain any useful seismic information from the sediment. Although the direct-wave signals are recorded unclipped, their amplitudes are not consistent with those of the other channels because of the unknown sensitivity changes. An appropriate scaling has been determined using direct wave path signals for long ranges from channel-15. Careful inspection showed that these are the only unclipped direct path data from the other channels. Therefore, these direct wave signals are compared to the direct wave signals from channel-16 at the same ranges. After calculating the appropriate scaling parameter,

channel-16 data has been up-scaled for use in the AVO investigation. Figure 6.3 shows the recovered raw direct wave amplitudes. The horizontal axis of this figure indicates the track direction in terms of approaching (from extreme left to centre) and then receding (from centre to extreme right) grazing angles. The large amplitudes at high grazing angles in the centre indicate closest approach at the VLA.

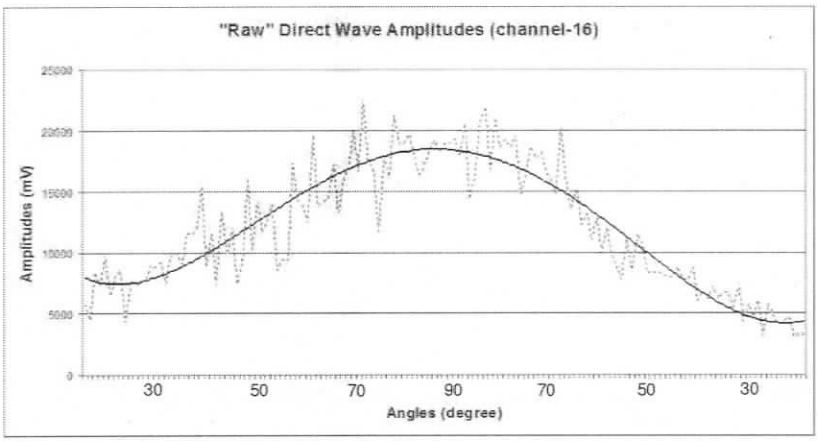

Figure 6.3: *The raw direct-wave amplitudes on channel 16 (before range and directivity correction) versus grazing angle. The dotted line represents the measured data points and the solid line is a polynomial fit (third order).*

True Amplitude picking

The amplitude picking for the direct wave and the bottom and sub-bottom horizons is done manually for all the lines. Maximum amplitudes (in mV) are picked using the software from Lookout Geophysical Company to display the data in specific time

windows previously calculated for each signal. After picking, the amplitudes are stored along with the offset and the trace number into a text file. This file was later processed using the Excel program.

True Amplitude Spherical Divergence correction

The amplitudes were corrected for the geometrical decay by multiplying by the time of the arrival. In this investigation, the data are corrected for constant velocity spherical divergence by multiplying each trace with a time-variant amplitude scale function. The correction is a linearly increasing factor equal to reflection time multiplied by the propagation speed. Figure 6.4 shows the spherical-divergence-corrected data.

Source Directivity

After the data were corrected for range effects, the sound source directivity was considered. The effect of the source directivity has serious influence on the amplitudes of the data as shown in Figure 6.4. The 80 in^3 watergun source used in this experiment showed strong directivity with a peak value around 32° relative to the incoming track geometry (Figure 6.4). To correct for this issue a directivity function was generated and was used to adjust the data for the directivity. The result of this correction for the direct wave is shown in Figure 6.5.

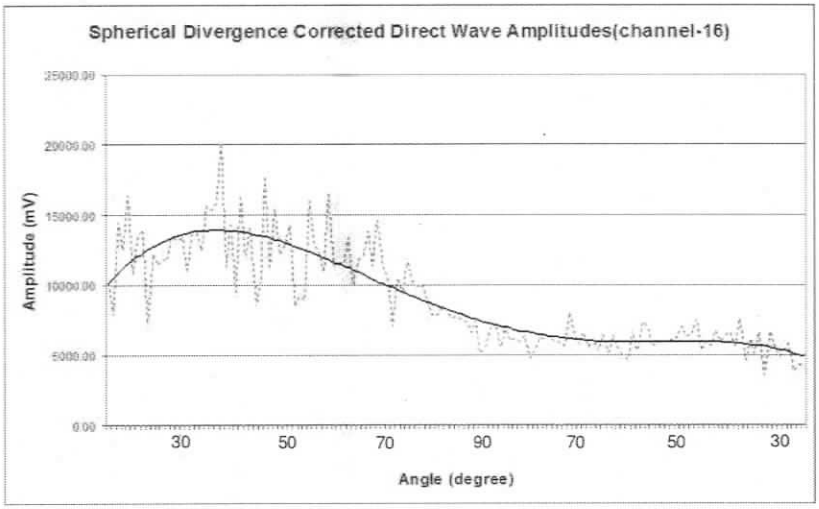

Figure 6.4: *Spherical divergence corrected direct-wave amplitudes (channel 16) versus grazing angle. The dotted curve represents the measured data points and the solid curve is a polynomial fit (third order). The horizontal axis of this figure shows the track direction in terms of approaching (from extreme left to centre) and then receding (from centre to extreme right) grazing angles.*

6.4 Sea-bottom reflection coefficient

The reflection coefficient is defined as the ratio of the reflected amplitude to the incident wave amplitude, where both amplitudes are range corrected. At normal incidence, the reflection coefficient of the sea floor can be obtained from:

$$R_b = \frac{A_b}{A_d} \tag{6.6}$$

where R_b is the reflection coefficient of the seafloor, A_b is the amplitude of the seafloor reflection and A_d is the amplitude of the direct wave. Equation 6.6 assumes that the

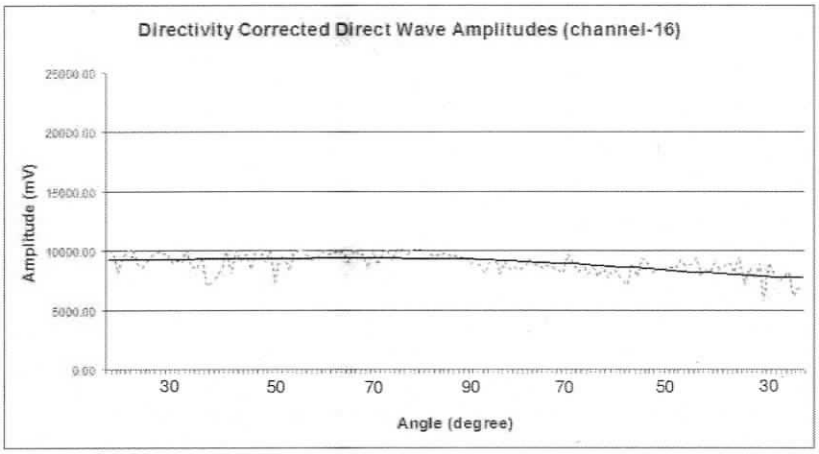

Figure 6.5: *Directivity and range corrected direct-wave (channel-16) amplitudes versus grazing angle. The dotted curve represents the measured data points and the solid curve is a polynomial fit (third order). The horizontal axis of this figure shows the track direction in terms of approaching (from extreme left to centre) and then receding (from centre to extreme right) grazing angles.*

amplitudes are corrected for range. The P-wave transmission coefficient at normal incidence T_b is given by equation 6.4. In a layered medium, the reflection coefficient of the next layer can be obtained by:

$$R_{sb} = \frac{A_{sb}}{(1 - R_b^2)A_d} \tag{6.7}$$

where R_{sb} is the reflection coefficient and A_{sb} is the scaled amplitude of the first bottom reflector and $(1 - R_b^2)$ is equal to the product of the transmission coefficient into and out of the first interface.

6.4.1 Averaging and Scaling

For the VLA geometry, the reflected signal at each hydrophone samples a different region of the sea-floor. In this analysis, the data at three adjacent hydrophones were averaged to obtain stable estimates of the AVA information. This has the effect of establishing common reflector domains on the sea-floor for the sensors, as shown in Figure 6.6.

The choice is made to use three hydrophones (channels 13, 14 and 15) from the lower portion of the array. Although the time delay is longer for hydrophones higher up the array, channels 15, 14 and 13 could be used because the delay between the direct path and bottom reflection was long enough that the two signals could be separated in time at each of the phones. Also, any uncertainty in the hydrophone position due to array motion would be amplified for the ones near the top of the array (since the array was anchored on the sea floor).

Table 6.1 shows the calculated distances and angles from the VLA to the reflection point at the sea floor for receivers 13 (50 m) and 15 (25 m). The span of offsets covers the range values used in the AVA analysis. The table shows that the size of the common receiver domains increases as the offset increases, but the largest domain size is comparable with the size of the Fresnel zone (about 55 m for the VLA geometry, assuming a frequency of 100 Hz). It is also important to note the span of offsets samples a region within about 100 m of the VLA. The distance increases for deeper

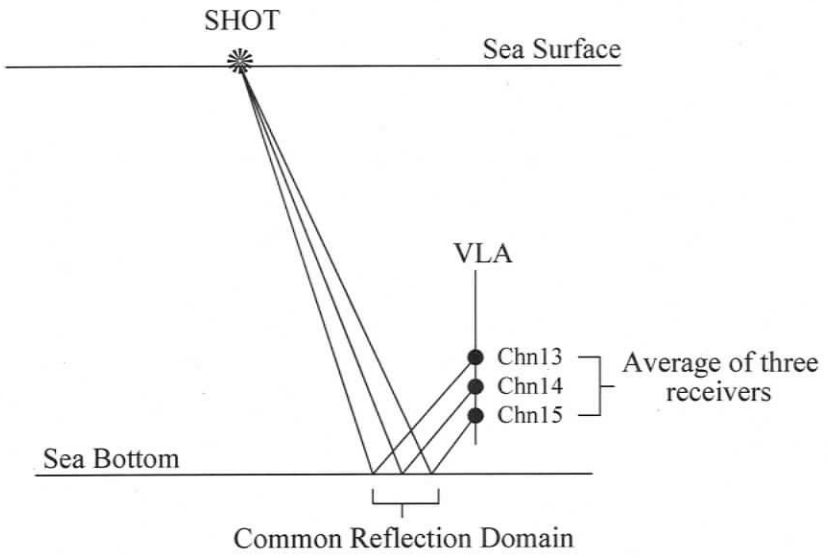

Figure 6.6: *The concept of averaging the data over three hydrophones (Channels 13, 14 and 15), and the corresponding average over their common reflection domain (close angles).*

layers, but in general the experiment provides a local estimate of the reflectivity near the VLA.

However, as mentioned above, the water leaking problem makes this procedure inaccurate without properly scaling of the various channels before averaging. Using Channel 15 as the reference channel (since it was used to scale the direct wave) Channel 13 and Channel 14 are scaled separately. The amplitudes of Channel-13 and Channel-4 are calculated and then compared to the amplitudes of Channel-15. Then a reference number is calculated between these channels and Channel-15. This

L(Offset)	$y(m)$	$x(m)$	CRD distance (m)	Θ_g
100m	25m	3.0m	2.9m	83.1^o
	50m	5.9m		83.3^o
500m	25m	15.2m	14.2m	58.8^o
	50m	29.4m		59.5^o
1000	25m	30.3m	28.5m	39.5^o
	50m	58.8m		40.4^o
2000m	25m	60.6m	57m	22.4^o
	50m	117.6m		23.0^o

Table 6.1: Calculated distances (x) and angles (Θ_g) to the reflection point from the VLA for receivers 13 (50m) and 15 (25m). y is the distance of the VLA receiver from the sea floor. The common reflection domain (CRD) is calculated as the difference of the distance between receiver 13 and 15.

reference number for Channel-13 and Channel-14 is used to up-scale the data. After the necessary calculations, the proper scaling is made and the trace amplitudes are averaged to produce the dataset used in the AVO analysis.

These corrections introduce several uncertainties into the problem and have affected the final results of the inversion (as seen later in this chapter).

6.4.2 AVA Data

In this research, three profiles (Lines 1, 2 and 3) from MC798 are used for determining seabed acoustic properties by Bayesian inversion. The amplitudes, after proper correction, scaling and averaging, are converted into reflection coefficients that are shown versus grazing angle on Line 1, Line 2 and Line 3 in Figure 6.7. The amplitudes near closest approach to and receding from the VLA are anomalously high (center

and right side in each panel of the figure). The reason for this anomalous behavior is not understood. Therefore, it has been decided to use only the approaching portion of the data set (left side of the figure) from about 27° to 70° grazing angle. The windowed section for all these lines are shown in Figure 6.8.

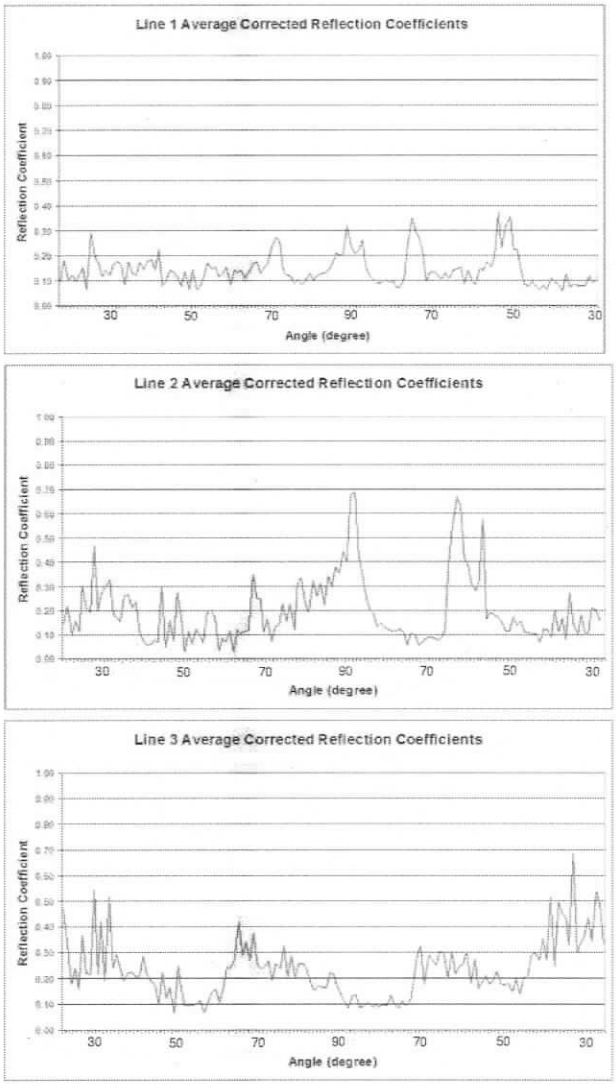

Figure 6.7: *Range and directivity corrected reflection coefficients versus grazing angle on Line 1, Line 2 and Line 3 from MC798.*

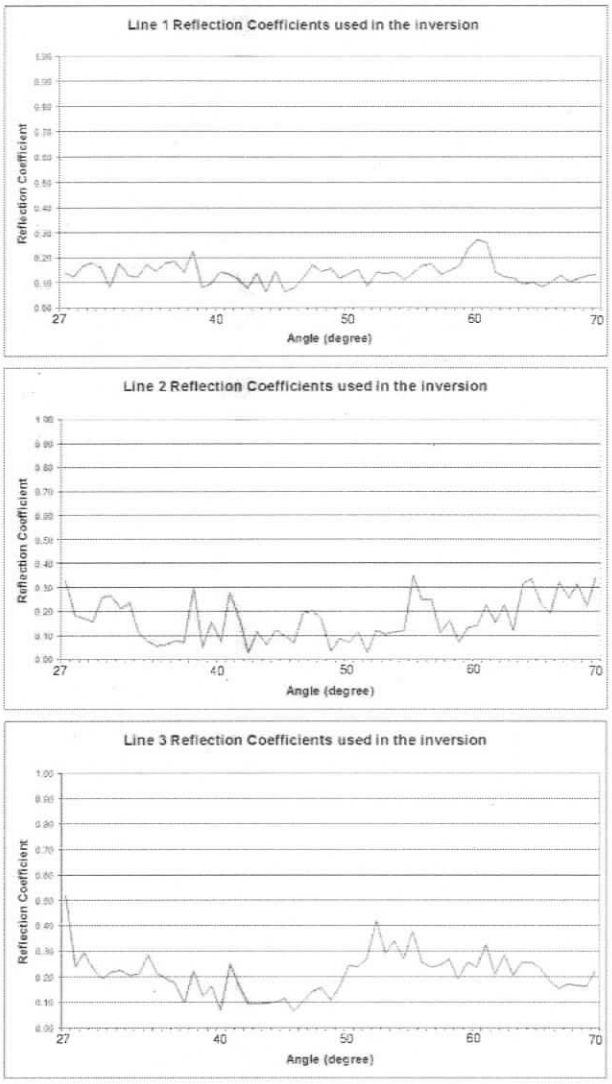

Figure 6.8: *Windowed range and directivity corrected reflection coefficients versus grazing angle on Line 1, Line 2 and Line 3 from MC798. These data have been windowed on the approaching side of the VLA between 27° and 70°.*

6.5 AVA Modeling

AVA modeling is a technique for determining sea-bed properties based on measuring the reflection coefficient of acoustic or seismic waves at an interface as a function of the angle of incidence (referred as the AVA function). The goal is to determine a model of the physical materials at the interface by inverting the measured reflectivities. The inverse problem is functionally non-linear and inherently non-unique [58]; hence, an important component involves estimating the uncertainties (probabilities) of the recovered model parameters. AVA modelling plays an active role in three areas: new technology development, quality control of data processing, and assisting data interpretation.

6.5.1 AVA Inversion Technique

Several approaches are applied to construct physical models from AVA data, including linearized methods such as generalized linear inversion [12] or fully nonlinear approaches such as genetic algorithms [66]. This research uses a Bayesian type inversion approach with Gibbs sampling for inverting reflection coefficient versus angle data to provide estimates and uncertainties of the viscoelastic model parameters at an interface [58]. The original computer code that was modified to the high-resolution VLA data to carry out this inversion was written by Dr. Stan Dosso from the University of Victoria.

Bayesian inference theory provides a fully nonlinear approach to parameter and uncertainty estimation . In the Bayesian formulation, the solution to an inverse problem is characterized by its posterior probability density (PPD). The PPD combines prior information about the model, such as parameter upper and lower bounds, with the information provided by an observed data set, quantified in terms of the likelihood function defined by the statistical distribution of the data errors [71].

Bayesian inversion treats the data and model vectors as random variables that obey Bayes' rule, which can be written as

$$P(\mathbf{m}|\mathbf{R}^{obs}) \propto L(\mathbf{R}^{obs}|\mathbf{m})P(\mathbf{m}) \tag{6.8}$$

where $\mathbf{R}^{obs}$ represents the vector of the observed reflection coefficients, $P(\mathbf{m}|\mathbf{R}^{obs})$'s the PPD and $P(\mathbf{m})$ is the prior distribution. For Gaussian errors with the likelihood $L(\mathbf{R}^{obs}|\mathbf{m}) \propto \exp[-E(\mathbf{m})]$, where $E(\mathbf{m})$ is the error function, the (normalized) PPD can be written as a Gibbs' distribution:

$$P(\mathbf{m}|\mathbf{R}^{obs}) = \frac{\exp[-E(\mathbf{m})]P(\mathbf{m})}{\int \exp[-E(\mathbf{m}')]P(\mathbf{m}')d\mathbf{m}'} \tag{6.9}$$

where the domain of integration spans the model space. From the Bayesian viewpoint, $P(\mathbf{m}|\mathbf{R}^{obs})$ represents the general solution to the inverse problem.

To interpret the PPD for multi-dimensional problems requires computation of its

properties defining parameter estimates and uncertainties, such as the maximum a posteriori (MAP) model estimate (i.e., the most probable model), the mean model estimate, the covariance matrix (evaluated about either estimates), and marginal distribution for parameter m_i, which are defined, respectively, as

$$\langle \mathbf{m} \rangle = \int \mathbf{m}' P(\mathbf{m}'|\mathbf{R}^{obs}) d\mathbf{m}', \tag{6.10}$$

$$\mathbf{C_M} = \int (\mathbf{m}' - \langle \mathbf{m} \rangle)(\mathbf{m}' - \langle \mathbf{m} \rangle)^T P(\mathbf{m}'|\mathbf{R}^{obs}) d\mathbf{m}', \tag{6.11}$$

$$P(m_i|\mathbf{R}^{obs}) = \int \delta(m_i' - m_i) P(\mathbf{m}'|\mathbf{R}^{obs}) d\mathbf{m}' \tag{6.12}$$

where δ represents the Dirac delta function and higher dimensional marginal distributions. These integrals can be written in the general form:

$$I = \int f(\mathbf{m}') P(\mathbf{m}'|\mathbf{R}^{obs}) d\mathbf{m}'. \tag{6.13}$$

In practice, much effort in Bayesian inversion is directed at efficient evaluation of integrals of the form in equation (6.14) [60]. An effective approach is given by Gibbs' sampling (GS) [67], [29]. The model is perturbed repeatedly, with perturbations

accepted if a uniform random number η on [0,1] satisfies

$$\eta \leq \exp[-\Delta E]. \tag{6.14}$$

Markov chain analysis [29] verifies that, for a large number of perturbations, the GS equilibrium distribution is equivalent to the PPD (equation(6.10)) for uniform priors. Hence, the integral I can be estimated by the mean of $f(\mathbf{m})$ as evaluated from the sample of Q models collected by GS [67]:

$$I \approx \frac{1}{Q} \sum_{i=1}^{Q} f(m_i). \tag{6.15}$$

The convergence criterion adopted here for the sampling process is to apply the GS procedure in parallel to simultaneously collect two independent samples of models. When the maximum difference between the cumulative marginal probability distributions for all parameters is suitably small (<0.05), the procedure is considered to have converged and the final sample is taken to be the union of the two independent samples [16], [17]. The credibility intervals for the solution are determined by the boundaries of the narrowest window that incorporates 95% of all samples.

Geoacoustic Model	$v_p(m/s)$	$v_S(m/s)$	$\rho(kg/m^3$
Water	1500	0.1	1030
Layer 1:	1486	100	1480
Layer 2:	1530	250	1550

Table 6.2: Geoacoustic model used in the AVA simulation for the MC798 data.

6.5.2 AVA Simulation Results

Before the inversion procedure was applied to the measured data, a simulation study was carried out with synthetic data that simulates the VLA data from the experiment. The study was designed to demonstrate the inversion performance for limited grazing angle data sets comparable to the span of angles from the experiment. There are a few 5-m piston cores available at the location of the VLA, so model parameters based on real core data could be entered into the simulation. The geoacoustic model that was used in this study can be seen in Table 6.2. The angle range of the data was between 27° and 70° and did not contain the critical angle (85°).

The standard deviation of the reflection coefficient (σ) was also calculated. The estimate of σ involves using a modeled reflection loss versus angle dataset. These geoacoustic parameters (model data) were obtained using the Adaptive Simulated Simplex Annealing (ASSA) method. This inversion uses optimization method to estimate the model parameters, then use these estimates to calculate the reflection loss. The maximum-likelihood estimate of $\hat{\sigma}$ is given by

$$\hat{\sigma}^2 = \frac{1}{N-M}|\mathbf{R}(\hat{m}) - \mathbf{R}^{obs}|^2, \tag{6.16}$$

where M is the number of model parameters, N is the number of data, and $\hat{m}$ is the maximum-likehood model estimate, determined using the ASSA optimization algorithm. $\mathbf{R}^{obs}$ represents the measured values of the reflection coefficient. The standard deviation for the first layer reflection coefficients in the synthetic case was 0.03. The results of the inversion with the synthetic data for the sea-bottom can be seen in Figure 6.9. In this inversion, the first layer (water) is constrained with very tight boundaries because there is generally sufficient information about the properties of the water from the measured sound speed profile in the experiment.

The marginal distributions for layer one are represented by histograms discretized into 150 bins and normalized so the integral over the parameter bounds (scaled to [0, 1]) is unity. The parameters (P-wave speed and density) are well determined within the assumed bounds, while S-wave speed is somewhat less well determined. The marginal distributions are smooth, and approximately symmetric for all parameters.

The inversion for the model parameters of the first sub-bottom layer used the PPDs from the first inversion for the sea-bottom as prior information. Uniform priors were passed on based on the lower and upper bounds from the marginal distributions from the first inversion. This approach represents a sequential Bayesian problem. The results of the second inversion with the simulated data can be seen in Figure

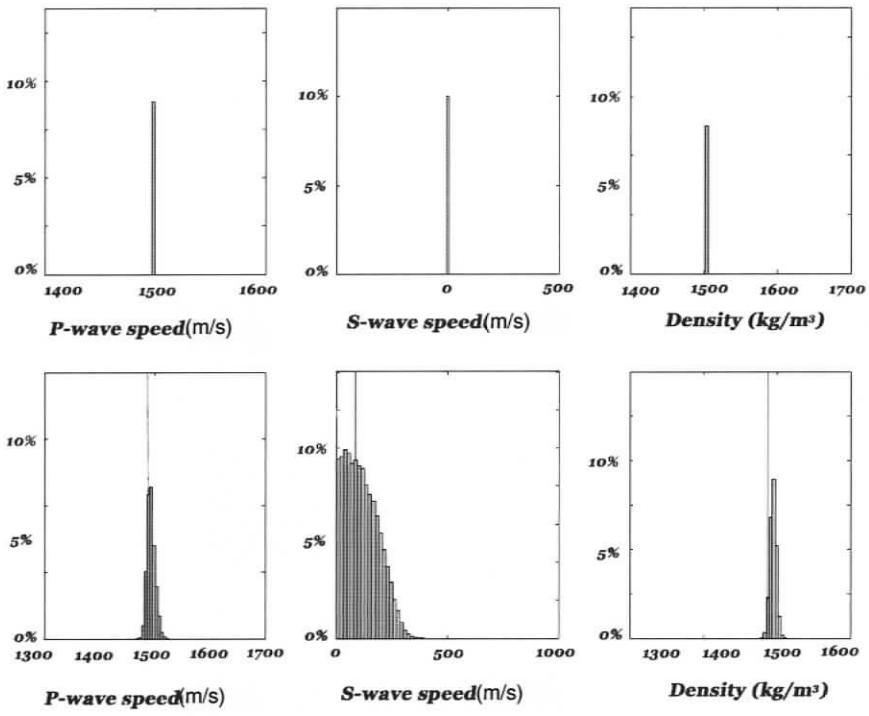

Figure 6.9: *Marginal probability distributions from the first AVA inversion with synthetic data. The first three plots represent the water layer using set values coming from the sound speed profile. The second three histograms show the marginal PPDs for the sea bottom interface. The straight line on the plots represents the true parameter value.*

6.10. The angle range was between 27° and 70° and did not contain the critical angle. The assigned standard deviation was 0.03.

In Figure 6.10, the first three marginal PPDs show the results for the sea-floor from the second inversion. The distributions are well determined and they are in good agreement with the results of the first inversion for this layer. The second three marginal PPDs show the estimates for the second layer; the distributions for

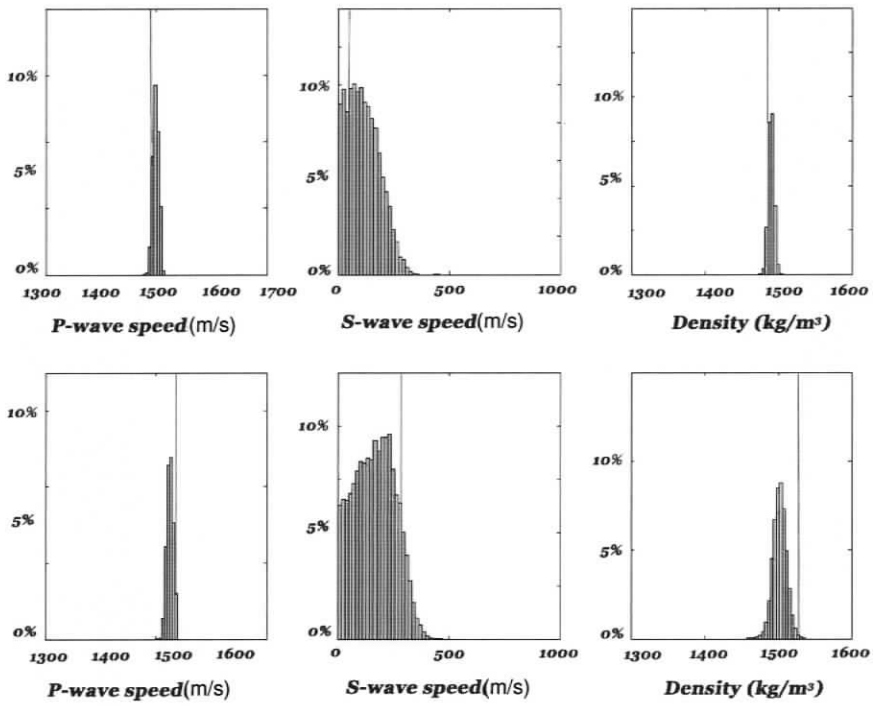

Figure 6.10: *Marginal probability distributions from the second AVA inversion with synthetic data using the marginal PPDs from the first AVA inversion as prior. The first three plots represent the first layer (sea bottom), the second three histograms show the marginal PPDs for the second layer. The straight line on the plots represents the true parameter value.*

P-wave speed and density are well determined within the bounds, but S-wave speed is not quite as well determined. The marginal distributions are symmetric and smooth for P-wave speed and density. Notice that the density marginal distribution for the second layer is wider than the distribution for the first layer. This means that this parameter not as precisely determined as it is for the first layer. For S-wave speed in the second inversion the marginal distribution is notably asymmetric with a heavier

tail toward low shear velocities. The marginal probability distributions shown in Figure 6.9 and 6.10 illustrate the uncertainties of individual parameters with the effects of all other parameters integrated out. In Figure 6.11, the marginal PPDs represent the inversion results (P-wave speed, S-wave speed, density) for the first layer from the second inversion with shaded histogram, and the white histogram represents the results for the same layer from the first inversion. It can be seen clearly that the second inversion is in a good agreement with the estimates of the first inversion.

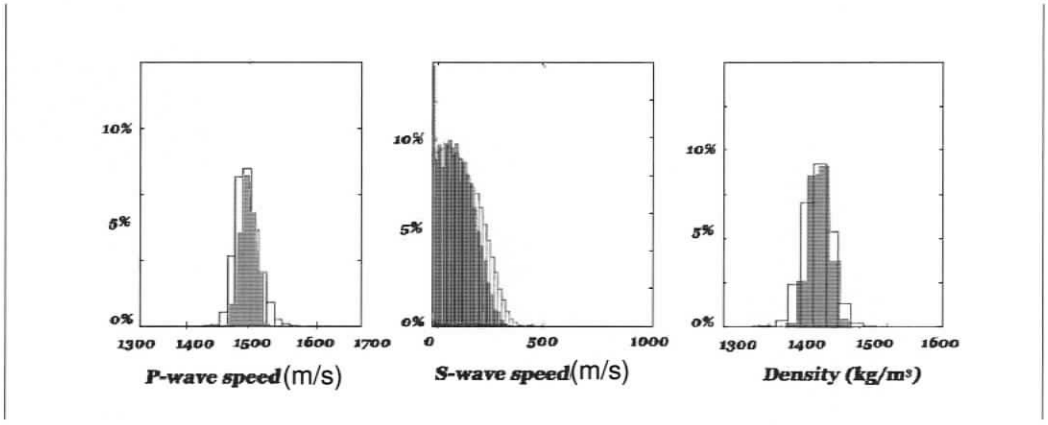

Figure 6.11: *Marginal probability distributions for the sea-floor. The shaded histograms represent the marginal PPDs for the sea-floor from the second inversion from Figure 6.10 (upper row) and the white histograms represent the inversion results for the sea-floor for the first layer from the first inversion from Figure 6.9 (lower row).*

6.5.3 AVA Inversion for the sea-bottom interface

Since the AVA inversion investigation for synthetic VLA data showed promising results, it was decided to proceed to the measured data from MC798. The properties

were well known for the upper media (water) from the measured sound speed profile. Therefore, the water velocity was fixed at 1500 m/s, according to the water velocity profile (chapter 4). The density of the water was set at 1029 kg/m^3. There is no S-wave propagation in the water so it was set as V_S=0 m/s. The bounds for the three sediment parameters are listed in Table 6.3. The angle range was between 27° and 70° and did not contain the critical angle. The calculated standard deviation was 0.05 for Line 1, 0.04 for Line 2, and 0.07 for Line 3. Figure 6.12 shows the results of the first Bayesian inversion for the properties of the sea bottom using the data from Line 3 from MC798.

The first three plots (upper row) represent the water layer using tight bounds since the values were well known. The second three histograms (lower row) show the marginal PPDs for the sea bottom interface. Parameters P-wave speed and density are well determined within the assumed bounds, while S-wave speed is not too well determined. The marginal distributions are approximately symmetric for all parameters except S-wave speed. The S-wave speed has no well determined peak and it is shifted to lower values as expected. For the inversion both the mean and the MAP (maximum a posteriori) values are given by Table 6.3.

Both the MAP and mean values for Line 1 and Line 3 for the P-wave velocity gave a value that is lower than the P-wave velocity in the water. This can have two explanations: (1) the uncertainty for the results is large and the expected value of

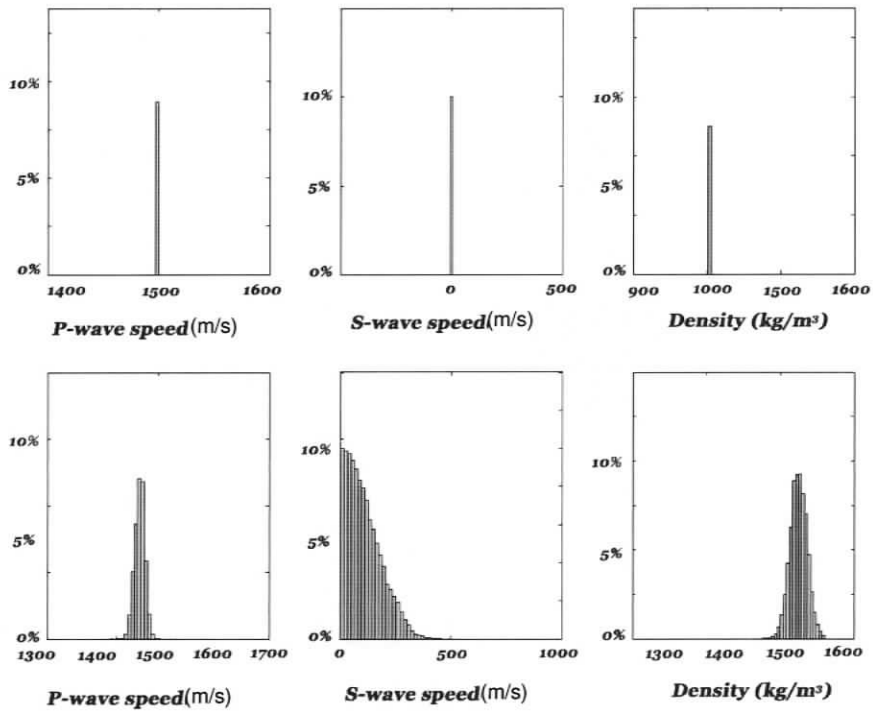

Figure 6.12: *Marginal probability distributions from the first AVA inversion using the data from Line 3 from MC798. The first three plots represent the water layer using set values coming from the sound speed profile. The second three histograms show the marginal PPDs for the sea bottom interface.*

the P-wave velocity of the near bottom sediments still falls well inside the confidence interval for the results; (2) the P-wave velocity in the sediment is lower than that in the water due to high porosity. Note that the porosity value from the core is between 55-60%. This value and the estimated density correspond well with the direct measurements conducted on samples retrieved from the piston core at the VLA site. The density value was about 1500 kg/m^3 and the estimated P-wave value was about

1492 m/s averaged over the top few meters. There are no previous measurements of the shear-wave velocity available for the site, but it is expected to be low as the sediments immediately below the seafloor are not compacted enough to provide great shear strength. Reasonable values for the shear-velocity for near bottom muddy sediment at similar sites in the Gulf of Mexico were about 70-100 m/s [32] and therefore the results of the inversion are consistent with the expected velocity range.

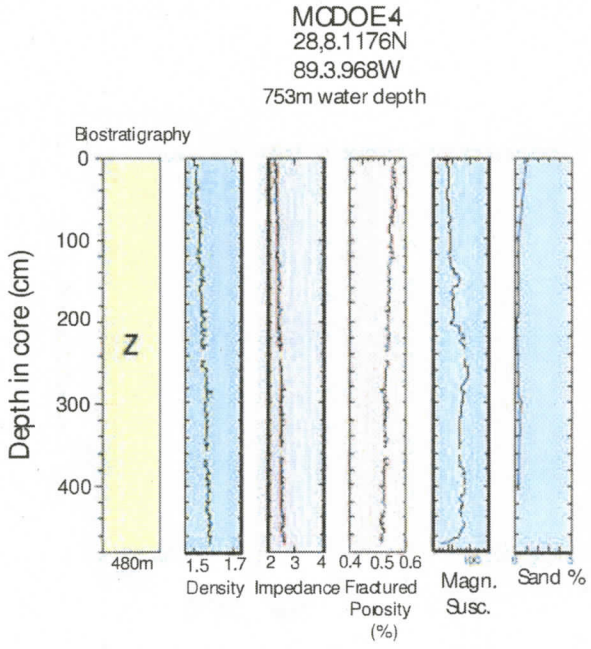

Figure 6.13: *Piston core data from the VLA location from Mississippi Canyon Block 798 by Charlotte Brunner (private communication, 2004).*

Line 1 First Inversion	$v_p(m/s)$	$v_S(m/s)$	$\rho(kg/m^3)$
Lower bound	1300	0	1300
Upper bound	1700	800	1800
Results:			
MAP	1493 ± 45	10 ± 310	1500 ± 74
Mean	1485 ± 30	68 ± 282	1530 ± 60
Line 2 First Inversion	$v_p(m/s)$	$v_S(m/s)$	$\rho(kg/m^3)$
Lower bound	1300	0	1300
Upper bound	1700	800	1800
Results:			
MAP	1517 ± 25	24 ± 280	1490 ± 90
Mean	1512 ± 28	58 ± 262	1460 ± 96
Line 3 First Inversion	$v_p(m/s)$	$v_S(m/s)$	$\rho(kg/m^3)$
Lower bound	1300	0	1300
Upper bound	1700	800	1800
Results:			
MAP	1497 ± 50	10 ± 260	1550 ± 80
Mean	1484 ± 46	30 ± 245	1530 ± 91

Table 6.3: Prior bounds and inversion estimates with standard deviation for the AVA sea bottom data for Line 1, 2 and 3 from MC798.

6.5.4 AVA Inversion for the sub-bottom interface

Similar to the approach taken in the simulation study, the upper and lower limits from the first inversion (for the sea-floor) mentioned above are used as prior information input for inverting the data for the first sub-bottom reflector. The AVA data of this reflector on Lines 1, 2 and 3 can be seen in Figure 6.14.

The angle range of the data was between 30° and 80° and did not contain the critical angle. The values for the standard deviation were 0.09 for Line 1, 0.07 for Line 2 and 0.08 for Line 3. However, when the parameters for both layers were treated as unknowns the inversion gives misleading results for the density. The densities are consistently pushed to unreasonably low values for the second layer. After several investigations were done to find the reason for this effect, it was decided that this phenomenon could be caused by errors in the scaling of the data. Since most of the scaling errors are unknown, an inversion is attempted with fixed density for the sea-floor sediments at 1500 kg/m^3. This value is based on direct measurements from the sediment cores. The results of the second inversion on Line 3 can be seen in Figure 6.15.

For the first layer the P-wave speed is well determined within the assumed bounds, while the S-wave speed displays the same trend that was seen for this parameter in the other inversions. The marginal distributions for the compressional wave velocity for the first and second layers are smooth, and approximately symmetric. The P-wave

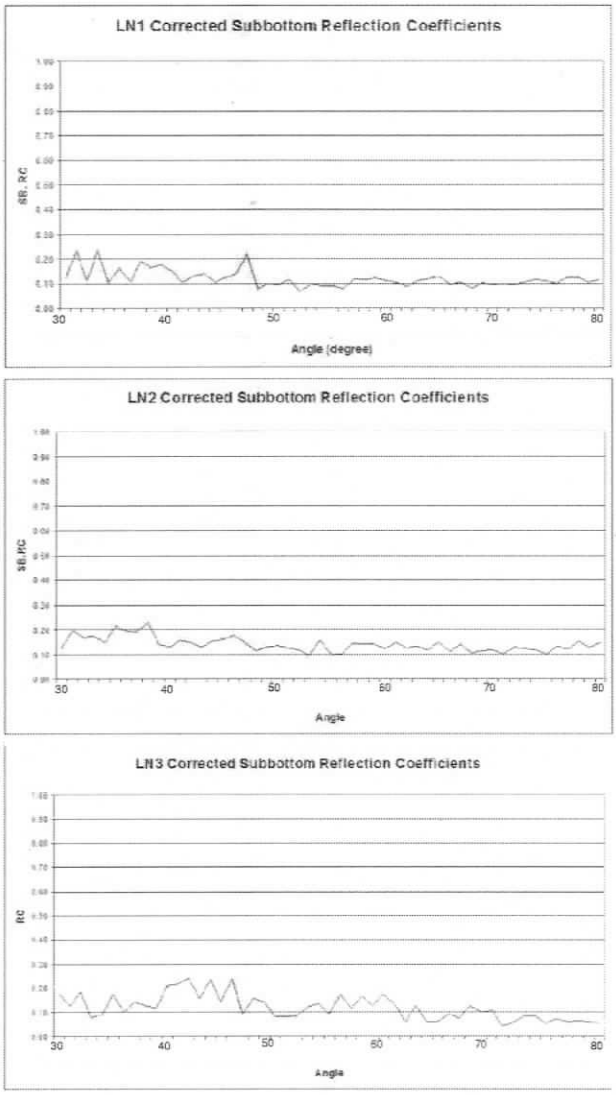

Figure 6.14: *Range and directivity corrected sub-bottom reflection coefficients versus grazing angle on Line 1, Line 2 and Line 3 from MC798.*

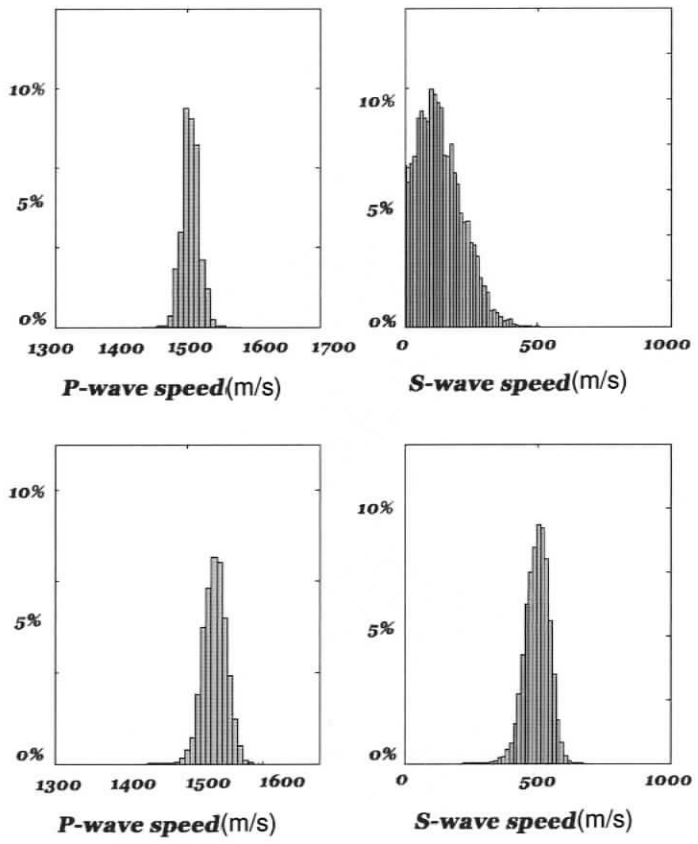

Figure 6.15: *Marginal probability distributions from the second AVA inversion with Line 3 data using the marginal PPDs from the first AVA inversion as prior. The first two plots represent the first layer (sea bottom), the second two histograms show the marginal PPDs for the second layer.*

MAP value for the second layer is slightly higher than the one for the first layer, so there is a small impedance contrast between the layers. The S-wave velocity has a wider distribution for the first layer and it favors the lower values. For the second layer, S-wave speed has a symmetric peak and the values are little high but not

unreasonable. Figure 6.16 shows the comparison between the first inversion (white) and the second inversion (grey) results for the first layer.

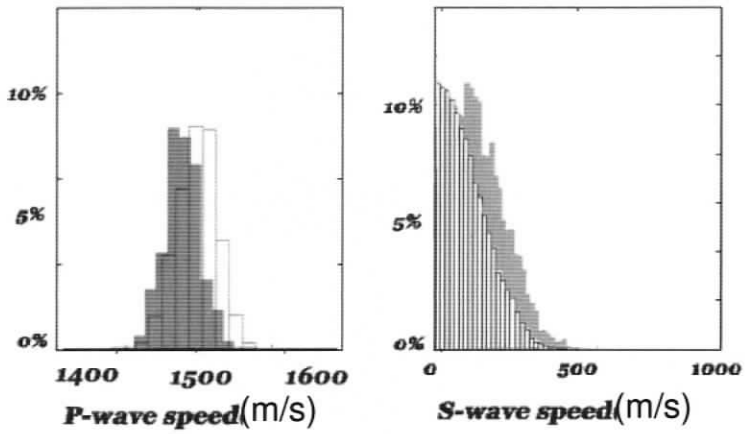

Figure 6.16: *Marginal probability distributions for the first layer in Line 3. The shaded histograms represent the marginal PPDs coming from the second inversion and the white histograms represent the inversion results for the first layer from the first inversion.*

The outcome of the second inversion for the first layer is in good agreement with the one from the first inversion. Both the mean and the MAP (maximum a posteriori) values are given in Table 6.4.

LN1 Sea-bottom	$v_p(m/s)$	$v_S(m/s)$	**LN1 First Layer**	$v_p(m/s)$	$v_S(m/s)$
Lower bound	1300	0	Lower bound	1300	0
Upper bound	1700	800	Upper bound	1700	800
Results:					
MAP	1465 ± 45	190 ± 186	MAP	1461 ± 44	475 ± 200
Mean	1500 ± 22	101 ± 139	Mean	1528 ± 37	448 ± 112
LN2 Sea-bottom	$v_p(m/s)$	$v_S(m/s)$	**LN2 First Layer**	$v_p(m/s)$	$v_S(m/s)$
Lower bound	1300	0	Lower bound	1300	0
Upper bound	1700	800	Upper bound	1700	800
Results:					
MAP	1476 ± 37	180 ± 180	MAP	1497 ± 44	510 ± 140
Mean	1510 ± 17	125 ± 115	Mean	1540 ± 27	598 ± 110
LN3 Sea-bottom	$v_p(m/s)$	$v_S(m/s)$	**LN3 First Layer**	$v_p(m/s)$	$v_S(m/s)$
Lower bound	1300	0	Lower bound	1300	0
Upper bound	1700	800	Upper bound	1700	800
Results:					
MAP	1490 ± 47	87 ± 190	MAP	1526 ± 55	491 ± 170
Mean	1505 ± 35	80 ± 200	Mean	1532 ± 48	423 ± 107

Table 6.4: Prior bounds and inversion estimates with standard deviation for the AVA sea bottom and sub-bottom data for Line 1, 2 and 3 from MC798 from the second inversion. Left column shows the results from the first inversion, right column shows the results from the second inversion.

The results presented in Figure 6.16 were achieved by using a fixed value of density for the second layer. As previously mentioned, the reason why the density parameter was fixed, was the concern about the scaling errors and that these errors may have impacted the ability to invert for the density. It is thought that the fixed density value may bias the inversion results. Therefore, an attempt was made to create a test to display how changes in density affect the inversion. The test aimed to do two inversions with -10% change and +10% change in density and see empirically what was the effect. The sensitivity of the AVA curve for the -10% and +10% density

change is shown in Figure 6.18. The AVA curve is shifted up as the effect of the +10% change. The curve is shifted down for the -10% change. Neither shift produce a change in shape. The 10% density change influences the reflection coefficient values and presents 0.18±0.05 sensitivity.

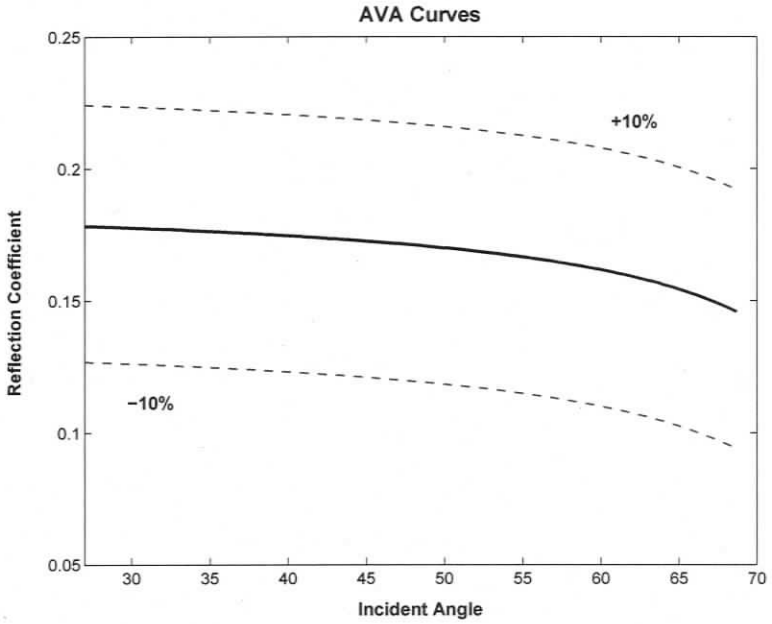

Figure 6.17: *AVA curve influenced by the density change. The black line represents the AVA curve between 27° and 70° with the actual fixed value (1500 kg/m^3). The red dotted lines show the AVA curves between 27° and 70° influenced by the -10% and +10% density change.*

The effect of -10% and +10% change in the P-wave speed influences the curve differently. It shifts the curve and changes its shape as well. With +10% the AVA curve favors the higher values. The -10% P-wave speed change lowers the values and

actually finds the angle of intromission in the given angle range. The 10% P-wave change presents 0.18±0.25 sensitivity. The sensitivity of the AVA curve for the -10% and +10% P-wave change is shown in Figure 6.18.

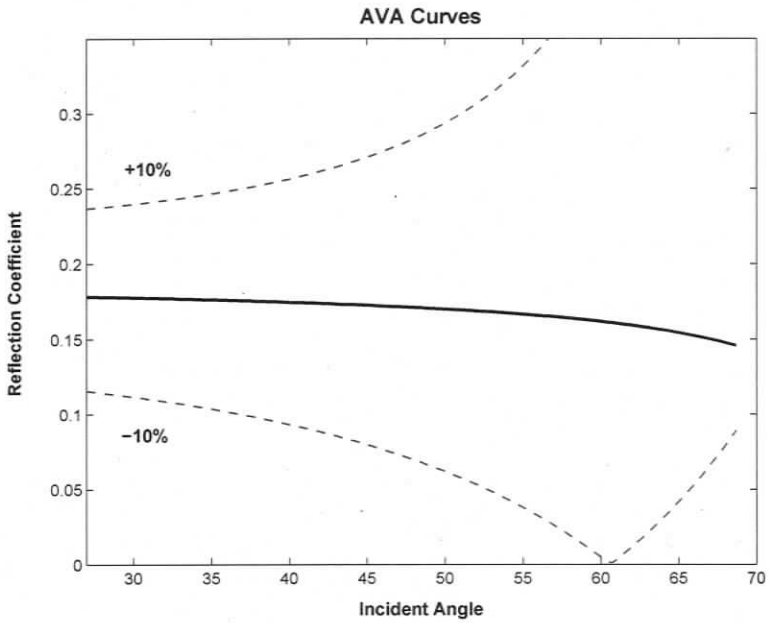

Figure 6.18: *AVA curve influenced by the P-wave change. The black line represents the AVA curve between 27° and 70° with the actual P-wave value. The red dotted lines show the AVA curves between 27° and 70° influenced by the -10% and +10% P-wave change.*

The effect of -10% and +10% change in the S-wave speed influences the curve slightly. It shifts the curve a bit up and down. Thist test shows that the S-wave is the least sensitive to the 10% change. The sensitivity of the AVA curve for the -10% and +10% P-wave change is shown in Figure 6.19.

The outcome of the inversions with the +10% and -10% density change can be seen

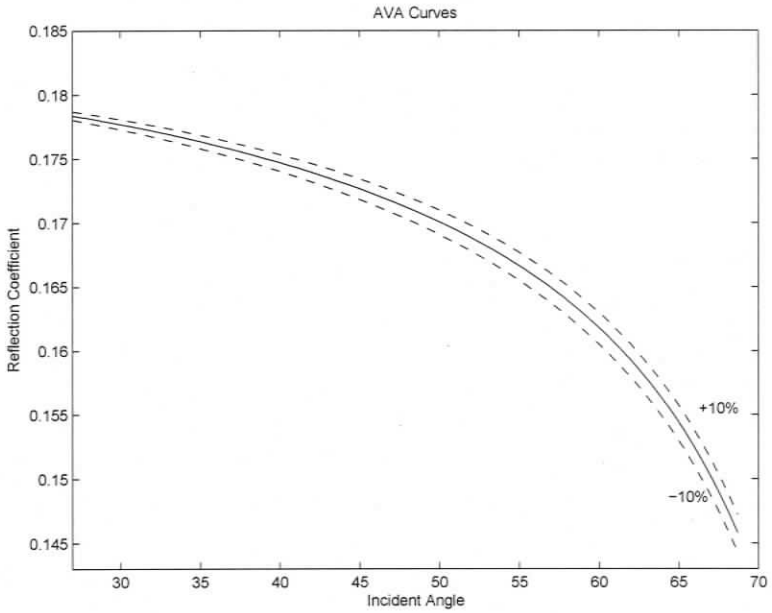

Figure 6.19: *AVA curve influenced by the S-wave change. The black line represents the AVA curve between 27° and 70° with the actual S-wave value. The red dotted lines show the AVA curves between 27° and 70° influenced by the -10% and +10% S-wave change.*

in Figure 6.20. The results show that the +10% change created unrealistic changes in the estimated values of the P-wave speed. The -10% change does not introduce significant differences in the distribution of the P-wave values. In each case, the S-wave speed of the sea floor sediment is influenced seriously and is forced to significantly larger values to compensate for the density change. This test demonstrates that the P-wave and S-wave values are sensitive to the unreasonable change in density and respond quite drastically. The study also shows that the parameters were more impacted by the higher density values (+10% change) then they are for lower (-10%

change). The outcome of this test shows that the fixed density based on the core value (1500 kg/m^3) and somewhat lower values are more accepted and likely to give reasonable results.

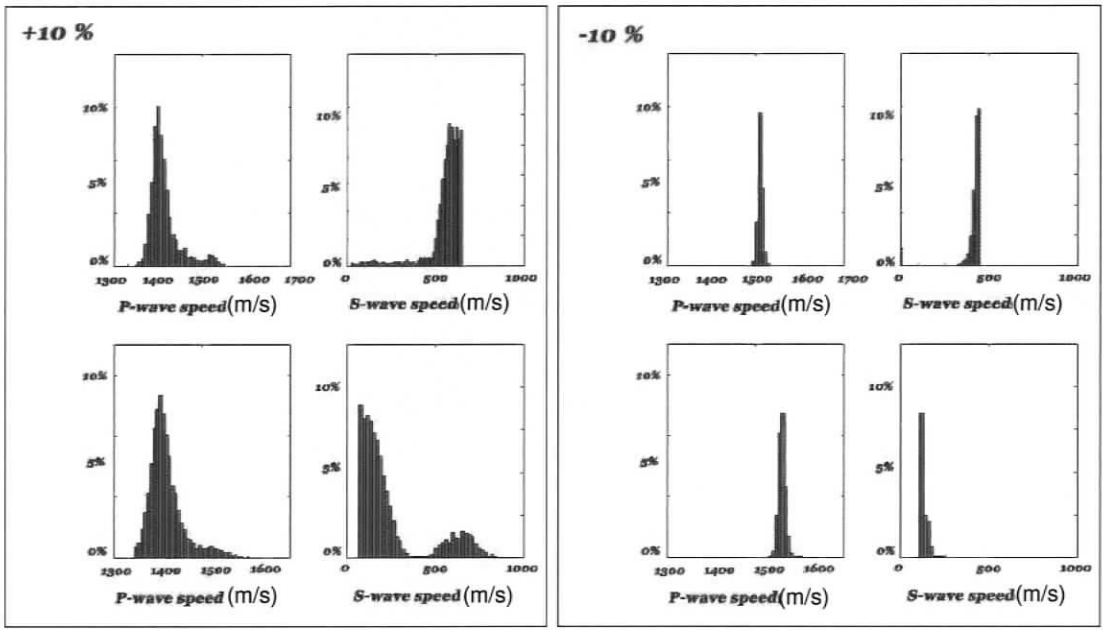

Figure 6.20: *Marginal probability distributions from the second AVA inversion with Line 1 data using the marginal PPDs from the first AVA inversion as prior. The first 2 plots represent the first layer (sea bottom), the second 2 histograms show the marginal PPDs for the second layer. At the left figure the density was fixed at 10 percent higher value at the right image at 10 percent lower than the one was used in the original inversion.*

6.6 VLA-AVA Conclusion

The amplitude analysis is a complicated process because of the type and the quality of the data. It needs to be shown that this dataset can be used in a type of investigation such as AVA. The clipped direct wave and the water leak introduced errors into

the scaling procedure. The calculated reflection coefficients provide estimates for the properties of shallow sediment in MC798. The results of this investigation are consistent with the suspected shallow sedimentary settings in the area. The inversions indicate low-velocity material with an average reflection coefficient of 0.2. This also corresponds well with areas with similar geographical settings in the northern Gulf of Mexico. In this investigation it is shown that the VLA-AVA analysis is a useful tool to gain better understanding of the sedimentary settings. For future surveys, the data quality is very important in any AVA research and it influences the overall success of this type of study. Recording the direct wave unclipped and controlling the hydrophones better with less timing errors would provide better data and less uncertainties in the inversion.

Chapter 7

Integrated Inversion Model of the Hydrated Sediment

7.1 VLA Velocity Inversion

In this study, several types of travel-time inversion methods were used to determine an integrated velocity model of the hydrated sediment in MC798 using VLA data. First, the velocity analysis to achieve NMO correction provided interval velocity profiles separately for each line and for each receiver (Figure 5.8). The interval velocities for twelve CRGs in the array have been averaged to represent the overall interval velocity model for each line. The averaging was done with the twelve time corrected velocity profiles. The averaged NMO velocity profiles for Line 1, Line 2 and Line 3

are represented in Figure 7.1.

Second, the migration velocity analysis provided the velocities to carry out the pre-stack depth migration on the VLA data. This process constructed a velocity structure model for the sub-surface, and was applied to obtain a velocity model separately for twelve receivers and for each line (Figure 5.13). The models for all the receivers were averaged to create an average migration velocity model for each line. Figure 7.2. displays the averaged migration velocity profiles for Line 1, Line 2 and Line 3 from the migration velocity analysis.

Figure 7.3 shows the results of the integrated interval velocity and migration velocity profiles over all hydrophones for Line 1, Line 2 and Line 3. The velocity model displays several different layers. The first layer shows very low velocity (close to water velocity about 1486 m/s), the thickness about 40 m. This low velocity might refer to young, muddy sediment with high porosity.

The next layer indicates little increase in the velocity (approximately 1516-1530 m/s) and appears to have about 40-45 m thickness. The third main layer is about 120 m thick and has an average interval velocity about 1550-1610 m/s. The fourth layer has about 35-40 m thickness and an average velocity about 1620-1670 m/s. The next layer has an average velocity about 1660-1700 m/s and it is about 90 m thick. The sixth layer starts at about 350 m with an average velocity about 1700-1760 m/s. Table 7.1 summarizes the velocities for each layer from the NMO velocity, the migration

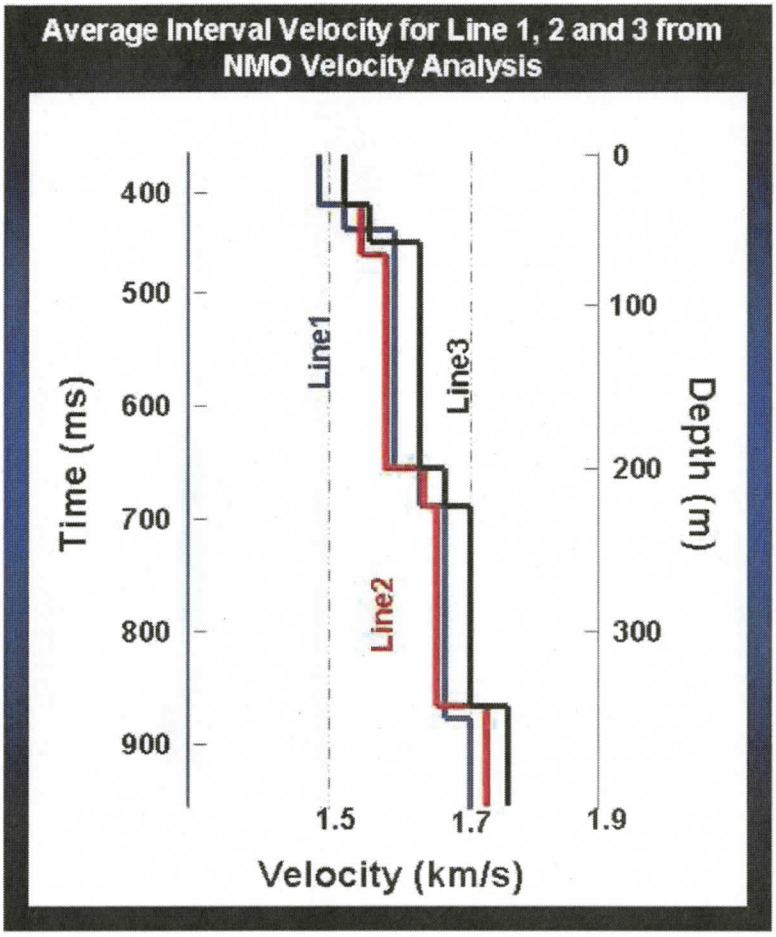

Figure 7.1: *Average interval velocities from the NMO velocity analysis for Line 1, Line 2 and Line 3. E1, E2 and E3 represent the main reflectors, for comparison with the inversions of Jaiswal [36].*

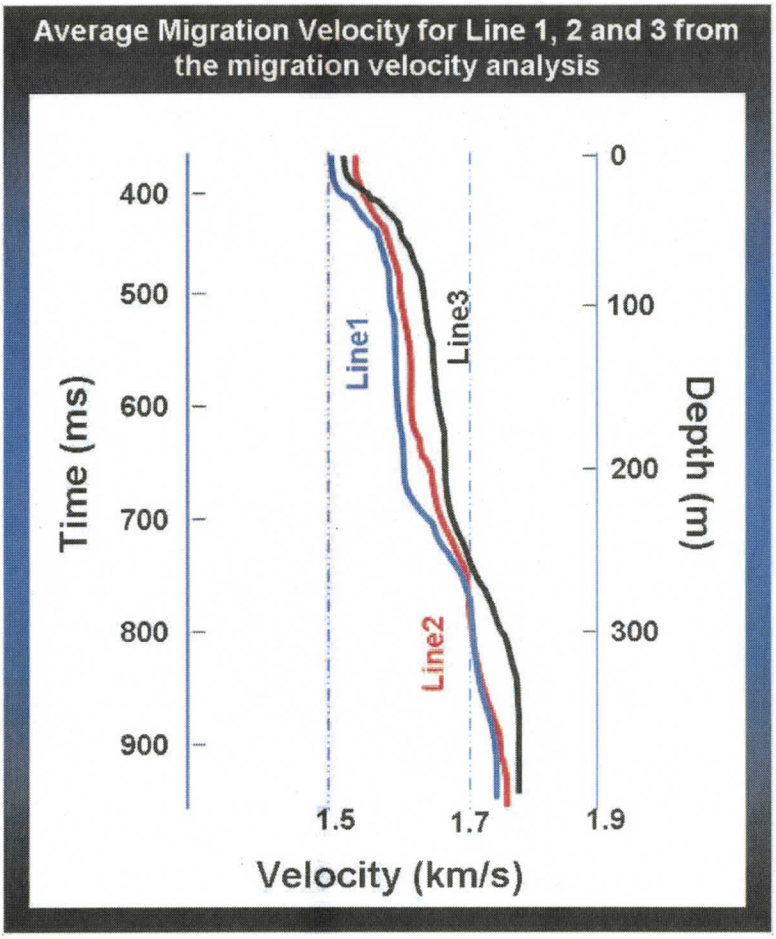

Figure 7.2: *Average migration velocities from the migration velocity analysis for Line 1, Line 2 and Line 3.*

Depth	NMO Vel.	Migration Vel.	Previous Studies
m	$v_p(m/s)$	$v_p(m/s)$	$v_p(m/s)$
$0 - 40 \pm 4$	1483 ± 10	1500 ± 10	
$40 - 80 \pm 7$	1519 ± 20	1517 ± 20	
$80 - 200 \pm 12$	1587 ± 35	1605 ± 30	1620
$200 - 240 \pm 19$	1645 ± 40	1655 ± 40	
$240 - 350 \pm 23$	1670 ± 50	1700 ± 50	1690
$350 - \pm 35$	1700 ± 60	1725 ± 60	

Table 7.1: Depths and velocities from the NMO correction, the migration velocity analysis with the errors for VLA Line 1 and from previous studies for GI Gun Line 11 [36].

velocity analysis and the velocities from previous studies with the calculated errors.

The previous seismic assessment studies on the OBS and the GI Gun datasets (Figure 7.4) [36] at an area close to the VLA location indicated similar velocities for the layers between reflectors E1 and E2, and E2 and E3. However, these studies did not give any information about the near-surface sediment above reflector E1 or for the layer beneath reflector E3.

The use of the amplitude versus angle information extracted from the VLA data provided the P-wave velocity and the density estimates and uncertainties of the very shallow sub-bottom sediment. These values have been compared with the NMO and migration velocities. This comparison is displayed in Table 7.2. for the sea floor and the first sub-bottom layer.

The AVA estimates corresponded well with the estimates from the travel-time inversion models. The two types of velocity analysis and the amplitude investigation

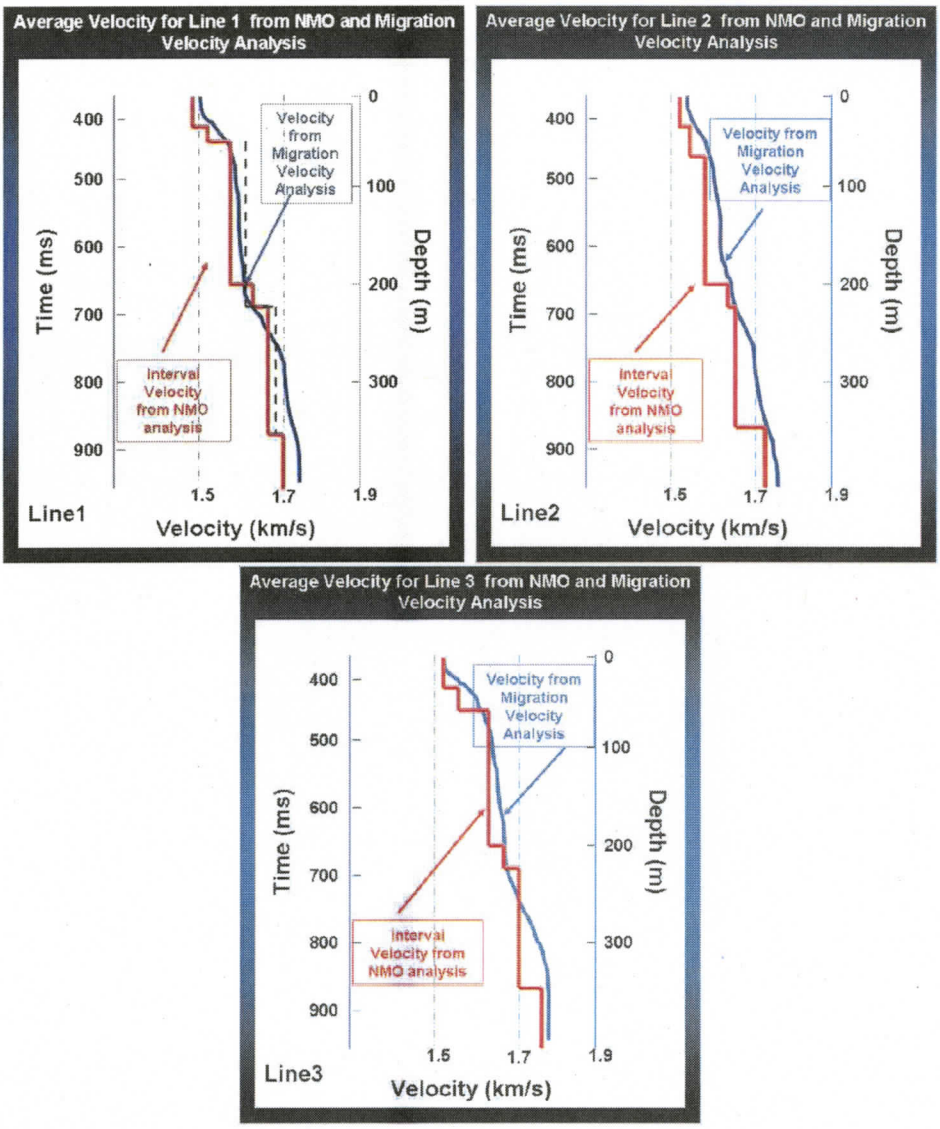

Figure 7.3: *Average migration velocities from the NMO velocity and the migration velocity analysis for Line 1, Line 2 and Line 3. On the first plot the black dashed line represents the velocities from a previous study [37] at the same location as the VLA.*

Line 1	Amplitude Analysis	NMO Velocity	Migration Velocity
Reflector	$v_p(m/s)$	$v_p(m/s)$	$v_p(m/s)$
Sea-floor	1485 ± 30	1483 ± 10	1500 ± 10
1st Reflector	1528 ± 26	1519 ± 20	1517 ± 20
Line 2	**Amplitude Analysis**	**NMO Velocity**	**Migration Velocity**
Reflector	$v_p(m/s)$	$v_p(m/s)$	$v_p(m/s)$
Sea-floor	1512 ± 28	1510 ± 10	1505 ± 10
1st Reflector	1540 ± 27	1535 ± 20	1538 ± 20
Line 3	**Amplitude Analysis**	**NMO Velocity**	**Migration Velocity**
Reflector	$v_p(m/s)$	$v_p(m/s)$	$v_p(m/s)$
Sea-floor	1505 ± 35	1508 ± 10	1500 ± 10
1st Reflector	1532 ± 40	1532 ± 20	1535 ± 20

Table 7.2: Velocities from the amplitude, the NMO velocity and from the migration velocity analysis for Line 1, Line 2 and Line 3.

indicated relatively low velocities (Table 7.2) in the shallow domain, consistent with results from core measurements (1489 m/s at the sea-bottom and 1520 m/s for the first layer) (Figure 6.13). The P-wave velocity increases gradually with depth to the estimated BGHS (approximately 350-400 m) below the seafloor.

7.2 VLA Image Quality

In order to make an assessment on the performance of the VLA data to image the structure in the hydrate bearing sediments in the Gulf of Mexico, several comparisons with other seismic methods were made. The high-resolution single-channel SSDR dataset was used to calibrate the VLA data. Figure 7.5 shows direct comparison between the VLA data and SSDR data for two lines on the same track. The VLA

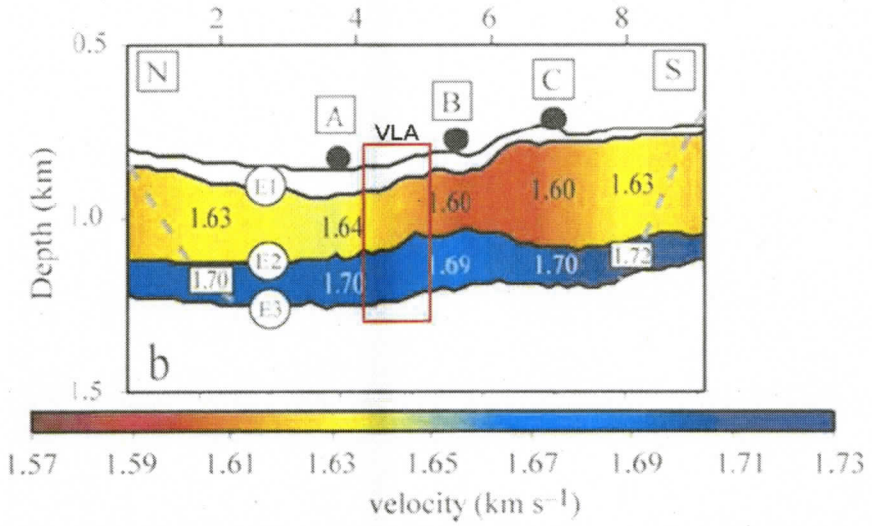

Figure 7.4: *Shallow velocity model for the area by Jaiswal [37]. A, B and C shows the positions of the OBSs on the sea-floor. E1, E2 and E3 display the strongest reflectors. The box displays the location of the VLA profile Line 1.*

data follows the same reflectors A, B and C.

Compared to the SSDR experiment, the VLA data were able to follow the main reflectors and image the main and micro layer structure in the sediment. Comparison can also be made between lines from the GI Gun dataset and VLA lines that were roughly on the same track. Line 11 from the G.I. Gun dataset is shown in Figure 7.6. This line covered a longer track than the VLA line (Line 1). The box in Figure 7.6. displays the portion of the section covered by the VLA line.

The comparison between GI Gun line 11 and VLA line 1 is shown in Figure 7.7. Both these lines have NS orientation and they were run 50 m apart on the same

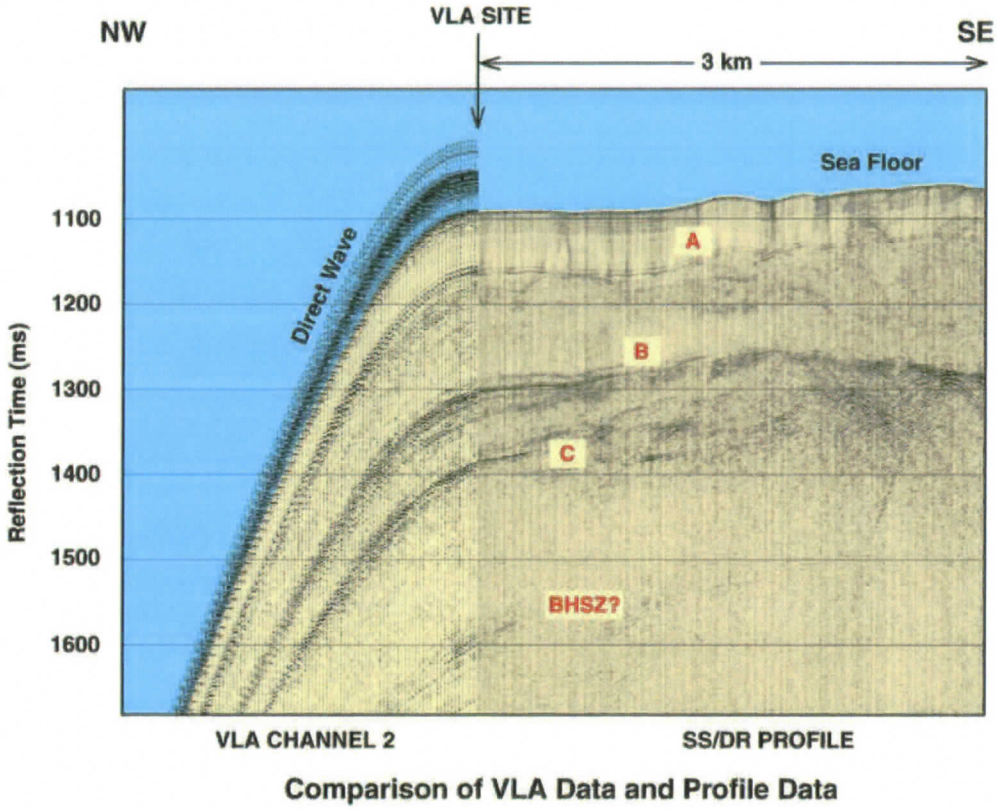

Figure 7.5: *Comparison of VLA data (Line 1) with SSDR data coming from the 2002 prototype VLA experiment.*

heading. The plotting options and gains were kept similar on the two sections. The right portion represents the GI Gun data and the left portion displays the VLA data. The migrated VLA data resolve three reflectors A, B and C, interpreted by Jaiswal et al. [37] as E1, E2 and E3. The comparison shows that the VLA data are useful for mapping continuous structure and capable of imaging the detailed structure of the sub-bottom. Figure 7.8 shows a direct comparison between the same section of the

GI Gun Line 11 (boxed section from Figure 7.6) and the VLA Line 1 profile. In this specific comparison between the GI Gun Line 11 and the VLA Line 1 some structures are more revealed in the VLA data then in the GI Gun data between reflector A and C. Reflector B appears stronger on the VLA data than on the GI Gun line.

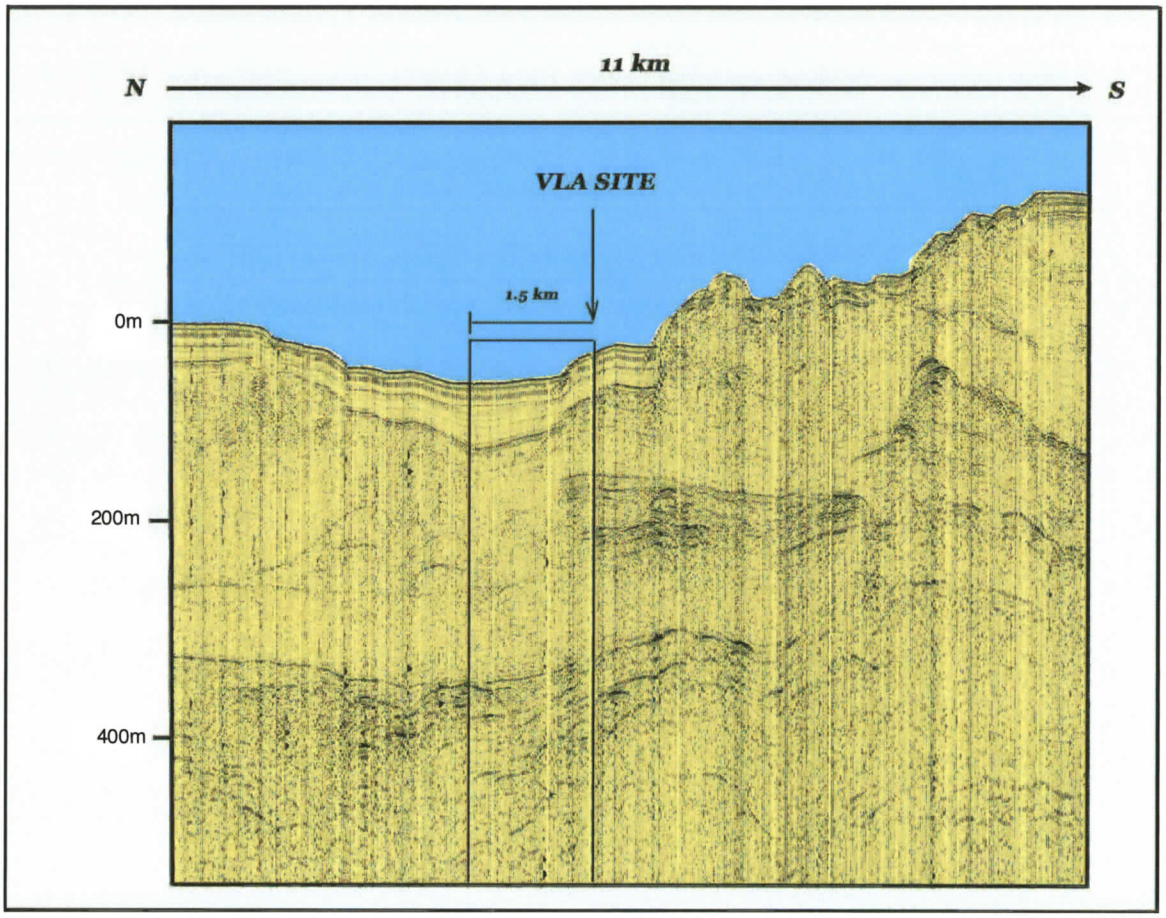

Figure 7.6: *High-resolution GI Gun data (Ln11). The profile shows the main reflectors that can be followed through the area. The rectangle shows where the VLA profile connects with this line.*

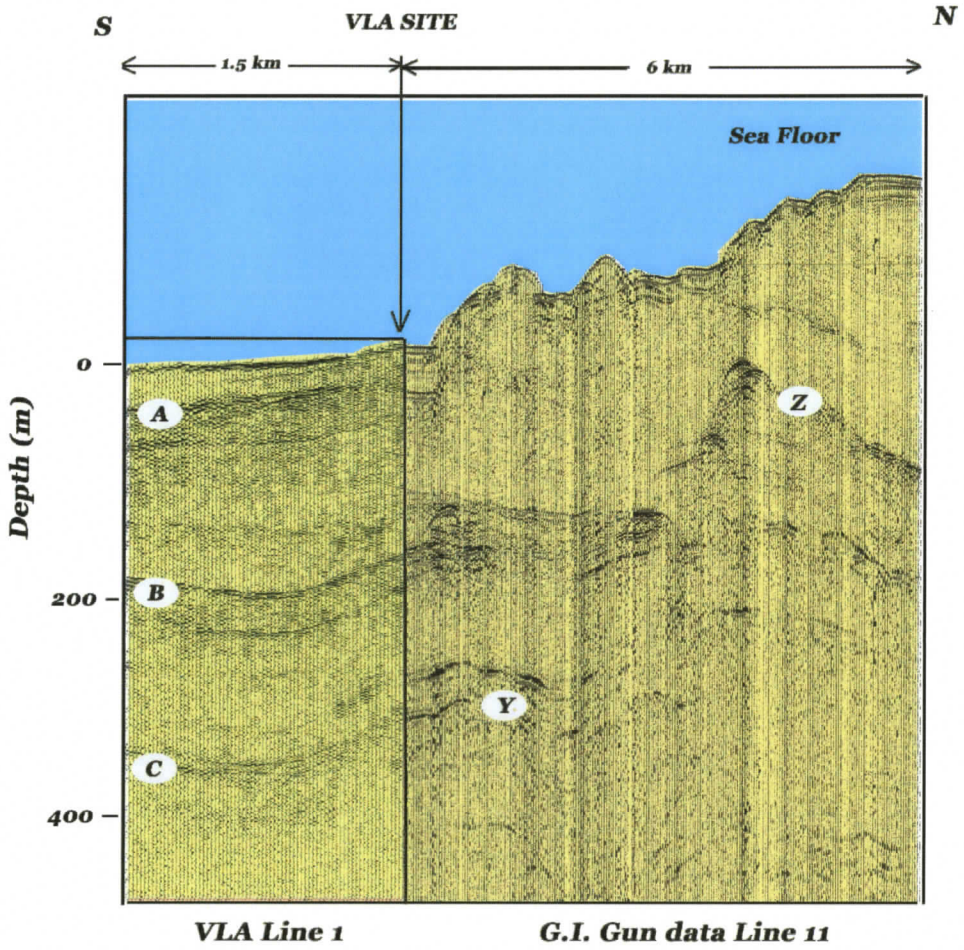

Figure 7.7: *Comparison of the conventional 2-D seismic (GI Gun data - right) and a selected, single, migrated common-receiver gather (channel-6) of the VLA data (Line 1 - left). A, B and C represent the major reflectors and Y, Z shows the wedge-shaped features.*

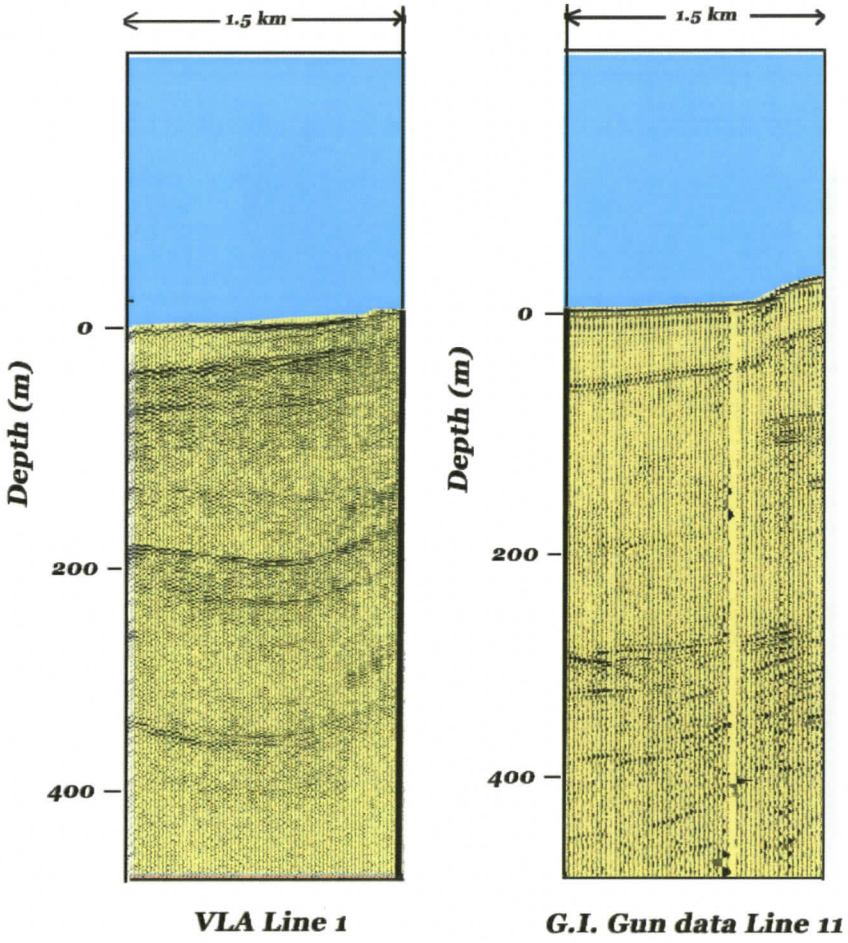

Figure 7.8: *Direct comparison of the conventional 2-D seismic (GI Gun data - right) and a selected, single, migrated common-receiver gather (channel-6) of the VLA data (Line 1 - left).*

7.3 Hydrate models for the study area

In the Gulf of Mexico, gas hydrates have been found in a number of surface expressions and piston cores. However, the classic seismic detection method - looking for relatively continuous BSRs - has not been successful in revealing hydrate reservoirs. Milkov and Sassen [51] postulate that, in the Gulf of Mexico, gas hydrate accumulations are concentrated along the rims of salt-withdrawal basins and over salt ridges where there is often fracturing and faulting. Fractures may act as conduits for the focused upward expulsion of fluids and methane gas.

The collected data in MC798 provide insight into the character of and dynamics of the processes active in this area. Interpretation by Geresi et al. [24] reveals the area to be characterized by high-energy mass-wasting, local uplift associated with salt diapirism and associated filling of inter-diapiric basins, and periodic episodes of erosion. Moreover, Geresi et al. [24] described evidence of significant fluid flux occurring through shallow seafloor faults and mud diapiric structures. The reflectors along the flanks of the Mississippi Canyon appear parallel with some thinning over bathymetric highs. There seem to be greater thickness variations along the western flank of the Canyon. A possible explanation provided by Lowrie et al. [47] is that this is due, in part, to the Coriolis effect on the descending turbulent clouds of water and fine-grained sediments overlying an advancing turbidity current. Such uniform, regionally constant, reflectors are indicative of low energy pelagic and hemi-pelagic

deposition. Sedimentological analysis of a giant piston core (28.5 m) collected by the RV Marion Dufresne in an adjacent and seismically comparable area, showed the sediments to be calcareous clays and silty clays (Brunner, personal communication, 2003). A geologically reasonable interpretation is that comparable sediments comprise these seafloor-following reflectors.

The VLA data provide new information from the travel time and amplitude inversions for comparing two possible interpretations.

According to the first interpretation, several wedge-shaped (diapir) features (marked as Y and Z in Figure 7.7) are present that are possibly caused by overbank deposits of a channel. This is a typical case of a channel deposit where the deposits along the channel axis are sandier and give rise to high reflectivity zones (HRZs), and the overbank deposits are shalier and have the shape of a wedge. HRZs are associated with a lateral lowering of velocity, suggesting that free gas is present along the channel axis. The sandy deposits along the channel axis are normally expected to have higher P-wave velocity than their surroundings. A high-porosity, unconsolidated sandy sediment zone would be an ideal host medium for methane because of their effective porosity and high permeability [34].

According to the second interpretation, the reflection from the top of the wedge-shaped feature (marked as Y on Figure 7.7) marks the gas hydrate-free gas contact. The stability diagram, constructed with a bottom temperature (8 °C) and range

of geotherms (25-40 °C/km) for this area [63], estimates the depth of the base of the GHSZ close to the top of the wedge and is consistent with this interpretation. The shape and the nature of reflectivity can be explained by assuming that the concentration of the gas decreases laterally away from the HRZs. Due to a decrease in gas concentration, the strength of the BSR decreases and the BSR eventually disappears when the gas concentrations are so low that the hydrates and free gas are no more in contact. This interpretation suggests that the upper 400 m in the region consists of fine-grained sediments with possible dispersed hydrate distribution within the GHSZ. This conclusion is consistent with the velocity model from the VLA that shows velocities not higher than the expected background velocities for similar areas and very little contrast at depths between reflectors B and C (Figure 7.7).

The sustainability of a gas hydrate system requires a dynamic equilibrium between gas entering into the GHSZ and gas diffusing out of it. If the first hypothesis is correct, the presence of gas hydrates within the diapir indicates that gas is being fed continuously into the diapir from the free gas accumulation in the axis of the channel. The sediments within the channel, being more permeable, act as a reservoir while the surrounding material being shalier, is much less permeable. This reduces the chances of gas being present in the study area apart from the channel axis, and therefore the hydrates may not be present anywhere else apart from the region close to the diapir. If the second hypothesis is correct though, hydrates may be prevalent in the basin

above the BSR consistent with depths roughly equivalent to reflector C. The presence of hydrates is possible above the BSR but nothing can be said about other parts of the study area. Several coring experiments have been carried out in MC798 and no hydrate has been discovered except from the Neurauter and Bryant experiment in 1989 [53]. The low velocity sediment at shallower depths ($\sim$ 250 m) indicates that there is overall very low concentration of dispersed hydrate, and also suggests that there is not likely to have massive hydrate in the upper sedimentary section.

An attempt was made to calculate the gas hydrate saturation in MC798 using the velocities calculated from the travel-time inversion as background velocity. The velocity of fully hydrate-saturated sediment can be obtained for the combination of pure gas hydrate and sediment matrix. The velocity is then combined with the velocity of the water-saturated sediment (zero hydrate saturation) to determine the overall velocity [74].

The fully hydrate-saturated sediment velocity V_{hysed}, can be written as:

$$\frac{1}{V_{hysed}} = \frac{\phi}{V_{hydrate}} + \frac{1-\phi}{V_{matrix}}, \tag{7.1}$$

where $V_{hydrate}$ is the P-wave velocity for pure gas hydrate and is taken to be 3730 m/s [70], V_{matrix} is the P-wave velocity of the sediment matrix, taken to be 4500 m/s [11] and ϕ is the sediment porosity. According to porosity measurements from the piston core data (Figure 6.13, the typical porosity is about 55% and the calculated

V_{hysed} is about 4040 m/s, respectively. The velocity of partially hydrate-saturated sediment, V_p can be written as:

$$\frac{1}{V_p} = \frac{S}{V_{hysed}} + \frac{1-S}{V_{sed}}, \tag{7.2}$$

where V_{sed} is the water saturated sediment velocity and S is the fraction of the hydrated sediment in the pore space. V_{sed} is known from the travel-time inversion and was assumed to be the background velocity because the interpreted velocity profile does not show any obvious indication of gas hydrate which would deviate from background. Figure 7.9 displays the velocity curve changes for different hydrate saturation levels. Figure 7.10 represents the porosity changes versus the velocities for different hydrate saturation. Five different hydrate saturation level were calculated here (0.1%, 0.5%, 1%, 5% and 10%). Figure 7.9 shows that 0.1%, 0.5% and 1% hydrate concentration in the sediment is in the error range of the calculated velocity. This study shows that only very low concentration of hydrate might be possible in the sedimentary section.

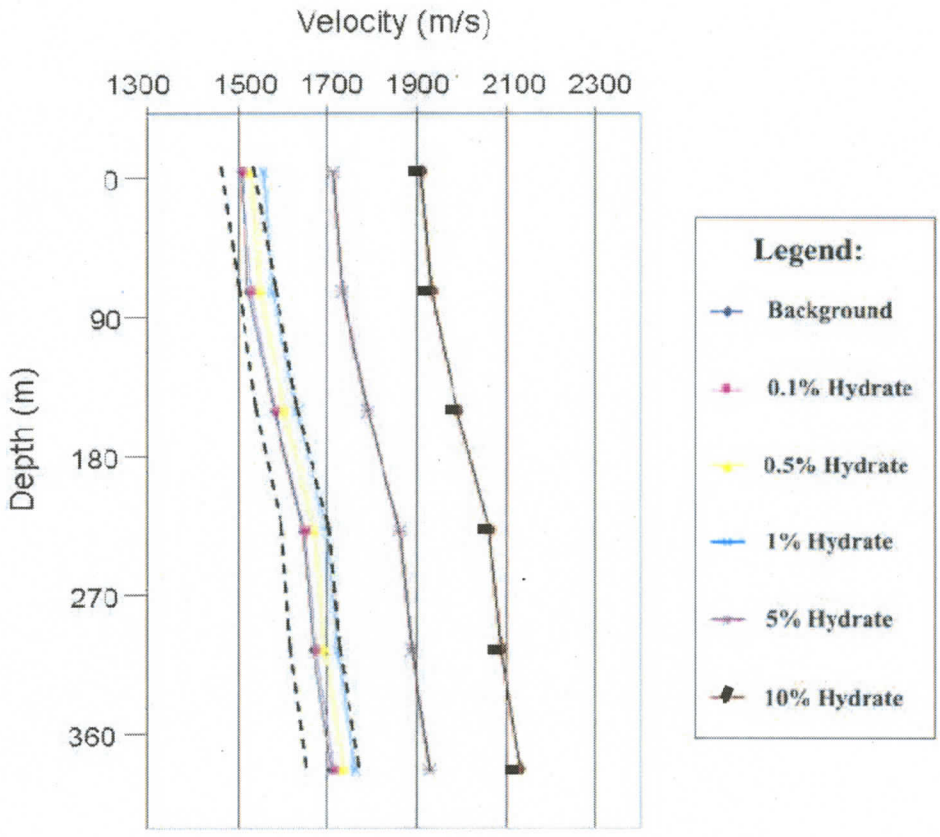

Figure 7.9: *Velocities of the hydrate saturated sediments. The lines with the different colors represent different hydrate percentage in the sediment. The dotted lines represent the calculated, background velocity error ranges.*

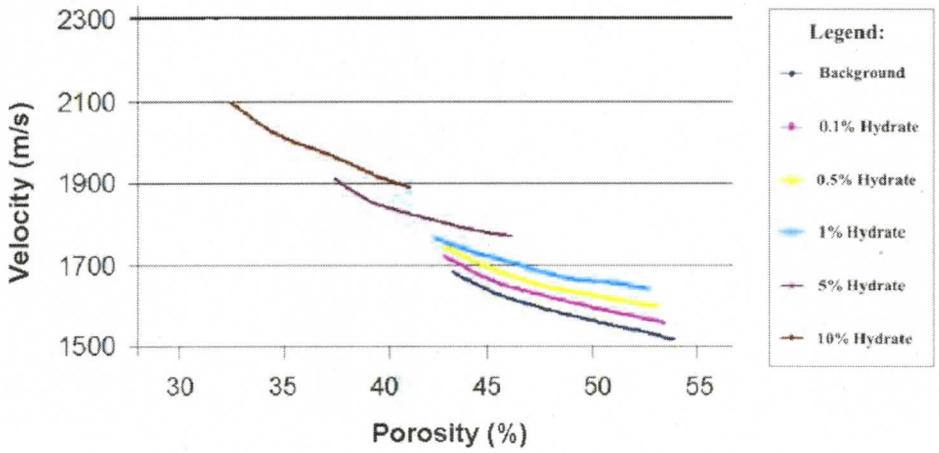

Figure 7.10: *Porosity changes with depth for hydrate saturated sediment. The dark blue line represents the background velocity and porosity. The maximum hydrate concentration that could exist consistent with the error bounds is 0.5-1 % of the pore space.*

Chapter 8

Summary and Conclusions

8.1 New techniques

The primary goals of this study have been to gain insights into the high-resolution vertical line array (VLA) technique and to assess its performance to obtain better imaging and understanding of the gas hydrate stability zone in the northern Gulf of Mexico. Several conventional (horizontal receiver style) processing algorithms such as NMO correction, stacking, migration, etc. were revalidated and recalculated to determine if these processes were applicable in the VLA common-receiver gather processing. In the framework of this study on the high-resolution VLA experiment from Mississippi Canyon Block 798 by the CMRET in 2002 and 2003, several new techniques were developed and applied to the data. A new methodology has been

developed for processing the VLA data that took into account the vertical acquisition geometry by integrating different processing techniques to extract travel time information. This research shows that many of the conventional seismic data processing techniques can not be applied to the VLA data because of the vertical arrangement of the receivers. In some cases the data sorting technique prevents them from presenting meaningful results. However, other important processing methods can be implemented into the VLA processing sequence. This investigation revealed these methods and presented the way they can be applied to the VLA data. These methods allow the user to efficiently process the VLA data and to carry out travel time inversion for a detailed velocity model to gain better understanding of the structure of the hydrate bearing sediment.

Amplitude analysis was applied to the VLA data using Bayesian inversion approach to provide estimates and uncertainties of the elastic physical parameters at an interface. The complicating factors consisted of the common receiver gather geometry, the sea water leakage problem and the clipped direct wave on the data. A model of the shallow sedimentary section was developed and proved that the VLA dataset can be successfully used for the mapping of the reflection coefficient distribution along the interface, both the sea floor and within the sedimentary section.

This research is part of the development of the gas hydrate monitoring station project in the northern Gulf of Mexico. It is also one of the first attempts to use VLA

data to image the gas hydrate stability zone.

8.2 Scientific results

An integrated velocity structure model was constructed for the sub-surface using travel time inversion from interval velocity analysis for the NMO correction and from migration velocity analysis for the phase-shift migration. The results from the travel time inversion reveal relatively low velocity structure in the GHSZ which is in good agreement with the previous seismic assessment studies on OBS and GI Gun datasets (Figure 7.4) [24], [36] at a site close to the VLA location. The average velocity profile for the site starts with low compressional velocities close to those in the sea-water $\sim$ 1500 m/s, and increases to around 1750 m/s at the suspected BGHSZ ($\sim$ 400 m).

However, these studies did not give any information about the near-surface sediment structure.

Models of sea floor and the first sub-bottom reflection coefficients were also calculated from amplitude data to gain a more detailed view of the P-wave and density distribution of the sea floor and the sub-seafloor. This model reveals a low velocity zone in the shallow region, consistent with results from core measurements (Figure 6.13) and from the velocity inversion.

The VLA data have been compared with conventional seismic data from different experiments to assess its performance to image structure in the hydrate bearing

sediments. First, the VLA data were compared to the high-resolution single-channel SSDR dataset from 2002 that was used to calibrate the VLA data. The assessment shows that the VLA data were able to follow the main reflectors and image structure in the sediment. Second, a comparison was also made between lines from the GI Gun dataset from 1998 and VLA lines that were roughly on the same track. This analysis demonstrates that the VLA technique was able to create an interpretable image of the sub-bottom and image deeper reflectors and micro-reflectors. In this particular comparison, the VLA data have better reflectivity contrast for the deeper layers and extract more detail about the layer structure between sub-bottom reflectors.

Based on the integrated velocity structure model from the travel time inversion and the amplitude analysis of the VLA data and the previous studies by Geresi et al. (2002), two possible scenarios are proposed in this study.

The first scenario suggests that the high reflectivity zones visible in the profiles are associated with a lateral lowering of velocity, suggesting that free gas is present along the channel axis and the sandy deposit acts as bearer. The sandy deposits that can be along the channel axis are expected to have higher P-wave velocity than their surroundings. The possible presence of gas hydrates within the diapir would indicate that gas is being fed continuously into the diapir from the free gas accumulation in the axis of the channel. The sediments within the channel, being more permeable, act as a reservoir while the surrounding material, being shalier, is much less permeable. This

reduces the chances of gas being present in the study area apart from the channel axis, and therefore the hydrates may not be present anywhere else apart from the region close to the diapir.

The second scenario proposes that the reflection from the top of the wedge-shaped feature marks the gas hydrate-free gas contact. Heat flow measurements also indicate that the GHSZ is about 400 m which is consistent with the assessments here. The shape and the nature of reflectivity of these features can be explained by assuming that the concentration of the gas decreases laterally away from the HRZs. Due to a decrease in gas concentration, the strength of the BSR decreases and the BSR eventually disappears when the gas concentrations are so low that the hydrates and free gas are no more in contact. Therefore, the presence of hydrates is definite above the BSR but nothing can be said about other parts of the study area.

The data and the integrated velocity model support both of these scenarios. In order to decide which hypothesis is more relevant for the study area more investigations are needed.

8.3 Future suggestions

For future VLA investigations several suggestions can be made based on the results and experience of this study. Some associated measurements such as sound speed profile and acoustic doppler current profiles or tilt meter on the individual receivers

are very important at any VLA experiment. Having good control on the timing of the VLA is also very important to avoid some later corrections and related errors and therefore save valuable computational time. The usage of an omni-directional source is also suggested to avoid directionality on the data. Analysis of the data coverage prior to the VLA survey would be essential to achieve success. Using ray tracing on synthetic data that mimic the realistic VLA scenario well enough would satisfy this goal. To have some information about the geographical settings, multi-beam data/sub-bottom profiler data would also help picking the best VLA development site. It is also important to record the data with unclipped direct wave signature. This process can be difficult to manage. It can be achieved with setting one hydrophones with lower gain to make sure that at least the direct wave will not be clipped on one channel. After the first recovery of the VLA data some onboard processing is necessary to recalibrate the gains of the hydrophones if needed. The onboard processing and quality control are essential to make sure that the required data quality is achieved. This would give better control on the amplitudes for possible future amplitude analysis as well.

Appendix A

Geophysical data in AT14 of the northern Gulf of Mexico

In May 2003, USGS conducted a 14-day cruise aboard R/V Gyre to collect high-resolution seismic reflection data and develop the geologic framework around two potential deep-water sites anticipated to be drilled in the spring of 2004 to study gas hydrates in the Gulf of Mexico. The Gyre cruise (USGS cruise ID: G1-03-GM) [35] is one part of a much larger program of hydrate research in the Gulf of Mexico. Specifically, the cruise is coordinated with a Joint Industry Program funded by the Department of Energy to assess the hazard that hydrates pose to deep-water drilling.

Objectives

The primary objectives of the Gyre cruise were:

- Characterize the shallow seismic stratigraphic framework of the two site survey areas: This objective addresses understanding the geologic framework of each site, i.e. to understand the stratigraphic and structural relations and how they might affect or alter hydrate occurrence. Success in meeting this objective requires collecting seismic reflection data sufficient to image the subbottom environment in which gas hydrate might occur and to relate local features to the broader understanding of the geology of the basins and structural highs in the Gulf of Mexico.

- Acquire data to map the distribution of acoustic indicators of gas hydrate. Several seismic indicators exist for identifying hydrate in the subsurface: the bottom simulating reflection (BSR), zones of amplitude blanking, and zones of enhanced reflections which may indicate the presence of free-gas trapped beneath the hydrate stability zone. Understanding the spatial distribution of these indicators can help determine the likely presence of hydrate in the sediments, as well as the places where hydrate may be most concentrated (and therefore a target for a drilling experiment). Good spatial coverage of high-quality, high-resolution data are needed to meet this objective.

Seismic Systems

The components for the multichannel seismic system consisted of the source, the receiving array, and the digitizing and recording PCs. Two sources were used: a

Seismic Systems, Inc. 15 in^3 water gun (operated at 2000 psi pressure), and a Seismic Systems, Inc. Generator-Injector (GI) gun (operated at 3000 psi pressure). A Bauer, 4-cylinder, 50-SFPM (standard cubic feet per minute) diesel compressor provided the high-pressure air for the guns. The GI gun is a dual-chamber air gun designed to minimize the bubble pulse. The injector chamber of the GI gun is timed to discharge a short time (typically 20-30 msec) after the generator chamber so as to suppress the bubble pulse and create an optimal signal. It was used with chamber inserts for a 13/13-in^3 configuration (i.e., 13 in^3 generator chamber, 13 in^3 injector chamber) for most of the cruise and was fired at 20-m intervals. The water gun was used for a test line at the beginning of the cruise and could be fired at 10-m shot intervals because it has only a single chamber. Firing was by distance (10-m shots for the water gun, 20-m shots for the 13/13 GI gun; 30-m shots for the 24/24 GI gun). The firing pulse generated by YoNav went to a SEAMAP Seislink seismic interface box, then into a Sureshot computer system (version 3.06) which enabled optimizing firing between the generator and injector chambers. Data were digitized and recorded at a sample interval of 0.5 ms. Record lengths were 4 s with a 1 s deep-water delay (i.e., 1-5 s record window) except for lines where the sea floor was shallower than 1 s [35].

Recording Conditions and Data Quality

A total of 253 km of MCS data along 35 short lines were collected during the survey in the Atwater Valley 14 lease block. Profiling was designed around detailed

north-south and east-west surveys (5 km long lines each 100 m apart) of each of the three vent/mound sites identified by the JIP as hydrate targets. The image quality in general was good (the raw data is shown in figure 9.1 upper panel)

Knudsen data quality in Atwater Valley was dependent on the weather. As the winds and seas moderated during the time spent at the Atwater site, the quality of the bathymetric record improved. In general, the bottom return was strong with few subbottom reflections, suggesting a harder, more reflective sea floor. The long line collected northwestward along the axis of the Mississippi Canyon crossed regions of varying sea floor returns, including many layered units within the subbottom, showing the variations in bottom type within the floor of the Canyon.

Basic Data Processing

The data were both processed on- and off-board using mostly Promax and Focus processing software. Several conventions were followed in the processing: original ffid's were preserved, but all shots were renumbered starting at 1 at the beginning of every line. All geometry was calculated in absolute coordinates, i.e., UTM positions calculated from the latitude/longitude positions supplied by YoNav. The Atwater Valley region was in UTM zone 16. The initial geometry definition involved extracting the position information from the headers in the SEG-D field records, calculating a corrected UTM x and y position for the actual shot location (using a combination of MATLAB and ArcGIS), then using ProMAX to do full geometry to accurately locate

all CDP and receiver locations. The SEG-Y data with geometry were read back into FOCUS for processing through stack. Although data were recorded to 5 s, stacks were only done to 4.5 s. Stacking was not sensitive to velocities because of the short streamer length (240 m) and large water depths (1300 m). A generic velocity was used that consisted of 1500 m/s rms to the sea floor, then increasing linearly to 2000 m/s at 3 s twtt and 2500 m/s at 4.5 s twtt. For the multichannel data with the 13/13 GI gun, data generally were stacked to 6 fold at 5-m CDP spacing. Final navigation was extracted from the CDP locations and converted back to latitude and longitude values.

The main processing steps can be concluded as following [76]:

- Reformatting, editing, amplitude balancing,
- Detrending,
- Deep-water delay correction,
- FK Filtering,
- Spiking Deconvolution,
- NMO Correction,Stacking,
- Spherical Divergence Correction,
- Bandpass Filtering,

- Multiple Suppression.

  A multiple elimination strategy was used, using a well-known subtraction technique, to improve the strength and continuity of the deeper reflections. This technique predicts the multiple energy using predictive deconvolution and then subtract it from input seismic data.

The results of the processing on an example profile, coming from Atwater Valley 14 area, is shown in Figure 9.1. lower panel.

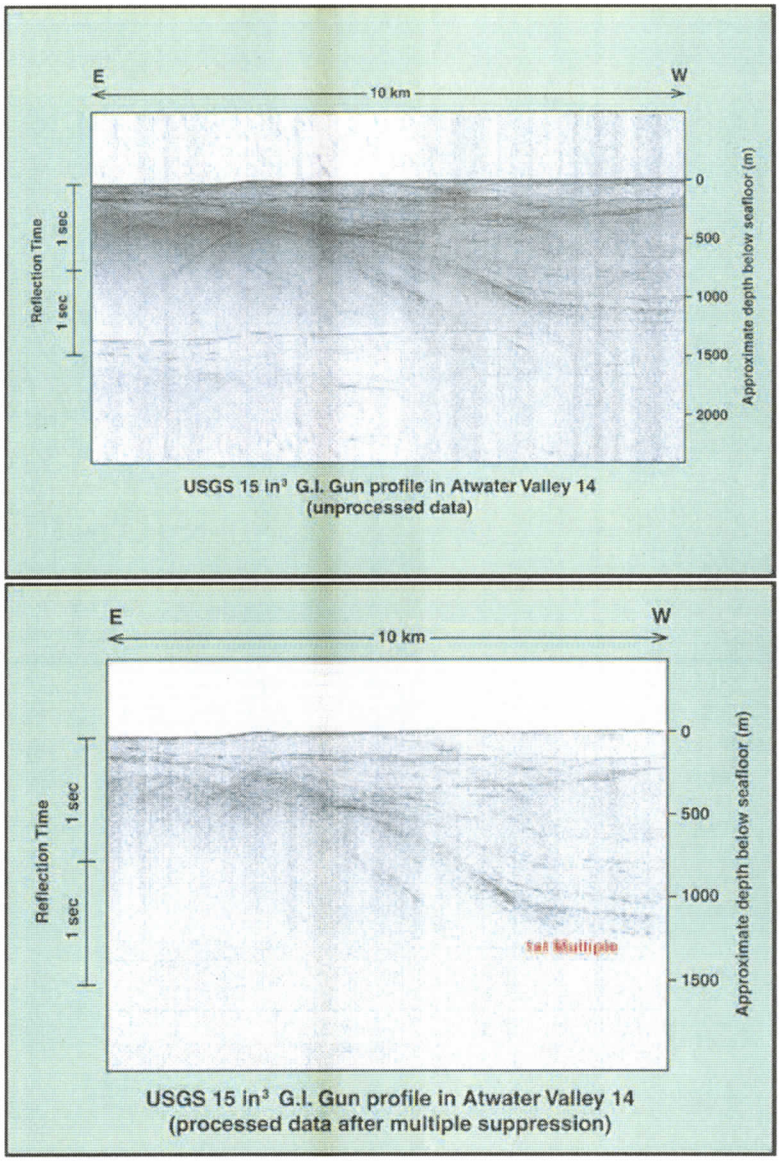

Figure A.1: *Example from the 2003 USGS dataset (Line 97) from Atwater Valley. The first image represents the raw, unprocessed data and the second image shows the processed image with multiple suppression [26].*

Appendix B

Travel-time Inversion for the VLA Geometry

The travel-time equation was examined in this study for CRG to obtain reliable velocities and depths for the sedimentary part of these types of models. Travel-time equations have been studied extensively in the last decades. Many authors ([20], [52], [54], [21], [13], etc.) have published different travel-time equations and their proofs. However, most of the equation were developed for refractions and for conventional geometries. Johnson (1976) presented a generic equation for travel-time with thickness and ray angles with reference to the vertical. Guimareas [31] also derived the 2-D travel-time equation for vertical cable geometry.

This study will focus on 2-D common receiver gather geometry to calculate the

2-D travel-time equation for dipping interfaces.

An analytic proof for the 2-D travel-time equation is presented that is generic for n layers. The offset is handled as a function of slowness [31]. The travel-time equation also describes trajectories in the $\tau - p$ domain. In this domain it is possible to estimate the slowness at the source and at the receiver location using 2-D or 3-D trajectories.

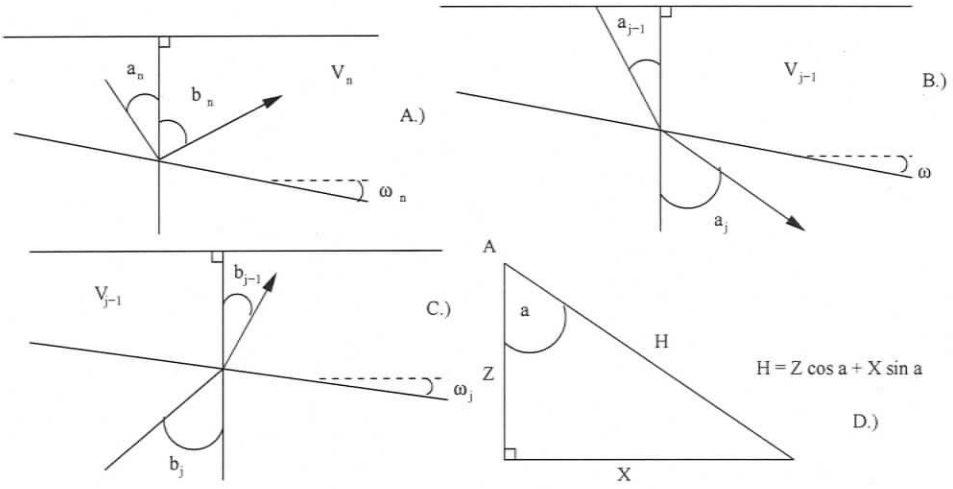

Figure B.1: *Relationship of the down-going and up-coming rays at the reflection interface $n(A)$. Relationships of down-going (B) and up-coming (C) rays, respectively, with a dipping interface and its angles with the vertical. The way the ray H is decomposed into its vertical horizontal contributions according to the angle a. (D)*

Assume two positions at the surface: A, where the down-going rays depart, and B, where the up-coming rays are observed. The horizontal slowness can be expressed by:

$$Pa_j = \frac{\sin a_j}{v_j} \qquad and \qquad Pb_j = \frac{\sin b_j}{v_j} \tag{B.1}$$

where a_j, b_j are angles which the down-going and up-coming rays make with the vertical in the j^{th} interface. The vertical slowness can be expressed by:

$$qa_j = \frac{\cos a_j}{v_j} \qquad and \qquad qb_j = \frac{\cos b_j}{v_j} \tag{B.2}$$

Using Snell's law and the relations of the angles a and b with the normal at the interface (A), the relationship between the down-going and the up-coming rays for a reflection on a planar dipping interface n can be expressed by:

$$Pa_n - Pb_n = -(qa_n + qb_n)\tan\omega_n \tag{B.3}$$

In the same way, the relationship between transmitted rays on each planar dipping interface j may also be expressed in term of slowness:

For the down-going rays $(B.)$:

$$Pa_{j-1} - Pa_j = (qa_j - qa_{j-1})\tan\omega_{j-1} \tag{B.4}$$

For the up-coming rays ($C.$):

$$Pb_j - Pb_{j-1} = (qb_j - qb_{j-1}) \tan \omega_{j-1} \tag{B.5}$$

According to Figure 8.1D the travel-time of each ray segment can be decomposed using equation 1 and 2, into vertical and horizontal contributions using the angles with the vertical.

For models with n dipping layers (Figure 10.2) a ray that goes from A and reflects at n^{th} interface and is observed at B, has the total travel time expressed by:

$$T = \sum_{j=1}^{n} Pa_j(Xa_{j-1} - Xa_j) + \sum_{j=1}^{n} qa_j(Z_j + Xa_{j-1} \tan \omega_{j-1} - Xa_j \tan \omega_j) + \tag{B.6}$$

$$+ \sum_{j=1}^{n} Pb_j(Xb_{j-1} - Xb_j) + \sum_{j=1}^{n} qb_j(Z_j - Xb_{j-1} \tan \omega_{j-1} + Xb_j \tan \omega_j)$$

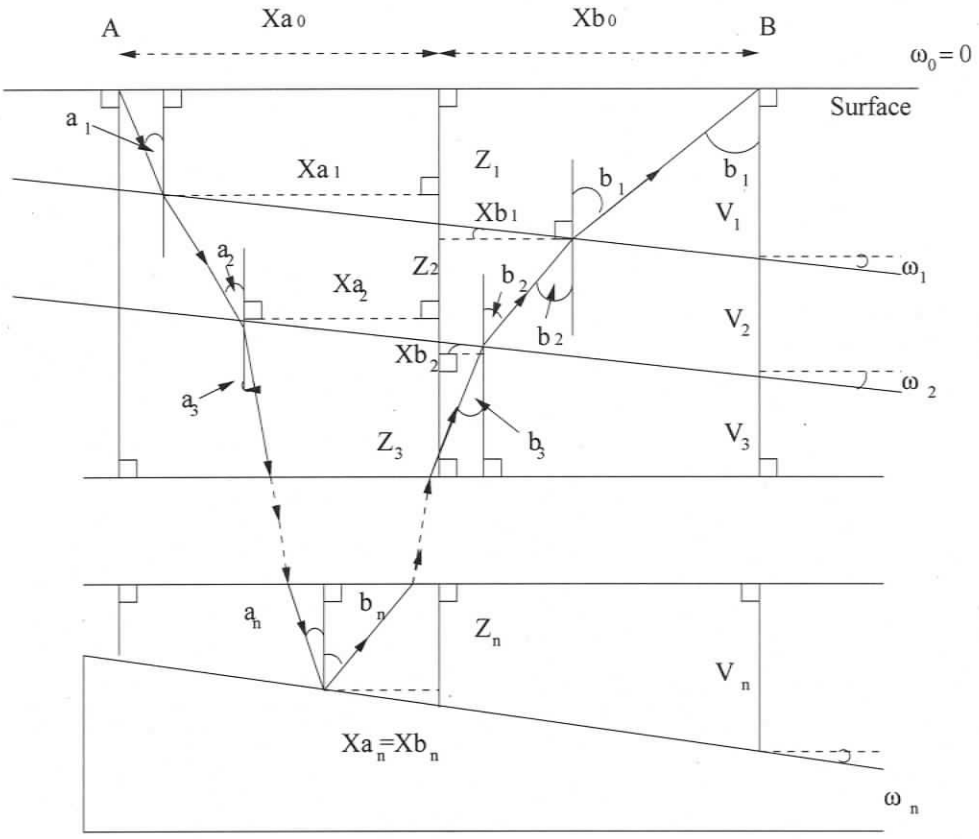

Figure B.2: *Model with n dipping interfaces specified by Z_j, V_j and ω_j. Z_j are the depths of interfaces measured at an arbitrary position between A and B. Xa_j and Xb_j are the distances from the point where the j^{th} down-going and up-coming rays, respectively, intercept the j^{th} interface to the arbitrary position. Then, each ray segment can be decomposed into its horizontal and vertical contributions in time. The total travel-time is the sum of travel-times of each ray segment.*

After expanding sums, using $Xa_n = -Xb_n = X_n$ and equation 3, 4, 5:

$$T = Pa_1 Xa_0 + Pb_1 Pb_0 + \sum_{j=1}^{n} Z_j (qa_j + qb_j) \tag{B.7}$$

If $Xa_0 = 0$ the vertical cable position Z_j will be at A. Then,:

$$T = Pb_1X + \sum_{j=1}^{n} Za_j(qa_j + qb_j) \tag{B.8}$$

where X is the offset between the cable position and the shots.

In order to compute $T(X)$, $X(p)$ is needed. Equation 8 is a straight line which is tangent to the travel-time curve at the point slope (T, X) with slope Pb_1 and intercept-time τ_A, it can be written:

$$T = Pb_1X + \tau_A \tag{B.9}$$

where τ_A is the total vertical time contribution of the ray all the way down and up the reflection path.

$$\tau_A = \sum_{j=1}^{n} Za_j(qa_j + qb_j) \tag{B.10}$$

or

$$\tau_A = \sum_{j=1}^{n} \frac{Za_j}{V_j} \left[\sqrt{(1 - Pa_j^2 V_j^2)} + \sqrt{(1 - Pb_j^2 V_j^2)} \right] \tag{B.11}$$

X can be derived by the derivate of τ_A with respect to Pb_1 on $T = Pb_1 X + \tau_A$, i.e.:

$$\frac{d\tau_A}{dPb_1} = -X \tag{B.12}$$

or with equation 11

$$X = \sum_{j=1}^{n} \left[Za_j Pa_j V_j (1 - Pa_j^2 V_j^2)^{-1/2} \frac{dPa_j}{dPb_1} + Za_j Pb_j V_j (1 - Pb_j^2 V_j^2)^{-1/2} \frac{dPb_j}{dPb_1} \right] \tag{B.13}$$

After differentiating and generalizing for n interfaces (previously solved for 2 interfaces case), $\frac{dPa_j}{dPb_1}$ and $\frac{dPb_j}{dPb_1}$ can be computed by:

$$\frac{dPa_j}{dPb_1} = \left[\prod_{i=j}^{n-1} \frac{dPa_i}{dPa_{i+1}} \right] \left[\frac{dPa_n}{dPb_n} \right] \left[\prod_{k=1}^{n-1} \frac{dPb_{k+1}}{dPb_k} \right] \tag{B.14}$$

for $j = 1$ $\frac{dPb_j}{dPb_1}$ is obtained from the previous differentiation of $\frac{dPa_n}{dPb_n}$ with respect to Pb_n:

$$\frac{dPb_j}{dPb_1} = \left[\prod_{i=1}^{j-1} \frac{dPb_{i+1}}{dPb_i}\right] \tag{B.15}$$

Equation 10 ($\tau_A = \sum_{j=1}^{n} Za_j(qa_j + qb_j)$) can be written for only one interface and using a_1 and b_1 angles:

$$\tau = \frac{Za_1}{V_1}(\cos a_1 + \cos b_1). \tag{B.16}$$

Then, a_1 and b_1 can be expressed by the reflection and dip angles of the interface:

$$a_1 = \Theta - \omega_1 \tag{B.17}$$

$$b_1 = \Theta + \omega_1 \tag{B.18}$$

Applying the cosine law:

$$\tau = \frac{2Za_1 \cos\omega_1}{V_1} \cos\Theta \qquad \rightarrow \qquad \tau = \tau_{max} \cos\Theta \tag{B.19}$$

(τ_{max} occurs where there is no horizontal contribution in time, only vertical ("normal ray").)

For the one layer case, τ is a direct function of the reflected slowness (τ has only time contribution from angles that generate the reflection. Observing the maximum value of τ in the curve, τ_{max}, and according to equation 18, $\Theta(Pb_1)$ can be determined.

Using two vertical angles b and b':

$$\Delta\Theta_1 = \Theta'_1 - \Theta_1$$

or using equation 18.

$$\Delta\Theta_1 = \sin^{-1}(Pb'_1V_1) - \sin^{-1}(Pb_1V_1) \tag{B.20}$$

$$\Delta\Theta_1 - \sin^{-1}(Pb'_1V_1) = -\sin^{-1}(Pb_1V_1)$$

$$V_1^2 = \frac{\sin^2(\Delta\Theta_1)}{(Pb_1 \cos\Delta\Theta_1 - Pb_1')^2 + Pb_1^2 \sin^2\Delta\Theta_1} \tag{B.21}$$

The dip can be computed:

$$\omega_1 = \sin^{-1}(V_1 Pb_1) - \Theta_1 \tag{B.22}$$

Pa_1 and Pb_1 are used as starting points to compute Pa_{n-1} and Pb_{n-1} through the Snell's law. Thus, τ_n is determined by removing the τ contribution of the overburden using equation 10. Next compute τ_n by equation 19. Three equation and three unknowns a_n, b_n and V_n:

$$\frac{\sin(a_{n-1} + \omega_{n-1})}{V_{n-1}} = \frac{\sin(a_n + \omega_{n-1})}{V_n} \tag{B.23}$$

$$\frac{\sin(b_{n-1} + \omega_{n-1})}{V_{n-1}} = \frac{\sin(b_n + \omega_{n-1})}{V_n} \tag{B.24}$$

$$\Theta_n = \frac{\sin^{-1}(Pa_n V_n) + \sin^{-1}(Pb_n V_n)}{2} \tag{B.25}$$

Interval velocity (solving these equations analytically for the interval velocity of the current layer):

$$V^2{}_n = \frac{\sin^2(2\theta_n)}{\{\frac{\sin(a_{n-1}+\omega_{n-1})}{V_{n-1}} + \frac{(\sin(b_{n-1}-\omega_{n-1})\cos 2\theta)}{V_{n-1}}\}^2 + \frac{\sin^2(2\theta_n)}{V^2{}_{n-1}}\sin^2(b_{n-1}+\omega_{n-1})}. \tag{B.26}$$

The dip can be computed by:

$$\omega_n = \sin^{-1}(V_n P b_n) - \theta_n. \tag{B.27}$$

The inversion requires measurements of the slowness at the cable and the emitted by the source to obtain a solution. This would be impossible in the conventional end on geometry since the vessel drags the receiver array. This method also requires $\tau - p$ transform, and for that not only a large aperture is required but also a small space between traces. Vertical cable technique provides all those requirements.

Appendix C

Downward continuation of sources and receivers

Mathematical description of the downward continuation of the shots by the phase shift plus interpolation (PSPI) method by Gazdag and Saguazzero [23]. For the continuation of the Dirac function of the receivers two option were used: numerical solution of the eikonal equation which provides travel-times everywhere in the velocity model and PSPI forward propagation. This methods are more accurate over complex geologic models since the complete solution of the wave-equation is obtained.

The plane wave equation for $P(x, y, z, t)$ can be expressed by the homogeneous differential wave equation:

$$\Delta^2 P = \frac{1}{c^2}\frac{\partial^2 P}{\partial t^2} \tag{C.1}$$

The above equation can be simplified by Fourier transforming one or more of the coordinates if its coefficients are constants along those coordinates. In the case of the above equation the coefficient is c. Thus, Fourier transform can be applied to the equation in any coordinate that c does not depend on.

The simplest case to treat is a velocity depending just on the depth z coordinate. Thus, the Fourier transform is applied to x, y and t to obtain:

$$\frac{\partial^2 P}{\partial z^2} + k^2 P - k_x^2 P - k_y^2 P = 0 \tag{C.2}$$

Provided that:

$$k^2 = k_x^2 + k_y^2 + k_z^2 \tag{C.3}$$

equation 2 becomes:

$$\frac{\partial^2 P}{\partial z^2} + k_x^2 P = 0 \tag{C.4}$$

The general solution for this kind of differential equation is expressed in term of exponential:

$$P = P_0 e^{\pm i k_z z} \tag{C.5}$$

provided that $\frac{dk_z}{dz} = 0$.

Let P_0 denote the value of the wave field at any depth z, then if the velocity is constant in the narrow strip $(z, z + \Delta z)$ the extrapolation wave field at $z + \Delta z$ is:

$$P = P_0 e^{\pm i k_z |\Delta z|} \tag{C.6}$$

The positive signal means back propagating. Fourier transforming the data in both the x- and y-direction gives k_z, whose solution depends on the dispersive equation expressed by:

$$k_z = \pm\sqrt{k^2 - k_x^2 - k_y^2} \tag{C.7}$$

or

$$k_z = \pm\frac{\omega}{c}\sqrt{1 - \frac{c^2}{\omega^2}k_x^2 - \frac{c^2}{\omega^2}k_y^2} \tag{C.8}$$

The Gazdag phase shift method [22] of wave-field extrapolation is achieved by applying phase shift in the Fourier transformed data:

$$P(k_x, k_y, z + \Delta z, \omega) = P(k_x, k_y, z, \omega) e^{iz\sqrt{1-\frac{c^2}{\omega^2}k_x^2-\frac{c^2}{\omega^2}k_y^2}} \tag{C.9}$$

The analytic solution expressed by the above equation which is the basis of the phase shift method, is not valid for the velocity field with lateral velocity variations. The PSPI extrapolation method, however,has been developed [23] to meet this objective. The procedure is centered around the idea that lateral velocity variation can be taken into account by interpolation among wave fields that were downward continued by phase-shift, using tow or more reference velocities. For two velocities $c_1(z)$ and $c_2(z)$:

$$P_1 = P_1^*(z) e^{i[k_z - \frac{\omega}{c_1}\Delta z]} \tag{C.10}$$

and

$$P_2 = P_2^*(z) e^{i[k_z - \frac{\omega}{c_1}\Delta z]} \tag{C.11}$$

The velocities are defined to be the extreme of $c(x, y, z)$:

$$c_1(z) = min[c(x, y, z)] \tag{C.12}$$

and

$$c_2(z) = min[c(x, y, z)] \tag{C.13}$$

Thus, the phase shift wave fields P_1 and P_2 are inverse Fourier transformed to $P_1(x, y, z + \Delta z, \omega)$ and $P_2(x, y, z + \Delta z, \omega)$. The final result is the interpolated wave field, in the frequency domain, of the modulus (A) and phase (θ) of both extrapolated wave fields:

$$A = \frac{A_1(c_2 - c) + A_2(c - c_1)}{c_2 - c_1} \tag{C.14}$$

and

$$\theta = \theta_1(c_2 - c) + \theta_2(c - c_1). \tag{C.15}$$

Appendix D

Abbreviations

ADCP : **A**coustic **D**oppler **C**urrent **P**rofiler

ASSA : **A**daptive **S**imulated **S**implex **A**nnealing

AT14 : **A**twater **V**alley **14**

AVA : **A**mplitude **V**ersus **A**ngle

AVO : **A**mplitude **V**ersus **O**ffset

BGHSZ : **B**ase of **G**as **H**ydrate **S**tability **Z**one

BSR : **B**ottom **S**imulating **R**eflector

CDP : **C**ommon **D**epth **P**oint

CMP : **C**ommon **M**id **P**oint

CMRET : **C**enter for **M**arine **R**esources and **E**nvironmental **T**echnology

CRG : **C**ommon **R**eceiver **G**ather

CTD : Conductivity-Temperature-Depth

DATS : Data Acquisition and Telemetry System

GHSZ : Gas Hydrate Stability Zone

GI Gun : Generated Injection Gun

GS : Gibbs Sampling

HRZ : High Reflectivity Zone

HSZ : Hydrate Stability Zone

LGC : Lookout Geophysical Company

MAP : Maximum A Posteriori

MC798 : Mississippi Canyon Block 798

MMTC : Marine Mineral Technology Center

NMO : Normal MoveOut

OBS : Ocean Bottom Seismometer

PPD : Posteriori Probability Distribution

PSPI : Phase Shift Plus Interpolation

RMS : Root Mean Square

SDI : Speciality Devices Inc.

SSDR : Surface Source Deep Receiver

TVG : Time Varying Gain

USGS : United States Geological Survey

VLA : **V**ertical **L**ine **A**rray

VSP : **V**ertical **S**eismic **P**rofiling

WEMVA : **W**ave **E**quation **M**igration **V**elocity **A**nalysis

References

[1] J. Anderson et al. 3-D vertical cable processing to obtain a pre-stack depth-migrated image. *SEG Technical Program Extended abstracts*, 16:1366, 1997.

[2] H. Arato, H. Akai, S. Uchiyama, T. Kudo, and K. Sekiguchi. Origin and significance of a bottom simulating reflector (BSR) in the Choshi Spur Depression of the offshore Chiba Sedimentary Basin, central Japan. *Journal of the Geological Society of Japan*, 102:972–982, 1996.

[3] A.J. Berkhout. *Seismic migration - imaging of acoustic energy by wave field extrapolation.* Elsevier, New York, 1980.

[4] B. Biondi and P. Sava. Wave-equation migration velocity analysis. *Extended Abstracts, 69th An. Internat. Soc. Expl. Geophysicists*, 1999.

[5] J.M. Brooks and M.C. Kennicutt. Thermogenic gas hydrates in the Gulf of Mexico. *Science Magazine*, 1984.

[6] N.R. Chapman. Modeling ocean-bottom reflection loss measurement with the plane-wave reflection coefficient. *J. Acoust. Soc. Amer.*, 73(5):1601–1607, 1983.

[7] J.F. Claerbout. *Imaging the earth's interior.* Blackwell scientific publications, New York, 1985.

[8] A.K. Cooper and P.E. Hart. Cruise report for a seismic investigation of gas hydrates in the Mississippi Canyon region in the northern Gulf of Mexico. *Cruise M1-98-GM*, 1998.

[9] A.K. Cooper and P.E. Hart. High-resolution seismic-reflection investigation in the northern Gulf of Mexico gas-hydrate-stability-zone. *Marine and petroleum geology*, 19:1275–1293, 2002.

[10] S.R. Dallimore and T.S. Collett. Regional gas hydrate occurences, permafrost condition, and Cenozoik geology, Mackenzie Delta area. *GSC Mallik 2L-38 Gas Hydrate Research Well, Mackenzie Delta, Northwest Territories, Canada, Geological Survey of Canada*, 1999.

[11] E.E. Davis, R.D. Hyndman, and H. Villinger. Rate of fluid expulsion across the northern Cascadia accretional prism: constrains from new neat flow and

multichannel seismic reflection data. *Journal of Geophysics Research*, 95:8869–8889, 1990.

[12] E. Demirbag et al. Inversion of P-wave AVO. *in J.P. Castagna and M.M. Backus, Eds., Offset-dependent-reflectivity -Theory and prcatice of AVO analysis, SEG*, pages 287–302, 1993.

[13] J.B. Diebold and P.L. Stoffa. The travel time equation tau-p mapping and inversion of common midpoint data. *Geophysics*, 46:238–254, 1981.

[14] W.P. Dillon and C.K. Paull. *Marine gas hydrate-II: Geophysical evidence*, volume Natural Gas Hydrates: Properties, Occurence and Recovery. Butterworth Publishers, 1983.

[15] C.H. Dix. Seismic velocties from surface measurments. *Geophysics*, 20:68–86, 1955.

[16] S.E. Dosso. Quantifying uncertainty in geoacoustic inversion I.: A fast Gibbs sampler approach. *The Journal of the Acoustical Society of America*, 111:142–159, 2002.

[17] S.E. Dosso. Quantifying uncertainty in geoacoustic inversion II.: Application to broadband, shallow-water data. *The Journal of the Acoustical Society of America*, 111:129–142, 2002.

[18] S.E. Dosso and G.R. Ebbeson. Array element localization accuracy and survey design. *CANADIAN ACOUSTICS*, 33(3), 2005.

[19] S.E. Dosso and C. W. Holland. Geoacoutic uncertainties from viscoelastic inversion of seabed reflection data. *IEEE Journal of Oceanic Engineering*, 31(3), 2006.

[20] M. Ewing, G.P. Wollard, and A. Vine. Geophysical investigation in the emerged and submerged atlantic coastal plain. *GSA Bulletin*, 50:257, 1939.

[21] A.F. Gangi and S.J. Yang. Traveltime curves for reflections in dipping layers. *Geophysics*, 41:245–255, 1976.

[22] L. Gazdag. Wave equation migration with phase-shift method. *Geophysics*, 44:1342–1351, 1978.

[23] L. Gazdag and P. Saguazzero. Migration of seismic data by phase shift plus interpolation. *Geophysics*, 49:124–131, 1984.

[24] E. Geresi. Geophysical identification of methane hydrates from the Mississippi Canyon area of the Gulf of Mexico. Master's thesis, University of Eötvös Loránd, 2002.

[25] E. Geresi. Monitoring seafloor instability caused by the presence of gas hydrate using ocean acoustical and geophysical techniques in the northern Gulf of Mex-

ico. *In press, AAPG Hedberg Conference Book "Gas Hydrates: Energy Resource Potential and Associated Geologic Hazards"*, 2007.

[26] E. Geresi and D. Hutchinson. Using multiple elimination to image geologic structures beneath the gas hydrate stability zone in the northern Gulf of Mexico. *Extended Abstracts, AAPG Annual Meeting*, 2003.

[27] E. Geresi et al. Seismic calibration of the proposed DOE/JIP drill site in Atwater Valley 14 in the Gulf of Mexico: Initial results in expected future development. *Extended abstracts, AAPG Annual meeting*, 2004.

[28] P. Gerstoft and C.F. Mecklenbrauker. Ocean acoustic inversion with estimation of a posteriori probablility distribution. *J. Acoust. Soc. Amer.*, 104(2), 1998.

[29] W.R. Gilks et al. *Markov chain Monte Carlo in practice.* Chapman and Hall, New York, 1996.

[30] G.D. Ginsburg et al. Gas hydrates in the southern Caspian Sea. *Izvestiya Akademii Nauk Seriya Geologisheskaya*, 7:5–20, 1992.

[31] M.A. Guimaraes. *Physical model study of seismic acquisition and processing of vertical cable dara.* PhD thesis, University of Texas, 1998.

[32] E.L. Hamilton. Geoacoustic modeling of the sea floor. *The Journal of the Acoustical Society of America*, 68:1313, 1980.

[33] B.A. Hardage. *Vertical Seismic Profiling Part A: Principles.* Geophysical Press, Houston, 1983.

[34] B.A. Hardage and H.H. Roberts. Gas hydrate in the Gulf of Mexico: What and where is the seismic target? *The Leading Edge*, May, 2006.

[35] D. Hutchinson and P. Hart. USGS Open-File Report 03-474, G1-03-GM, Gas Hydrates Cruise Report, R/V Gyre, 1-14 may 2003, northern Gulf of Mexico. *USGS Open-File Report 03-474*, 2003.

[36] P. Jaiswal. Seismic characterization of a gas hydrate system in the Gulf of Mexico - a novel approach for evaluating high-resolution wide-aperture data. Master's thesis, University of Houston, 2002.

[37] P. Jaiswal et al. Seismic characterization of a gas hydrate system in the Gulf of Mexico using wide-aperture data. *Geophys. J. Int.*, 165:108–120, 2006.

[38] S.H. Johnson. Interpretation of split-spread refraction data in terms of plane dipping layers. *Geophysics*, 41:418–424, 1976.

[39] M. Kastner et al. Chemistry, isotopic composition, and origin of a methane-hydrogen sulfide hydrate at the Cascadia subduction zone. *Earth and Planetary Science Letters*, 156:173–183, 1998.

[40] P.M. Krail. Case history: vertical cable 3-d acquisition. *In abstracts: 53rd EAEG*, 1991.

[41] P.M. Krail. Vertical cable as a subsalt imaging tool. *The Leading Edge*, 13:885, 1994.

[42] P.M. Krail. Vertical cable marine seismic acquisition. *In abstracts, Offshore Technology Conference*, 1997.

[43] K.A. Kvenvolden. Gas hydrates-geological prespective and global change. *Publication: Reviews of Geophysics*, 31:173–188, 1993.

[44] K.A. Kvenvolden and A. Grantz. Gas hydrates of the Arctic Ocean region. *in A. Grantz, L. Johnson, and J.F. Sweeney (eds.), The Arctic Ocean Region, Geol. Soc. Am., Boulder*, pages 939–942, 1990.

[45] K.A. Kvenvolden and T.D. Lorenson. The global occurence of natural gas hydrate. *Geophysical monograph 124, AGU*, 124:3–18, 2001.

[46] P. Leach. Strathspy vetical-cable seismic survey: a North Sea first. *SPE abstracts*, pages 333–347, 1997.

[47] A. Lowrie, C. Lutken, E. Geresi, and T.M. McGee. The lower Mississippi Canyon: Possible loci of multiple mass-wasting events. *AAPG Annual Meeting, In extended abstracts*, 2004.

[48] A. Lowrie et al. Unstable passive Continental Margins are currently unacceptable candidates for detailed risk analysis. *Energy Exploration*, 19:375–385, 2001.

[49] D.R. McConnell and B.A. Kendall. Images of the base of gas hydrate stability in the deepwater Gulf of Mexico. *The Leading Edge*, 4:361–367, 2003.

[50] T.M. McGee. High-resolution seismics in the frequency domain: An illustrated overview. *European Journal of Environmental and Engineering Geophysics*, 2:205–228, 1998.

[51] A.V. Milkov and R. Sassen. Estimate of gas hydrate resource, northwestern Gulf of Mexico Continental Slope. *Marine Geology*, 179, 2001.

[52] L. Mota. Determination of dips and depths of geological layers by the seismic source analysis. *Geophysics*, 19(2):1542–1548, 1954.

[53] T.W. Neurauter and W.R. Bryant. Gas hydrates and their association with mud diapir/mud volcanoes on the Louisiana Continental Slope. *Proceedings of the 21st Offshore Technology Conference Paper*, 1(5944):599–607, 1989.

[54] L. Ocola. A non-linear least-squares method for seismic refraction mapping - part i: algorithm and procedure. *Geophysics*, 37:260–272, 1972.

[55] W.I. Ostrander. Plane-wave reflection coefficients for gas sands at nonnormal angles of incidence. *Geophysics*, 49:1637–1648, 1984.

[56] C.R. Partouche and T.M. McGee. Source signature processing in deep water, Gulf of Mexico: comparison between deterministic deconvolution and phase conjugation. *earth-prints.org*, 2000.

[57] C. Paull, W. Ussler, W. Winters, and Lorenson T. Constraints on the distribution of gas hydrates in the Gulf of Mexico. *Geophysical Research Abstracts, European Geophysical Society*, 6:12019, 2003.

[58] M. Riedel, S.E. Dosso, and L. Beran. Uncertainty estimation for amplitude variation with offset (AVO) inversion. *Geophysics*, 68(5):1485–1496, 2003.

[59] M. Riedel, G.D. Spence, N.R. Chapman, and R.D. Hyndman. Deep sea gas hydrates on the northern cascadia margin. *The Leading Edge*, 20(1):87–91, 2001.

[60] M. Riedel et al. Seismic investigations of a vent field associated with gas hydrates, offshore Vancouver Island. *Journal of Geophysical Research*, 107, 2002.

[61] H.H. Roberts et al. Fluid and gas expulsion on the northern Gulf of Mexico Continental Slope : Mud-prone to mieral-prone responses. *In Abstracts, AGU*, 81, 2001.

[62] R. Sassen and I.R. MacDonald. Evidence of structure h hydrate, Gulf of Mexico Continental Slope. *Organic Geochemistry*, 22, 1994.

[63] R. Sassen, S.V. Sweet, A. Milkov, A.V. DeFreitas, M.C. Kennicut II, and H.H. Roberts. *Stability of thermogenic gas hydrate in the Gulf of Mexico: Constrains of models of climate change, in natural gas hydrates occurrences*, volume Distribution and Detection: Geophysical Monograph 124. Marcel Dekker, New York, 2001.

[64] P. Sava and W.W. Symes. A generalization of wave-equation migration velocity analysis. *Stanford Exploration Project, Rep. Nr. 112, Stanford University*, 2002.

[65] K.K. Sekharan. 3-D marine data acquisition and processing over ACTI/EAGE physical model using vertical hydrophone array. *In abstracts, Offshore Technology Conference*, 1997.

[66] M.K. Sen and P.L. Stoffa. Rapid sampling of model space using generic algorithms: examples from seismic waveform inversion. *Geophysical Journal International*, pages 287–302, 1992.

[67] M.K. Sen and P.L. Stoffa. *Bayesian inference, Gibbs' sampler and uncertainty estimation in geophysical inversion.* Geophysical Prospect., Blackwell Synergy, New York, 1996.

[68] C.E. Shannon. The mathematical theory of communication. *Bell System Technical Journal (July and October)*, 1948.

[69] T.H. Shipley and M.H. Houston. Seismic evidence for wildespread possible gas hydrate horizons on the Continental Slope and Rises. *AAPG Bulletin*, 1979.

[70] E.D. Sloan. *Clathrate hydrates of natural gas.* Marcel Dekker, New York, 1990.

[71] A. Tarantola. *Inverse problem theory: Methods for data fitting and model parameter estimation.* Elsevier, Amsterdam, 1987.

[72] A.M. Trehu et al. Temporal and spatial evolution of a gas hydrate-bearing accetionary ridge on the Oregon Continental Margin. *Geology*, 27:939–942, 1999.

[73] W.T. Wood and J.F. Gettrust. Deep-tow seismic investigations of methane hydrates. *Geophysical monograph (Geophys. monogr.) ISSN 0065-8448, Natural Gas Hydrates: Occurrence, Distribution, and Detection*, 124:165–178, 2001.

[74] W.T. Wood, S.W. Holbrook, and H. Hoskins. In situ meausrents of P-wave attenuation in the methane hydrate- and gas-bearing sediments of the Blake Ridge. *Proceedings of the Ocean Drilling Program, Scientific Results*, 164, 1994.

[75] A.G. Yefremova and B.P. Gritchina. Gas hydrates in sediments beneath seas and the problem of their exploitation. *Geologiya Nefti i Gaza*, 2:32–35, 1981.

[76] O. Yilmaz. *Seismic Data Processing.* SEG Publication, 1987.

[77] K. Zoeppritz. On the reflection and propagation of seismic waves. *Gottinger Nachrichten*, Erdbebenwellen VIIIB(I):66–84, 1919.